

POLYMERIC MICRORING RESONATOR BASED
ELECTRO-OPTIC MODULATOR

POLYMERIC MICRORING RESONATOR BASED ELECTRO-OPTIC MODULATOR

PROEFSCHRIFT

ter verkrijging van
de graad van doctor aan de Universiteit Twente,
op gezag van de rector magnificus,
prof. dr. W.H.M. Zijm,
volgens besluit van het College voor Promoties
in het openbaar te verdedigen
op vrijdag 27 mei 2005 om 15.00 uur

door

Arne Leinse

geboren op 22 januari 1977
te Enschede, Nederland

Dit proefschrift is goedgekeurd door:

De promotor: Prof. Dr. A. Driessen

De assistent-promotor: Dr. ing. M.B.J. Diemeer

Contents

1	INTRODUCTION	1
1.1	THz	1
1.2	NAIS	2
1.3	DEVICE PRINCIPLE	3
1.4	BOUNDARY CONDITIONS.....	5
2	THEORY.....	7
2.1	INTRODUCTION	7
2.2	POLYMERS AND THEIR PROPERTIES	8
2.2.1	<i>Absorption properties</i>	8
2.2.2	<i>Thermal properties</i>	9
2.2.3	<i>Nonlinear polymer configurations</i>	10
2.2.4	<i>Electro-optic properties</i>	11
2.2.5	<i>Poling and poling-induced loss</i>	15
2.2.6	<i>Electric fields in layerstacks</i>	19
2.2.7	<i>Comparison to organic materials</i>	22
2.3	RINGRESONATOR.....	23
2.3.1	<i>Operation description</i>	23
2.3.2	<i>Thermal/electrical dependence</i>	27
2.3.3	<i>Bandwidth limitations</i>	29
2.4	MACH-ZEHNDER INTERFEROMETER	31
2.4.1	<i>Operation description</i>	31
2.4.2	<i>Thermal/electrical dependence</i>	33
3	DEVICE DESIGN	37
3.1	CHOICE OF MATERIALS	38
3.1.1	<i>Material parameters</i>	40
3.2	STRUCTURE DESIGN	47
3.2.1	<i>Waveguide design</i>	47
3.2.2	<i>Ringresonator design</i>	50
3.2.3	<i>Total device</i>	56
3.2.4	<i>Electrode design</i>	60
3.3	MASK DESIGN	62
4	REALIZATION.....	67
4.1	FABRICATION STEPS.....	67
4.2	FABRICATION ISSUES	70
4.2.1	<i>Buffer layer spincoating</i>	70
4.2.2	<i>SU8 lithography</i>	71
4.2.3	<i>Intermediate layer</i>	73
4.2.4	<i>Surface modifications</i>	75
4.2.5	<i>PMMA-DR1 etching</i>	76
4.2.6	<i>PMMA-DR1 reflowing</i>	76
4.2.7	<i>Topcladding spincoating</i>	77
4.2.8	<i>Electrode deposition</i>	78
4.2.9	<i>Interruptions in the fabrication process</i>	79
4.2.10	<i>Dicing</i>	79
4.2.11	<i>Poling</i>	80
4.2.12	<i>Packaging</i>	81
5	CHARACTERIZATION	83
5.1	MATERIAL PROPERTIES MEASUREMENTS	83
5.1.1	<i>Ellipsometry</i>	83
5.1.2	<i>Resistivity measurements</i>	85

5.1.3	<i>Surface scattering measurements</i>	87
5.1.4	<i>Prism coupler loss measurements</i>	89
5.2	DEVICE-MEASUREMENTS	90
5.2.1	<i>Passive MR-behaviour</i>	91
5.2.2	<i>Thermal tuning</i>	100
5.2.3	<i>Electro-optic modulation in MR</i>	101
5.2.4	<i>Electro-optic modulation in MR with MZI</i>	105
5.3	PHOTO-STABILITY MEASUREMENTS	108
6	CONCLUSIONS	113
7	SUMMARY	115
	APPENDIX	117
	REFERENCES	141
	SAMENVATTING (DUTCH)	149
	DANKWOORD (DUTCH)	151
	BIBLIOGRAPHY	153

1 Introduction

This chapter will discuss the framework in which the work was done for this thesis where integrated optical devices were designed, realized and characterized. A short description of the two projects involved in this is given, after which the devices with different boundary conditions are discussed.

1.1 THz

In the Strategic Research Orientation Terahertz (THz) of the MESA⁺ institute of the University of Twente, the design and realization of key components for a superconducting Analog Digital Converter (ADC) system, suitable for software-defined radio, are carried out. The objective is to arrive at an ADC with 16 bits resolution, a clock frequency of 15 GHz and an input bandwidth of 60 MHz. The ADC will be built in high-T_c technology, based on superconducting YBaCuO related materials, consisting of circuits containing around 50 Josephson elements. This part is strongly supported by the EC-program "Super ADC". A parallel study based on low-T_c materials is the fault modelling in complicated processes and circuits. The readout of the superconducting chip is performed by an Electro-Optical (EO) modulator that is connected to an optical CMOS device, which is positioned at a different temperature than the superconducting circuits. These superconducting circuits should operate at about 30 K, and cooling is therefore another topic in this project. Actually, the THz-program is a cooperation between five groups in the Applied Physics and Electrical Engineering departments. A part of the system considered in THz is given schematically in figure 1.1.

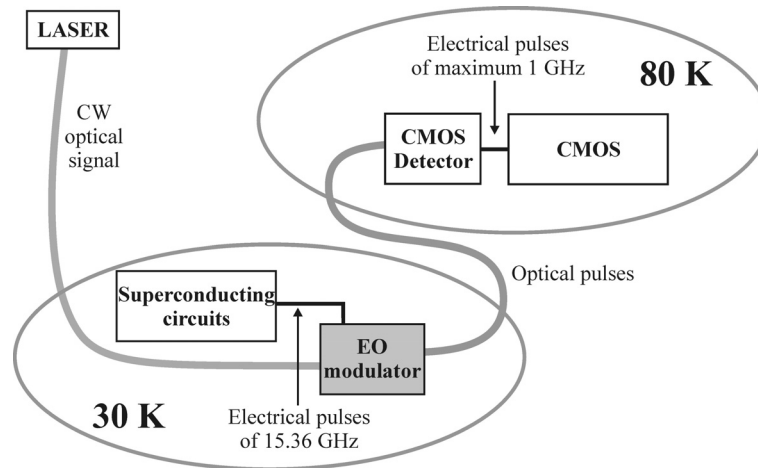


Figure 1.1: Schematic representation of the connection between superconducting circuits and CMOS by an EO modulator.

Figure 1.1 also shows the frequency problem of this setup. The modulation frequency of the superconducting circuits is 15.36 GHz, while the operating frequency of the CMOS (and the CMOS detector) is around 1GHz. The splitting of the 15.36 GHz signal can be done before or after the modulator. Both options set different demands for the modulator

1.2 NAIS

Another project which plays an important role in the work done for this thesis is the EC-IST project (number 2000-28018) Next-generation Active Integrated optic Subsystems (NAIS). The drive for this project is the increasing demand set on communication networks. Especially the metropolitan networks and even the access networks become optical because of the rapidly increasing bandwidth need of the users. In this context integrated optical devices have to compete with the bulk optic solution with respect to performance and price. Bulk optics is mainly used in the long-haul telecommunications and adapting optical solutions from this long-haul network for operation in the access networks is not the way to go because these devices have been optimized for performance and not for low cost.

In order to make an integrated optical device for these access networks an elementary building block can be used. This building block is the optical ring resonator that can be used to realize a large number of optical and electro-optical (EO) functions.

In the original project-description an innovative subsystem, a Wavelength Division Multiplexer (WDM) transceiver for the access node is proposed. This device is schematically shown in figure 1.2.

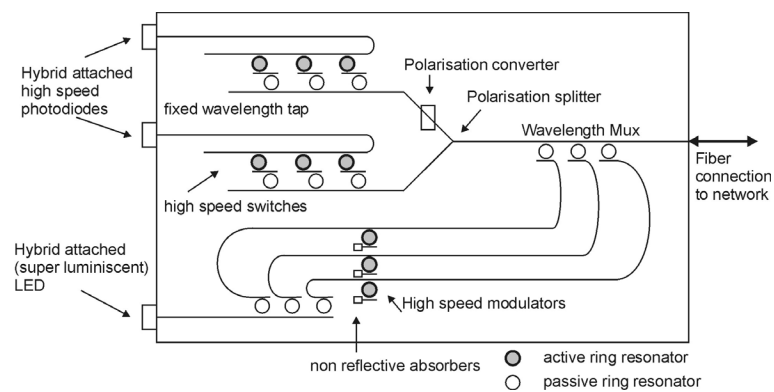


Figure 1.2: WDM transceiver for an access network with a large number of wavelengths used for downstream and upstream communication.

Ring resonators are used for passive wavelength slicing, high-speed modulation and passive multiplexing at the transmitter side and high-speed single wavelength tapping at the receiver side.

1.3 Device principle

This thesis will deal with the high speed EO modulators for this WDM transceiver and the THz project. The building block for this modulator, the Microring Resonator (MR), was demonstrated before by several groups, see e.g. [Rabiei.2002] [Little.1998] [Klunder.2000] and will be discussed in more detail in chapter 2. Two basic devices with a MR will be shown here and discussed in the rest of the thesis. These structures are a single MR and a MR combined with a Mach-Zehnder Interferometer (MZI). The single MR consists of a cylindrical waveguide coupled to two straight port-waveguides, by either placing the waveguides horizontally next to the MR or vertically below (or above) the MR. Both options have their benefits and drawbacks, as discussed by [Klunder.2002].

The two devices with different coupling options are schematically shown in figure 1.3.

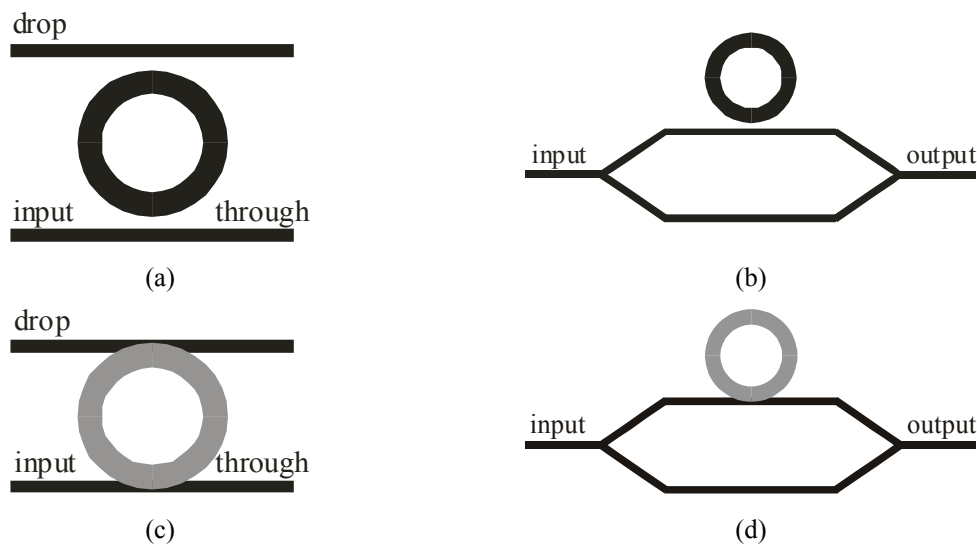


Figure 1.3: Schematic representation of the MR and MR with MZI devices. (a) MR and waveguides coupled horizontally in the same waveguide layer (b) MR and MZI coupled horizontally in the same waveguide layer (c) MR and waveguides coupled vertically and realized in different waveguide layers (d) MR and MZI coupled vertically and realized in different waveguide layers

In this thesis, vertically coupled MR structures (figure 1.3 (c) and (d)) will be chosen because the properties of the MR and port-waveguide can be easily varied independently of each other. Controlling the distance (coupling) between MR and port-waveguides is in this geometry straightforward by controlling the layer-thickness of the layer between them. The most critical fabrication difference between horizontal or vertical coupling is the alignment between MR and port-waveguides. The vertical coupling is a 2 mask fabrication process, introducing a critical alignment step of the MR to the port-waveguides. This fabrication step is less critical when the MR is placed on one of the branches of an MZI, because the MR is only coupled to one waveguide and the spectral behaviour of an MR is less sensitive to this single waveguide coupling than double waveguide coupling.

The MR has to function as an EO modulator and therefore it is fabricated from a material of which the optical properties change under the influence of an electric field. This material is an EO polymer, PolyMethyl-MethAcrylate Disperse Red1 (PMMA-DR1), synthesized by the Ecole Nationale Supérieure de Chimie de Montpellier and consisting of a Disperse Red1 (DR1) chromophore (the chemical group that gives colour and nonlinear properties to the polymer) connected to a Methyl-MethAcrylate (MMA) group, that forms the backbone of the polymer. Because the electric field is easily applied by sandwiching the MR (and the layers around it) between two electrodes, polymers are very suitable for the complete device fabrication because of their easy applicability on metal layers.

Both devices from figure 1.3 (c and d) will be discussed in this thesis and because the MR is the main, and most critical, building block in both, the design and characterization will be mainly focused on this structure. In the characterization chapter, measurements of both the MR and MR-MZI are presented.

1.4 Boundary conditions

Both projects for which the modulator was realized set different demands for it. The following list summarized the device demands set by the two different projects.

	THz	NAIS
Operating wavelength	< 850 nm	1530-1560 nm
Modulation frequency	1 GHz (set by the CMOS side) 15 GHz (set by the superconducting circuits)	1.25 Gbit/s
Operating temperature	< 10 K	Ambient temperature
Available modulation voltage	>1 mV _{pp} < 100 mV _{pp}	~ 1 V _{pp} . Lower is preferable. Demonstrating high frequency modulation is main aim of the project.
Needed optical modulation depth	As close to 100 % as possible	As close to 100 % as possible
Device dimensions	No restrictions	Small area
Device principle	No restrictions	MR

Table 1.1: Demands set to the modulator by the two different projects.

From table 1.1 it can be seen that the demands are more critical for the THz project than for the NAIS project. The most logical step is therefore to first realize a proof of principle device for the NAIS project, which can be redesigned afterwards for the THz project. Another great advantage in the NAIS project is the use of the standard telecom wavelengths (the telecom window around 1550 nm is used), for which characterization equipment is available. A wavelength of 1550 nm is chosen in all the simulations and characterizations in this thesis.

The lower available modulation voltage in the THz project means that the NAIS device must be optimized to function at much lower voltages than usual.

The lower operating temperature used in the THz project should not be a problem because the materials of which the devices will be fabricated are polymers and some tests done by AKZO Nobel [Diemeer.1998] show that they can sustain very large temperature differences.

The following chapters will discuss the design, realization and characterization of the EO MR and EO MR-MZI devices. The build-up of the thesis is as follows:

- The current chapter gives an introduction to both projects for which the work of this thesis is done and a short description of the device principle.
- In the second chapter the theory related to material and device properties will be discussed
- The design of the device will be discussed in chapter 3
- The different fabrication steps with the solution of problems that arose will be treated in chapter 4
- Chapter 5 shows the characterization of the realized devices
- After which in chapter 6 and 7, conclusions will be drawn and a summary will be given.
- Finally an appendix presents some useful details

2 THEORY

2.1 Introduction

This chapter deals with the different elements of theory used in designing, realizing and characterizing the polymeric electro-optical (EO) modulators.

As was described in the introduction chapter, two different device lay-outs are considered. Both approaches make use of Microring Resonators (MR). The first device is an MR with a through and a drop waveguide (schematically shown in figure 2.1.a). The second device is a Mach-Zehnder Interferometer (MZI) with an MR on one of the branches (see figure 2.1.b)

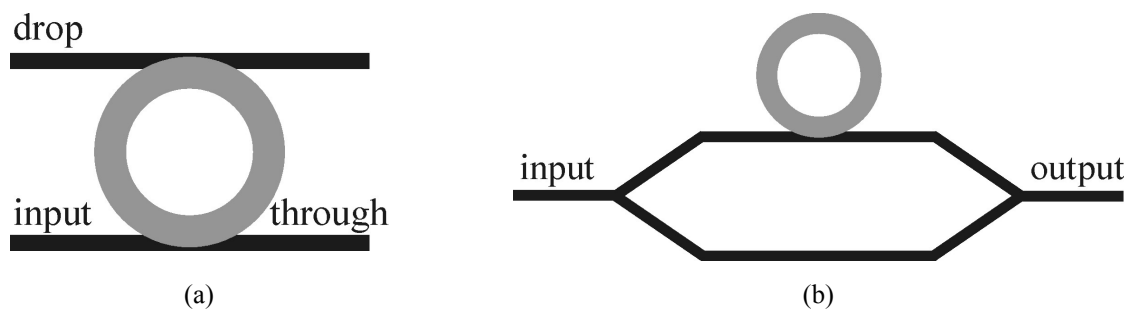


Figure 2.1: Schematic representation of two modulator devices. a) Single MR b) Mach-Zehnder Interferometer with MR

The two devices have one common element (which is also the most critical one in the design), namely the MR. The main part of this thesis will therefore deal with the structure shown in figure 2.1.a. The second device (MR-MZI) is nothing more than two additional splitters/combiners in the waveguides.

For all the different axis notations in this chapter a right handed coordinate system is used in which the axis are as given in figure 2.2.

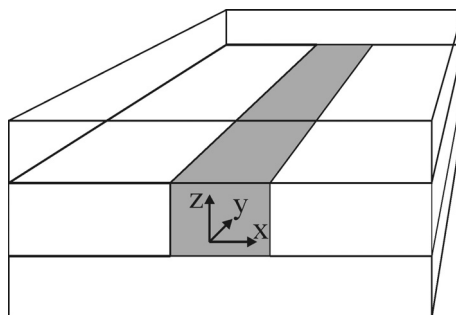


Figure 2.2: Definition of axis-system in an optical waveguide

2.2 Polymers and their properties

2.2.1 Absorption properties

A very important issue of organic polymers used in integrated optics is the optical loss occurring in the waveguide, which can be caused by both scattering and absorption and a material with very high absorption is not suitable for integrated optical applications. Losses caused by scattering, due to waveguide roughness, can very often be reduced by optimizing the fabrication process. Measuring the absorption loss is very important when selecting materials for optical devices. The materials used in active optical devices should have nonlinear optical (NLO) coefficients that are as large as possible. Large coefficients however means that the absorption bands of the NLO chromophores must be located near the desired operating wavelength [Skumanich.1993], but should have no overlap with this wavelength (no absorption should occur at this wavelength). The nonlinear materials are therefore the most difficult/critical to choose in the device design.

The absorption over a large wavelength range was measured for the polymer PolyMethylMethAcrylate (PMMA) with different NLO chromophores added to it [Skumanich.1993]. The polymer used in the NAIS project has a Disperse Red (DR1) side-chain. The measured spectra are given in figure 2.3.

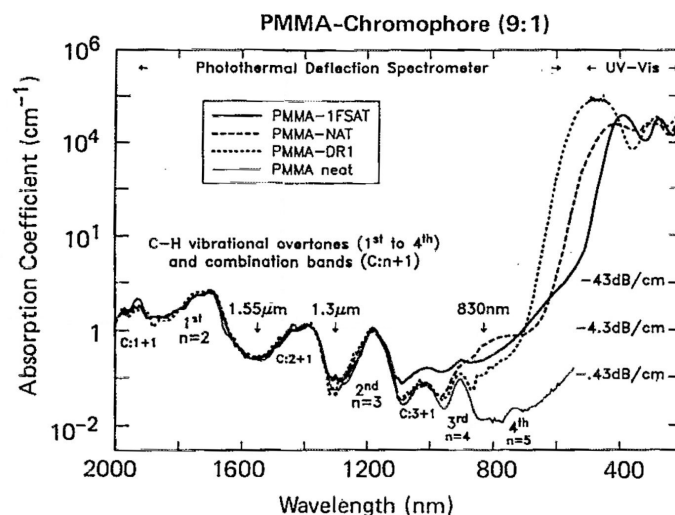


Figure 2.3: Measured absorption for PMMA with different chromophores [Skumanich.1993]

What can be seen from figure 2.3 are the C-H overtones present at wavelengths above 1 μm . Two windows that coincide with the telecom windows at 1320 and 1550 nm can clearly be seen. For PMMA-DR1 it can even be seen that at a wavelength between 800-850 nm the

absorption is relatively low compared to the other chromophores, making the material also useable at this wavelength range, which is needed if the modulator must be used in combination with the CMOS detector developed in the THz project.

What also can be seen from figure 2.3 is the absorbance of the material at the lower wavelengths, which is caused by the primary electronic transitions of the chromophore [Skumanich.1993]. These transitions have a long absorption tail in the region from 500 nm to 1 μm . Each chromophore has a wavelength of maximum absorption (λ_{max}). For the Disperse Red chromophore this λ_{max} is around 500 nm [Serat.2001] [Alkeskjold.2004] (as can be seen from figure 2.3)

2.2.2 Thermal properties

When using polymers in optical devices the change in refractive index as a function of temperature changes must be taken into account. This change is due to the change in the density of the material and the thermo optic (TO) coefficient can be written as [Diemeer.2003]:

$$\frac{dn}{dT} = -\left(\frac{\rho \partial n}{\partial \rho}\right)_T \gamma + \left(\frac{\partial n}{\partial T}\right)_\rho \quad (2-1)$$

in which ρ is the density and γ is the volume expansion coefficient. At room temperature the term $(\rho \partial n / \partial \rho)_T \sim 0.5$ for most polymers, while γ is for most polymers in the order of $2 \times 10^{-4} / ^\circ\text{C}$ [Diemeer.2003]. The second term $(\partial n / \partial T)_\rho$ is much smaller and is for polycarbonate and PMMA for instance $\sim 9 \times 10^{-6} / ^\circ\text{C}$ and $\sim -4 \times 10^{-6} / ^\circ\text{C}$ respectively [Waxler.1979].

Polymers are very often used in devices as thin films with a silicon wafer as a carrier. Silicon has a much lower thermal expansion $\gamma = 8.1 \times 10^{-6} / ^\circ\text{C}$ [Diemeer.2003] and is also a much stiffer material (the ratio between the Young's moduli $E_{\text{Si}} / E_{\text{polymer}} \sim 10^2$). This has a consequence that the polymer layers are constrained in their expansion or contraction. The volume expansion coefficient is effectively reduced by this effect. For a polymer film on a rigid substrate the following relation for the corrected γ can be derived.

$$\gamma^* = \frac{1}{3} \left(\frac{1+\nu}{1-\nu} \right) \gamma \quad (2-2)$$

where ν is the Poisson's ratio. For polymers this factor is relatively high ~ 0.4 , which results in only a small change in γ of a factor of $\gamma^*/\gamma=0.8$.

2.2.3 Nonlinear polymer configurations

The nonlinearity in polymeric systems is caused by a nonlinear chromophore which consists of a donor-acceptor distributed π -conjugated electron system. This system has basically three building blocks, namely an electron donor on one side, a π -bridge in the middle and an electron acceptor on the other side [Gunter.2000]. Schematically the molecule is shown in figure 2.4.

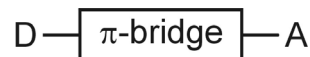


Figure 2.4: Donor-acceptor distributed π -conjugated system

The donor, acceptor and π -bridge can be substituted by various chemical structures, of which [Gunter.2000] gives a short overview of some of the possibilities.

The NLO chromophore by itself has nonlinear properties, but the cooperative effect of a lot of these chromophores in a device layer can result in a zero net nonlinear effect. In a random orientated chromophore layer all the individual nonlinearities cancel out and some polar order must be created, which can be done by a process called poling (further explained in chapter 2.2.5). Once the chromophores are aligned by poling this alignment should be retained and therefore the chromophores must be packed in another material. Polymers are well suited for this task, because the chromophores can easily be packed in their molecular structure and fabrication of thin layers of polymers is relatively easy. Roughly four different types of packaging can be distinguished. These four types are:

- Guest-host
 - o The chromophores are simply mixed in a polymer matrix, making it very easy to fabricate but long term stability of the polar order is not guaranteed due to relaxation effects.

- Side-chain
 - This is one of the most applied types and has as an advantage that the chromophore's covalent bonding to the polymer backbone makes the long term stability better as compared to the guest host system
- Cross-linked
 - In this type the chromophore is covalently bonded to more than one backbone, making it more stable but also more difficult to align.
- Main-chain
 - In this type the chromophore becomes a part of the polymer-backbone, making it very stable but also very difficult to process.

In figure 2.5 [Gunter.2000] the four types are schematically given.

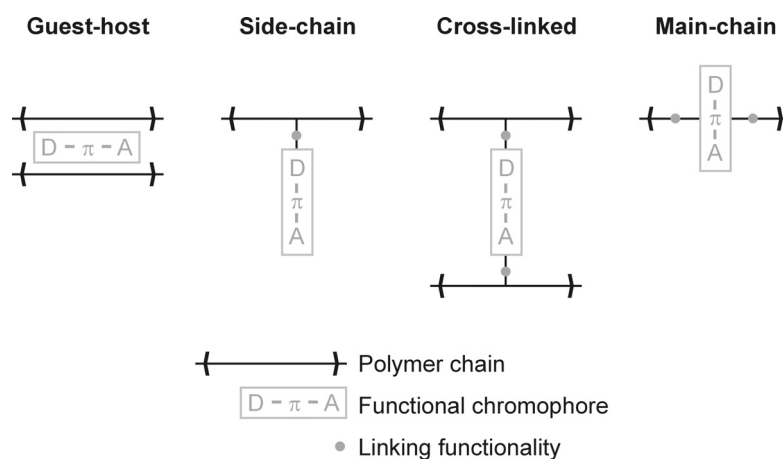


Figure 2.5: Schematic view of the different types of polymers

The PMMA-DR1 polymer used in the NAIS project is of the side chain type.

2.2.4 Electro-optic properties

To discuss the EO effect in the material used in the MR, this effect can first be considered on a microscopic level. The NLO chromophore that is used, must be a non-centrosymmetric molecule [Yariv.1975] [Gunter.2000] [Singer.1987] and this molecule must have non-linear polarizability (p), which can be described in terms of the ground state dipole moment (μ_g), the linear polarizability α_{ij} and the first order hyper-polarizability (β_{ijk}) (in which i, j, k are indices of a tensor in the Einstein convention). When using the Einstein convention this is given by:

THEORY

$$p_i = \mu_{g,i} + \varepsilon_0 \alpha_{ij} E_j^0 + \varepsilon_0 \beta_{ijk} E_j^0 E_k^0 + \dots \quad (2-3)$$

In which E_j^0 and E_k^0 are the local electrical fields acting on the molecule as a result of applied electric fields. For the relation between the formulas for the single molecule and the macroscopic effects, different theories can be found in literature. The difference between these theories depends on the degree of interaction between neighbouring molecules that is taken into account. A clearly described model is given by [Firestone.1995] and [Singer.1987] in which an important parameter is the angle between the ground state dipole moment (μ_g) and the applied electric field. In figure 2.6 this angle is given in polar coordinates.

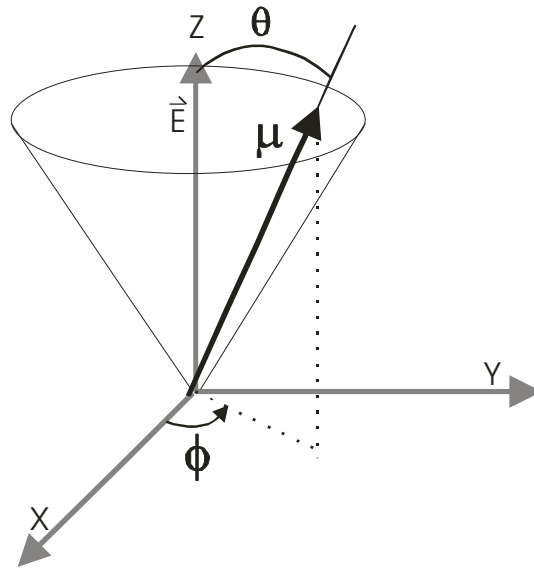


Figure 2.6: Three dimensions model of a polar molecule in the presence of an external field [Firestone.1995]. θ is the spherical polar angle between the principle molecular dipole axis, μ , and the field E . ϕ is the azimuthal angle

If for instance the β_{zzz} component dominates [Firestone.1995] and [Bauer.1996] state that the macroscopic susceptibility for the second order nonlinearity can be written as.

$$\chi_{zzz}^{(2)} = N \beta_{zzz} \langle \cos^3 \theta \rangle / 2 \quad (2-4)$$

In which N is the chromophore number density, β_{zzz} is a component of the molecular hyperpolarizability and $\langle \cos^3 \theta \rangle$ the angular average which describes the polar order of the molecules.

The macroscopic relation for the polarization as a function of the applied electric field (\vec{E}) is given by.

$$P_i = P_{0,i} + \varepsilon_0 \chi_{ij}^{(1)} E_j + \varepsilon_0 \chi_{ijk}^{(2)} E_j E_k + \varepsilon_0 \chi_{ijkl}^{(3)} E_j E_k E_l + \dots \quad (2-5)$$

P_0 is the spontaneous polarization, $\chi^{(n)}$ the n^{th} order susceptibility tensor and ε_0 the permittivity of the vacuum.

The susceptibility tensor has a symmetry property ($\chi_{ijk} = \chi_{jik}$) and has therefore 18 independent elements. Dependent on the structure of the material, the 18 elements can further be reduced by symmetry considerations [Sauter.1996]. In a uni-axial medium the only macroscopic anisotropy is the optical axis (the z-axis in this description). Directions perpendicular to this axis are equivalent and can be arbitrarily chosen. This causes the susceptibility tensor to be nonzero for only five components of which there are three independent.

1. χ_{zzz}
2. $\chi_{xxz} = \chi_{yyz}$
3. $\chi_{xzx} = \chi_{yzy}$

of which the first two (1 and 2) represent a change in refractive index caused by an electric field and the third component (3) represents a polarization rotation caused by an electric field. The linear EO effect, also known as the Pockels effect, is frequently described by an EO tensor r_{ijk} instead of the susceptibility tensor. The relation between the two is given by:

$$\chi_{ijk} = -\varepsilon_{ii} \varepsilon_{jj} r_{ijk} \quad (2-6)$$

in which ε_{ii} and ε_{jj} are the permittivities of the material.

Because χ_{ijk} is symmetric in the first two indices (ij) r_{ijk} is also symmetrical in these indices and also for r_{ijk} an 18 element matrix can be defined with the definition ($i,j,k=1,2,3$).

$$\begin{aligned} r_{11k} &= r_{1k}, & r_{22k} &= r_{2k}, & r_{33k} &= r_{3k}, \\ r_{23k} &= r_{32k} = r_{4k}, & r_{13k} &= r_{31k} = r_{5k}, & r_{12k} &= r_{21k} = r_{6k} \end{aligned}$$

THEORY

This matrix is often called the “EO tensor” and the change in refractive index due to an electric field can be written as [Gunter.2000]

$$\Delta\left(\frac{1}{n_i^2}\right) = \sum_i r_{ik} E_k \quad (2-7)$$

where $i = 1\dots 6$; $k = 1\dots 3$. No universal EO behaviour can be predicted applicable to all materials. The r -tensor is generally very sparse and has only a few nonzero elements, determined by unique crystal symmetries. Günter [Gunter.2000] predicts a ratio $r_{33}/r_{13} = 3$, based on an oriented gas model, for a poled polymer. Rotational symmetry leads to the equality $r_{13} = r_{23}$. Furthermore $r_{42} = r_{51}$ is also nonzero. This value doesn't contribute to a change in refractive index but represents a polarization rotation.

The tensor for poled polymers is given by [Gunter.2000].

$$r_{ik} = \begin{bmatrix} 0 & 0 & r_{13} \\ 0 & 0 & r_{13} \\ 0 & 0 & r_{33} \\ 0 & r_{51} & 0 \\ r_{51} & 0 & 0 \\ 0 & 0 & 0 \end{bmatrix} \quad (2-8)$$

When applying an electric field in the z -direction (E_3), r_{51} does not contribute to a refractive index change. The change can be separated in two directions.

For the two different indices this is given by,

$$\begin{aligned} \Delta n_1 &= -\frac{1}{2} r_{13} E_3 n_1^3 \\ \Delta n_3 &= -\frac{1}{2} r_{33} E_3 n_3^3 \end{aligned} \quad (2-9)$$

When poling with electrodes above and below the MR, the electrical field will be in the z direction (E_3) meaning that the largest change in refractive index is in this direction (Δn_3).

Because the optical field of the TM mode is largely in the z-direction, this mode will sense the largest effect of an applied electric field. The ratio between the nonlinear effects for TM and TE polarization is equal to the ratio between r_{33} and r_{13} and is 3.

2.2.5 Poling and poling-induced loss

Poling of the MR is necessary to orientate the molecular dipoles in an electric field, breaking the centro-symmetry in the polymer layer. The orientation of the molecular dipoles is only possible because polymeric materials have a glass transition temperature (T_g). To explain the definition of a T_g , the polymers are compared to crystalline materials, which normally have a very sharp solid-liquid transition when heated. Schematically the heating of different materials is shown in figure 2.7 [Vegt.1994]. In this figure the heating of a crystalline material can be seen, where the slope of the line FC is the expansion coefficient of the crystalline phase and at the melting-point (T_m) the volume expands from C to B after which the slope of BA is the larger expansion coefficient of the liquid.

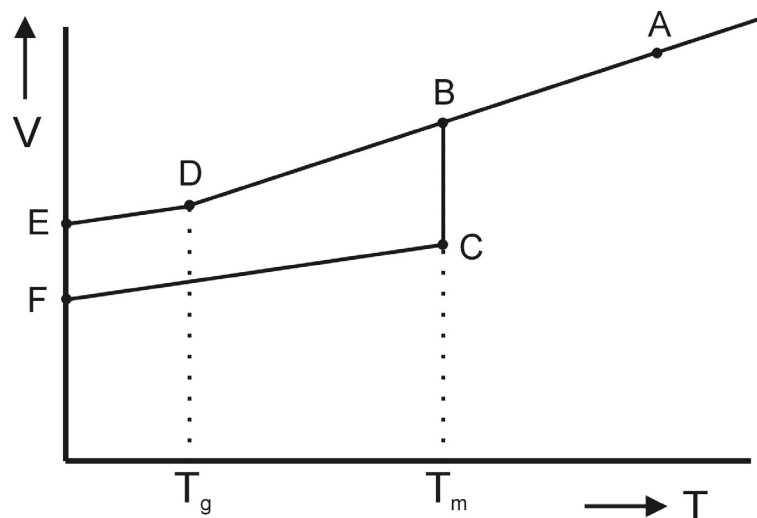


Figure 2.7: Volume expansion as a function of temperature

In a material which is unable to crystallize (as for instance glass or polymers) there is no jump in the volume of the material. When heated, this material follows the line EDDBA and goes into a rubbery state at the T_g (D), after which it will slowly become a liquid. From the T_g it already has the expansion coefficient of the liquid material. The T_g is always lower than the T_m of a material.

When heating a polymer to its T_g the polymer chains become mobile and the molecules with a dipole-moment μ_0 can be aligned by an applied electric field. For small poling fields, $\mu F / kT < 1$, equation (2-4) can be rewritten to (when β_{zzz} is the dominant part in β),

$$\chi_{zzz}^{(2)} = N\beta \frac{\mu_0 F}{5kT} = 3\chi_{xxz}^{(2)} \quad (2-10)$$

in which k is the constant of Boltzmann, T the absolute temperature and F the local poling field, which is equal to $F = \varepsilon_r E / (2\varepsilon_r + \varepsilon_u)$, with ε_r and ε_u the limiting low and high frequency permittivities.

The better the dipole is aligned by the electrical field applied ($\mu_0 F$), the larger the susceptibility tensors for the macroscopic effect will be.

From equation (2-10) it can be seen that during poling two effects occur. The term $\mu_0 F$ is the driving force to align the dipole with a polarizability (β) and the of thermal randomization (kT) that counteracts with this electrical force.

Because the mobility of the molecules diminishes below the T_g , the polar alignment can be fixed by cooling the sample. This effect of the alignment of the dipoles is given in figure 2.8.

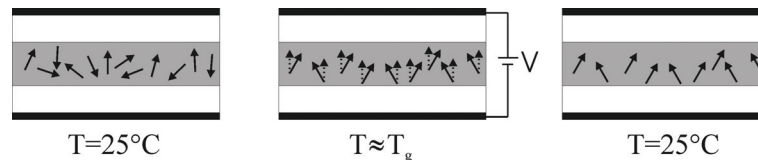


Figure 2.8: Schematic representation of the alignment of the dipoles

There are different techniques which can be used for poling a polymer layer.

The different techniques are described by [Bauer.1996] and the two most common used techniques for the application of a high voltage are:

1. Electrode poling

- Electrode poling is a technique in which the layer that has to be poled is sandwiched between two electrodes, over which a voltage can be applied. This can be done over a large area or the electrode can be patterned first so the poling can occur locally.

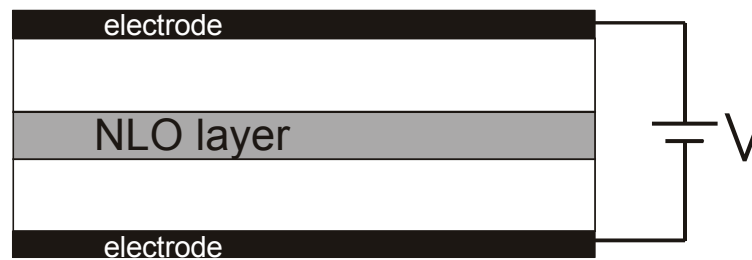


Figure 2.9: Schematic view of electrode poling

2. Corona poling

- A corona poling setup basically consists of a sharp needle or a wire placed above the layer to be poled. The bottom of this sample should be metallized and the electrical field is formed between the bottom electrode and a surface charge consisting of ions. These ions are formed by the needle or wire at which air breaks down, creating ions accelerating toward the polymer film. The danger of damaging the complete layer, caused by a defect somewhere in the layer, is low because transportation of current along the surface of the polymer is almost impossible (the polymer film is a very poor conductor)

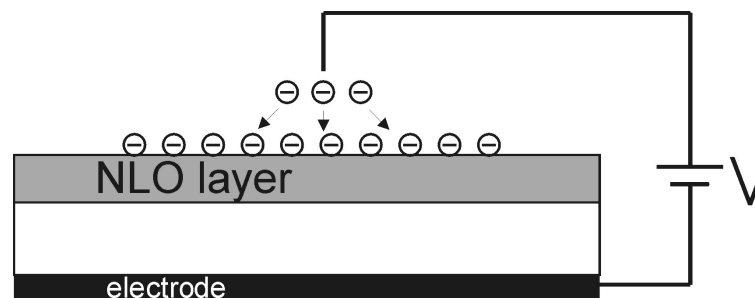


Figure 2.10: Schematic view of corona poling

In the devices discussed in this thesis, a form of electrode poling is used. The top electrode of the device is used for both operating and poling of the MR.

There are different models for the behaviour of the molecules under the influence of an electrical field. [Havinga.1979] and [Firestone.1995] both describe the theoretical principles of the poling-process. As was already shown before, the most important parameter in the poling-process is the angle (θ) that the dipole makes with the applied electric field. As long as the dipole isn't aligned maximally (for a given electrical field), this angle will change and with this change the electrical current that flows to compensate the induced surface charge will also change. This current is a good indication of the amount of poling reached for a given electrical field. Schematically a poling process is given in figure 2.11.

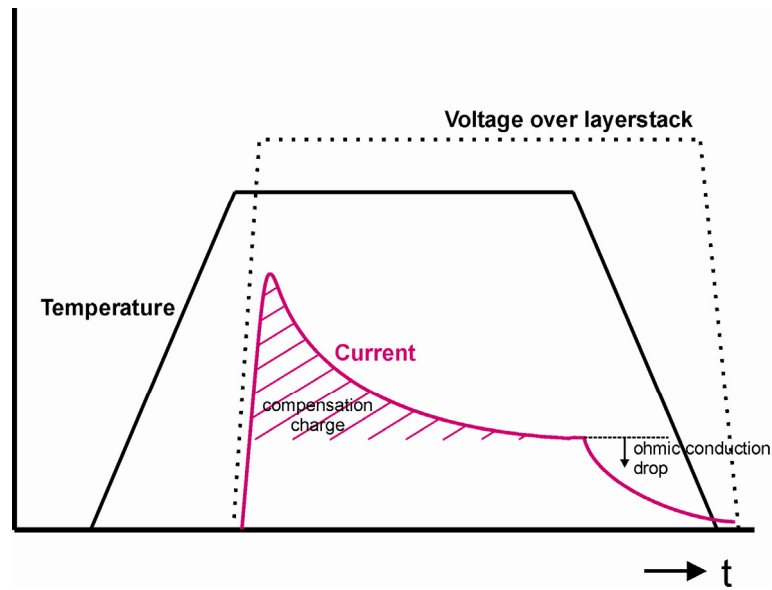


Figure 2.11: Schematic representation of the poling process

The device is first heated up to slightly below the T_g , after which an electrical field in the order of $100 \text{ V}/\mu\text{m}$ [Diemeer.2003] is applied. When the electrical field is applied over the layer, the dipoles are aligned and for this alignment, compensation charge is needed in the layer. In addition there is ohmic conduction due to the relatively high mobility of charges in a polymer in its rubbery phase. In the beginning a lot of charge is needed (because a large number of dipoles are aligning) and during the poling the amount of charge needed will reduce when most of the dipoles are aligned. Therefore the current will reduce and it will drop even further when the layer is cooled down because the ohmic conduction will drop.

The poling of the NLO layer is necessary to induce a macroscopic nonlinear effect, but one of the disadvantages of poling is that some additional waveguide losses can be introduced. These losses are caused by scattering of optical power from poling-induced in-homogeneities in the material. Because there is a difference in the indices of refraction for the TM and TE polarization ($\delta n_z, \delta n_x, \delta n_y$), the optical loss is polarization dependent. The amount of scattered optical power is proportional to λ^{-4} and $(\delta V)^2$ [Teng.1995] in which δV is the average volume of an in-homogeneity in the layer and λ is the wavelength of light in the NLO material. In large poling-fields the waveguide loss per unit length (γ_i) is for both y and z direction proportional to r_{33}^4 . For lower poling-fields the TM waveguide loss is approximately 4 times larger than the TE loss [Teng.1995].

$$\gamma_z \cong 4\gamma_y \quad (2-11)$$

[Teng.1995] describes the origin of these losses which can roughly be divided in three types of in-homogeneities of which two can be caused by poling.

1. The first type represents small domains which are distributed close to one another. In the NLO polymer, these domains could be tiny volumes of NLO moieties which have a certain preferred group orientation. This type of domains can be caused by poling but can also result from the evaporation of the solvent from a spin coated film, leaving behind free volume in the polymer and texture on the surface of the film.
2. The second type are large-volume defects (a few micrometers in diameter) and normally far away from each other (a few millimeters or more). These defects can be caused by aggregation of the polymer in the solution or air bubbles during spincoating.
3. The third type of in-homogeneities is caused by a depression of the top electrode over weak spots of the polymer film due to the induced electrostatic force during the poling.

A possible solution to minimize the poling induced loss is to find NLO chromophores with relatively isotropic first order molecular susceptibility ($\alpha_{xx} \cong \alpha_{yy} \cong \alpha_{zz}$), where n_x , n_y and n_z are relatively independent of the orientation of the NLO moieties.

Another issue to consider in the poling process, is the photochemical stability of the NLO chromophores. Under the influence of singlet oxygen and free radical pathways [Dalton.2001], the photochemical decomposition of the chromophores can occur. Preventing the formation of singlet oxygen during poling or preventing the oxygen from reaching the NLO layer should prevent this decomposition. Preventing the formation is the easiest solution to implement in a fabrication process by poling in an enclosure free of oxygen. The enclosure can be filled with nitrogen during poling.

2.2.6 Electric fields in layerstacks

Because an electric field should change the properties of the MR, it is also very important to know what the electrical properties of the surrounding layers are. Using materials with very different electrical properties might result in electrical drift phenomena (with a DC field applied) due to accumulation of charges at the interfaces of these materials. This effect is called the Maxwell-Wagner effect and is described in [Anderson.1964].

To analyze the behaviour of a layer stack with different properties, a two layer stack can be analyzed [Anderson.1964].

THEORY

This stack consists of two layers “i” and “j” with different properties sandwiched between two electrodes with a surface A. The important properties are the dielectric constant $\epsilon_{i,j}$, the conductivity $\sigma_{i,j}$, and the thickness of the layer $d_{i,j}$.

Each layer can be considered as a resistance and capacitance in parallel. The resistance and capacitance of each layer are given by

$$R_{i,j} = \frac{d_{i,j}}{A\sigma_{i,j}} \text{ and } C_{i,j} = \frac{\epsilon_{i,j}A}{d_{i,j}} \quad (2-12)$$

Schematically the electrical representation of the two layerstack is given in figure 2.12.

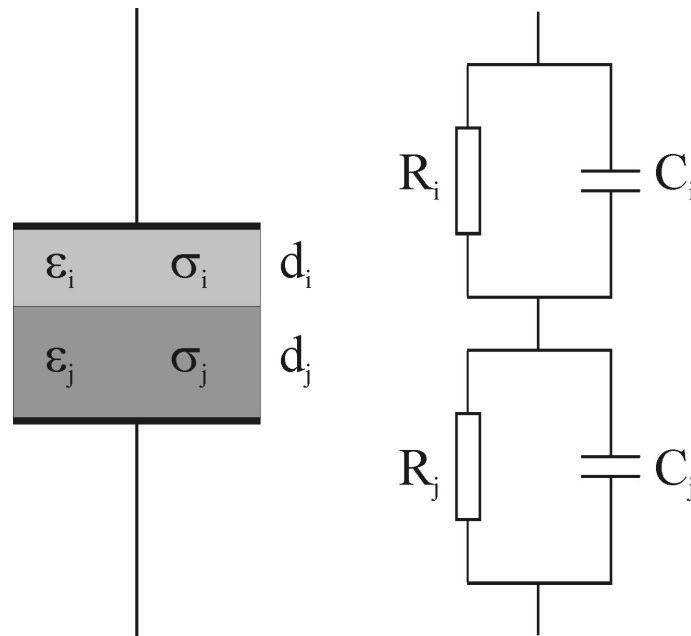


Figure 2.12: Electrical equivalent of two layerstack between two electrodes

There are two interesting situations for this layer stack. These are the field distributions during poling and switching. For switching the initial voltage distribution can be considered. For layer “i” this is given by [Diemeer.2004]:

$$V_{i0} = V \frac{C_j}{C_i + C_j} \quad (2-13)$$

During poling the field is applied for a longer time and currents will induce charge build-up at the interfaces. The voltage over layer “i” as a function of time is given by [Diemeer.2004]:

$$V_i = V_{i\infty} \left(1 - \left(1 - \frac{\tau_j}{\tau} \right) \exp\left(\frac{-t}{\tau}\right) \right) \quad (2-14)$$

in which

$$V_{i\infty} = V \frac{R_i}{R_i + R_j} \quad (2-15)$$

is the voltage across layer i for time $t \rightarrow \infty$

$$\tau_{i,j} = R_{i,j} C_{i,j} = \frac{\varepsilon_{i,j}}{\sigma_{i,j}} \quad (2-16)$$

is the relaxation time of layer i,j and

$$\tau = (C_i + C_j) \frac{1}{\frac{1}{R_i} + \frac{1}{R_j}} = \frac{\frac{\varepsilon_i}{d_i} + \frac{\varepsilon_j}{d_j}}{\frac{\sigma_i}{d_i} + \frac{\sigma_j}{d_j}} \quad (2-17)$$

is the relaxation time of the complete multilayer.

It can be seen from the previous that the switching behaviour is only determined by the capacitance of the layers and that the effectiveness of poling (which is a process over a longer time $t \rightarrow \infty$) only depends on the resistance of the different layers.

The model given here for two layers can easily be extended to more layers. It is used here to see the importance of the different parameters on the total field.

All common polymers are dielectrics and because the dielectric constant in glassy polymers is not widely different from the refractive index squared [Diemeer.2004] the capacitance of the different layers will be close to each other, because refractive indices are also. The voltage during switching or modulation is therefore distributed evenly over the different layers.

During poling the resistivity of the layers becomes important. To get a high electric field in the ringlayer its resistivity should be high compared to the layers surrounding it. A

characterization-setup to measure this resistivity is described in the characterization chapter. (chapter 5.1.2).

2.2.7 Comparison to organic materials

In EO modulators roughly two classes of materials can be distinguished. These two classes are the organic and inorganic materials. Two very good examples of inorganic materials are for instance LiNbO₃ or GaAs. The use of organic materials can have large benefits compared to inorganic materials in many aspects.

Schematically the differences between the two different types of materials are given in table 2.1 [Hornak.1992].

Physical and device property	Ti:Lithium niobate	Organic polymers
Electro-optic coefficient, pm/V	32	10-50*
Dielectric constant	28	4
Loss, dB/cm at $\lambda=1.3\mu\text{m}$	0.1	0.2-0.5
Bandwidth-length product, GHz·cm	10	120
Crystal growth temperature, °C	1000	NA
Waveguide processing temperature, °C	1000	<300
Waveguide processing time, hours	10	1
Multiple layers possible	No (vertical stacking of MR not possible)	Yes
Fabrication and processing	More complicated equipment needed for the fabrication	Simple fabrication because of spincoating of the layers

* Dependent on poling field and temperature

Table 2.1: Comparison of LiNbO₃ and EO polymers [Hornak.1992]

The most important parameters from table 2.1 are the difference in dielectric constant and the simpler fabrication and processing of the polymers.

As a rule of thumb in RF design it is stated that if no feature of the electrode structure is longer than 10% of the electrical wavelength, the electrode can be used as a lumped element. Because of the relatively low dielectric constant of organic materials, the electrical wavelength is larger than for inorganic materials. This allows higher frequency modulation with lumped element electrodes on organic materials than on inorganic materials.

Besides the easy fabrication and, advantageous design issues there are also a few drawbacks to polymers compared to LiNbO_3 .

The first drawback is the dipole alignment issue. To gain a net NLO effect in the polymer layer, the layer has to be poled which is a very critical fabrication step.

A second large drawback is the limited stability of the NLO polymers used in these modulators. The stability of the layer is influenced by processes of de-poling and photochemical degradation [Ren.2000], which will be shown in chapter 5.3.

2.3 Ringresonator

2.3.1 Operation description

The most important part of the modulator is the MR. This resonator consists of a circular waveguide with one or two straight port-waveguides coupled to it. Schematically this is shown in figure 2.13.

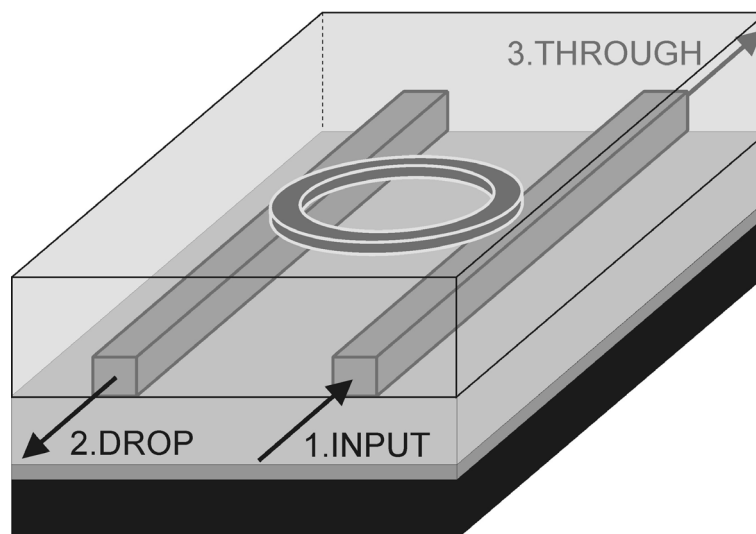


Figure 2.13: Schematic 3D image of the MR with two port-waveguides

The waveguides are not directly connected to the MR, but there is a small separation between them. When light is coupled in at port 1 of the waveguide a fraction (κ_1) of the light is coupled to the MR. The amount of light that is coupled in depends strongly on the separation between MR and waveguide. After half a roundtrip, a fraction (κ_2) of the light in the MR is coupled to the drop waveguide. The rest of the light completes the roundtrip and if a whole number of effective wavelengths fits in the MR the light will interfere constructively with light coupled from the waveguide to the MR. The amount of optical field in the MR will

build-up and a part of this field is coupled to the drop port. If the build-up of field in the MR is large enough almost the complete optical input intensity can be coupled to the drop port. The intensities at output 2 and 3 have the shape as in figure 2.14.

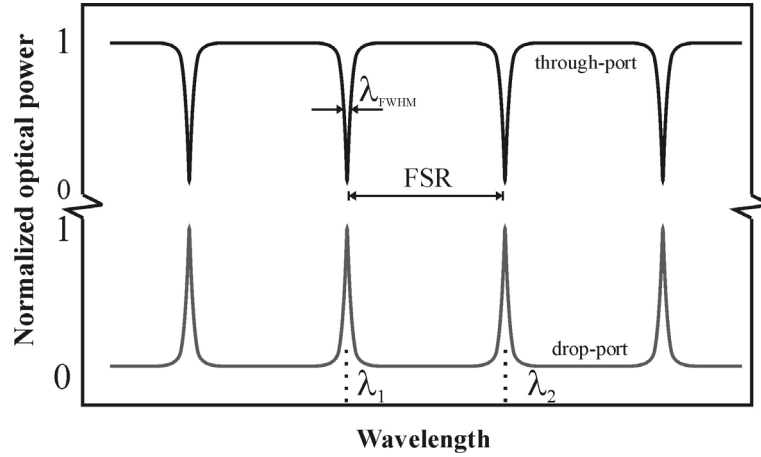


Figure 2.14: Schematic representation of a through and drop port spectrum

Figure 2.14 shows a schematic spectrum of the through and drop port of an MR. In this figure the following parameters are given.

- $\Delta\lambda_{FWHM}$ = the Full Width at Half Maximum (FWHM) of the resonance peak
- λ_1 and λ_2 are two neighbouring resonance wavelengths
- FSR = Free Spectral Range of the MR

To describe the behaviour of an MR, a number of useful parameters can be calculated/determined.

The first parameter of interest is the Free Spectral Range (FSR).

The FSR can be calculated from

$$FSR = \frac{\lambda_1 \lambda_2}{2\pi R n_g} \approx \frac{\lambda_r^2}{2\pi R n_g} \quad (2-18)$$

in which λ_1 and λ_2 are two neighbouring resonance wavelengths, λ_r is the resonance wavelength, R is the radius of the MR and n_g is the group index of the mode in the MR. This group index is given by [Madsen.1999],

$$n_g = n_e(\lambda_0) - \lambda_0 \left. \frac{dn_e}{d\lambda} \right|_{\lambda_0} \quad (2-19)$$

In which n_e is the effective index of the optical mode in the MR and the second term in equation (2-19) represents the dispersion in the MR. For materials with zero dispersion around λ_0 the term $dn_e/d\lambda$ is zero.

The FSR is a parameter which is determined by the geometry and material choice of the MR and is therefore “independent” of the fabrication process. An important parameter that determines the behaviour of the MR is the width of the resonance peaks. A relative value for this width is given by the finesse (F), which is defined as the amount of peaks/dips fitting in one free spectral range.

$$F = \frac{FSR}{\Delta\lambda_{FWHM}} \quad (2-20)$$

When one is interested in the absolute wavelength selectivity of the MR a good parameter is the quality factor (Q) of the MR, which is defined as.

$$Q = \frac{\lambda}{\Delta\lambda_{FWHM}} \quad (2-21)$$

The FSR is a parameter which can be calculated before the device is fabricated. The finesse and quality factor can be estimated from the losses in the MR.

One way to get an estimate for the finesse is by calculating the average number of roundtrips that a photon propagates in the MR. This number of roundtrips (m) is defined as the number of roundtrips after which the photon energy has decreased by a factor $1/e$ [Verdeyen.1981]. If the optical loss in the MR is known, ‘m’ can be calculated. The relation between m and F is [Klunder.2002]:

$$m = \frac{F}{2\pi} \quad (2-22)$$

When using the MR as an EO modulator, a single wavelength optical input signal is used, which is tuned such that the operating wavelength is at the steepest slope of one of the dips in the through port spectrum. Applying a voltage (electrical field) over the MR induces a shift in

the position of the resonance peak, which results in a change in intensity at the through port output (see figure 2.15).

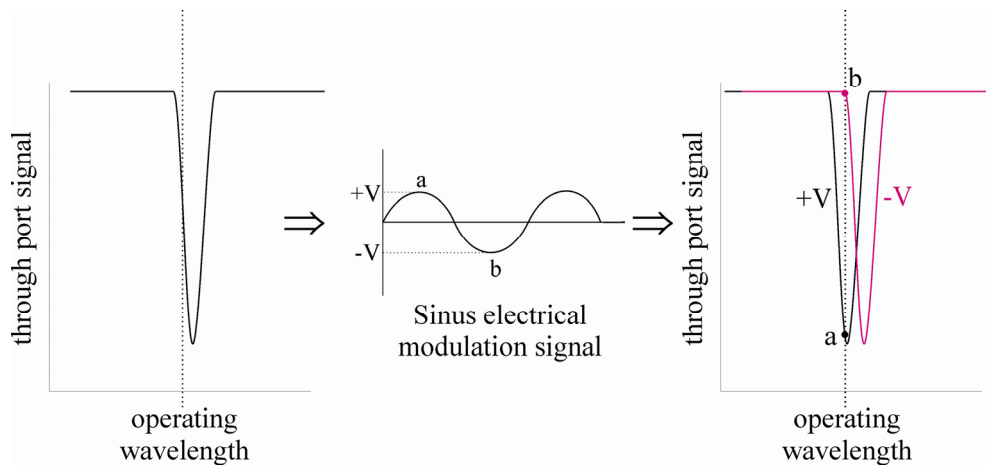


Figure 2.15: Modulation on the flank of a dip in the spectrum

From figure 2.15 it can be seen that at the steepest slope a small change in the properties of the MR (resulting in a shift of the resonance peak) results in a large change of the through port intensity. A large finesse is needed to have a steep slope on the flank of the dip. Equation (2-22) already shows that for a high finesse the number of roundtrips (m) also is large. This can only be achieved in an MR with low loss. Mathematically the MR can be simplified to a number of optical building blocks of which the behaviour can be expressed in mathematical functions. The schematic representation of the MR is given in figure 2.16 [Klein.2002] [Madsen.1999].

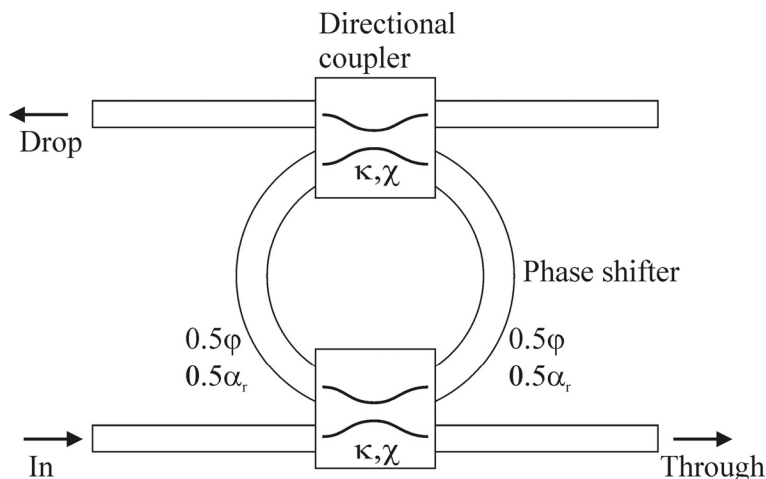


Figure 2.16: MR device represented by building blocks

The total device consists of two directional couplers (the coupling from waveguide to MR and vice versa) and two loss inducing phase shifters (= half a roundtrip through the MR).

The directional couplers are described by two parameters:

- κ , which is the power coupling constant (the amount of optical power coupled from waveguide to MR, or vice versa, by one of the couplers)
- χ is the excess loss within the coupler (assumed to be zero).

The MR is described by two phase shifters, each inducing a phase shift of 0.5φ and a loss of $0.5 \alpha_r$, in which φ is the phase shift and α_r is the loss of a single roundtrip through the MR.

α_r can also be written as $\alpha_r = 2\pi R \alpha_{LIN}$, where R is the radius of the MR and α_{LIN} is the linear attenuation constant. Mostly the ringlosses are given in dB/cm (α_{dB}) and α_{LIN} can be calculated from that value by $\alpha_{LIN} = \frac{\alpha_{dB}}{20 \log(e)} \approx \frac{\alpha_{dB}}{8.68}$ [Klein.2002] in cm^{-1} valid for the optical field attenuation. For optical powers the $\log(e)$ factor is multiplied by 10 instead of 20. With these values, a finesse factor (F_c) [Madsen.1999] can be calculated.

$$F_c = \frac{4\mu^2 e^{-\alpha_r}}{(1 - \mu^2 e^{-\alpha_r})^2} \quad (2-23)$$

in which $\mu = \sqrt{1 - \kappa^2}$.

With this finesse factor the finesse can be calculated from

$$F = \frac{\pi}{2 \arcsin\left(\frac{1}{\sqrt{F_c}}\right)} \quad (2-24)$$

As can be seen from equation (2-24) the value of F_c must be large in order to get a high finesse. As was shown before the loss should be low for high finesse rings. With α_r small, μ has to be close to 1 in order to get F_c as large as possible. High finesse rings are therefore made with low loss rings combined with small coupling constants.

2.3.2 Thermal/electrical dependence

The properties of the MR (realized with EO polymers) can be changed by either applying an electric field or changing the temperature of the MR. In both situations the same relation between the changes in the MR and the shift of the resonance peak can be found. This relation

THEORY

can be found by considering the fact that the total phase shift of a wave travelling in the MR must be a multiple of 2π after a roundtrip to build up resonance. This can be described by

$$\frac{\text{length of roundtrip}}{\lambda} = \frac{2\pi R n_g}{\lambda} = l \quad l = \text{integer} \quad (2-25)$$

Assuming that R is constant when changing the properties of the MR it can be seen that a change in the group index n_g results in a shift in the resonance wavelength.

$$\frac{2\pi R(n_g + \Delta n_g)}{(\lambda + \delta\lambda)} = l = \frac{2\pi R n_g}{\lambda} \quad (2-26)$$

Resulting in,

$$\frac{\lambda \Delta n_g}{n_g} = \delta\lambda \quad (2-27)$$

The relationships between the change of the index of the MR material, Δn_{ring} , and either an electrical field or temperature change can be found in previous paragraphs (paragraph 2.2.2 and 2.2.4). The change in n_g in equation (2-27) is dependent of the amount of optical field in the ringresonator. Because of the “high” index contrast between MR and cladding the change in n_g is almost equal to Δn_{ring} .

As an example a thermal and electrical tuning example is given.

From paragraph 2.2.2 it can be seen that $\frac{dn}{dT} \approx -10^{-4}$. This means that each degree in temperature change induces a change of 10^{-4} in refractive index. At a wavelength of 1550 nm and an optical mode with an effective index of 1.48 this induces a change in resonance wavelength of approximately 100 nm. For an MR with a relatively high finesse the width of a dip/peak in the spectrum is very often smaller than 100 nm. This means on one hand that the resonance behaviour of the MR can be tuned thermally very easy, but also the temperature must be controlled very carefully in order to keep λ_r stable.

From equation (2-9) the change in refractive index caused by an electrical field can be calculated. As an example the $\delta\lambda$ caused by a change in refractive index Δn_3 is calculated. For r_{33} a realistic value of 10 pm/V is assumed and a voltage of 1 Volt is applied over a layerstack

of 10 μm . This results in a shift of the resonance peak of only $1.7 \cdot 10^{-3}$ nm at a resonance wavelength of 1550 nm.

As can be seen from these two examples it is very important to have rings with a very high finesse to let the small effect (in case of electrical modulation) in wavelength shift have a large effect in the output of the MR.

Another issue to consider here is the uncertainty in the exact position of the resonance peak after fabricating an MR. For using the MR as an EO modulator the wavelength has to be set to a steep flank of the MRs dip or peak. This can be done by either changing the lightsource or the MR. For a fixed lightsource the properties of the MR have to be changed in order to shift the resonance wavelength. To that end a bias signal must be applied to the MR. From the two calculated examples it can be seen that it is very difficult to tune an MR electrically over an entire FSR (\sim a few nm, depending on the exact MR properties). However, the biasing of the MR therefore can be done thermally by either placing the entire device on some kind of a heater or realize a heater to locally heat the MR. With a temperature change of 20°C the resonance wavelength can already be tuned over a few nm.

2.3.3 Bandwidth limitations

One of the issues when using an MR as a high-speed modulator is the fact that the MR needs some time to build up the optical field. One roundtrip of the light through the MR takes,

$$\tau_{\text{Roundtrip}} = \frac{2\pi R}{v} = \frac{2\pi R n_g}{c}. \quad (2-28)$$

in which v is the speed of the light in the MR and c is the speed of light in vacuum. For an MR to build up resonance, multiple roundtrips are needed. The total/characteristic time for the MR to build up resonance is also called the cavity ring-down time τ_{cav} [Verdeyen.1981] and with (2-22) this can be written as

$$\tau_{\text{cav}} = m \cdot \tau_{\text{Roundtrip}} = m \frac{2\pi R n_g}{c} = \frac{F R n_g}{c} \quad (2-29)$$

THEORY

The cavity ring-down time is proportional to the quality factor and with the help of equation (2-18) (2-20) (2-21) (2-22) the following relation can be found.

$$\tau_{cav} = \frac{\lambda Q}{2\pi c} \quad (2-30)$$

The quality factor of an MR is strongly determined by the fabrication process. Very high quality MRs give very steep through and drop responses, but have the disadvantage that the cavity ring-down time increases. There is therefore a trade-off between sensitivity of the MR vs. modulation bandwidth. As an example an MR with an effective index of 1.48 is considered and for different radii the $1/\tau_{cav}$ is calculated as a function of finesse. These values are given in figure 2.17.

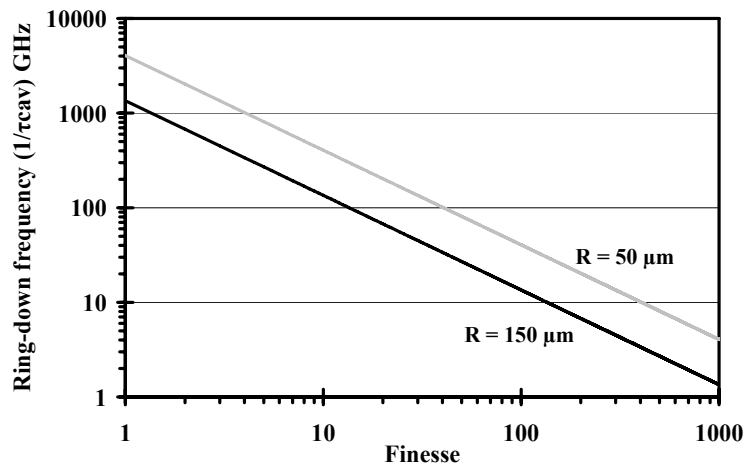


Figure 2.17: $1/\tau_{cav}$ value vs. finesse

The values chosen in the example are realistic values for MR's discussed in this thesis. Typical finesse values for realized polymer MR are $\sim < 200$ [Chen.2004]. It can then be seen from figure 2.17 that restrictions due to the finesse are only relevant for modulation frequencies well above 1 GHz.

2.4 Mach-Zehnder Interferometer

2.4.1 Operation description

To increase the effect of the phase change induced by the MR, it can be connected to an MZI. This paragraph will describe the MZI and the use of the MR in this device.

The MZI is basically a waveguide, which is split into two waveguides after which these two waveguides are recombined again.

Schematically this is shown for the TE_{00} mode in figure 2.18.

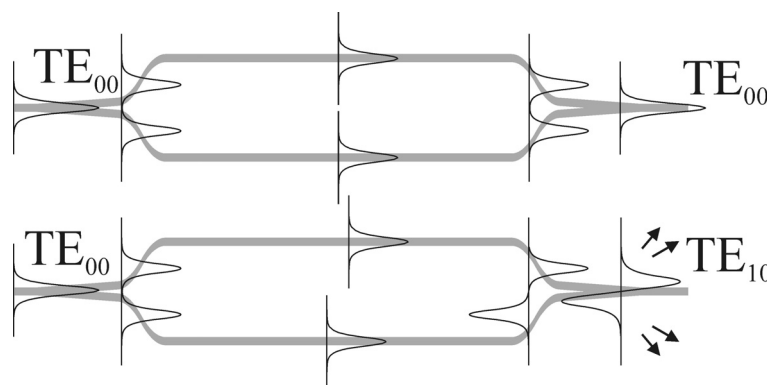


Figure 2.18: Schematic representation interference in an MZI

By inducing a phase change in one of the two branches of the MZI the recombination of the optical paths can result in a guided zero order mode or an unguided first order mode.

If one of the optical paths experiences a phase change of π compared to the other, the two zero order modes recombine as a first order mode. If the waveguide after the MZI is designed such that it only sustains the zero order mode, the first order mode will radiate away. In this way an intensity modulator can be built by switching between these two states.

The intensity at the output waveguide can then be written as:

$$I_{out} = I_{in} \cdot \cos^2\left(\frac{\Delta\phi}{2}\right) \quad (2-31)$$

in which I_{in} is the optical input intensity, I_{out} the intensity at the output and $\Delta\phi$ the phase difference between the two branches.

If an MR is placed on one of the branches of an MZI there is no drop waveguide to couple the light to. The through port spectrum of the MR will have no dips in the ideal lossless case. The interesting parameter in that case is the phase shift induced by the MR.

This parameter depends strongly on the amount of light coupled from the waveguide to the MR. In the ideal case (ringloss = zero), a high finesse resonance can build up in the MR with an infinitesimal small amount of light coupled from the waveguide to the MR as can be seen from equation (2-24). The fraction of light coupled from waveguide to the MR also determines the shape of the phase change spectrum. From [Roeloffzen.2002] it follows that for lower coupling constants the phase change near the resonance wavelength is much steeper than for larger coupling constants. Figure 2.19 gives an impression of the phase response for a lossless MR for three different coupling constants [Madsen.1999] [Roeloffzen.2002].

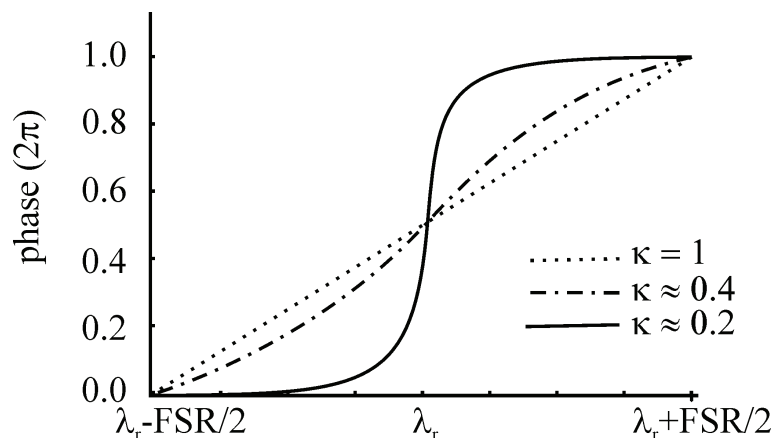


Figure 2.19: Impression of phase response of a lossless MR for three different coupling constants

It can be seen that it is important to have the coupling from the waveguide to the MR as low as possible to have the slope as steep as possible. In addition the MR-loss should also be low in order to build up resonance. The complete device is given schematically in figure 2.20.

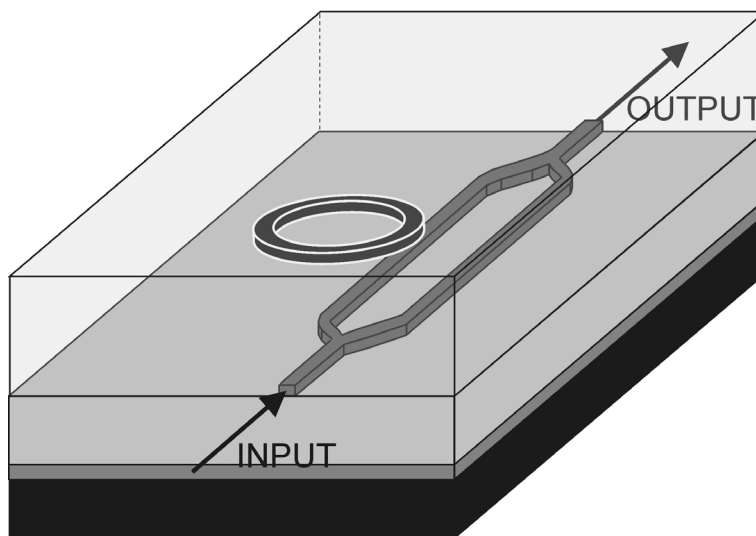


Figure 2.20: Schematic 3D image of the MZI with MR

With the MR placed on top of one of the branches of the MZI, a phase change π can be easily induced by bringing the MR in resonance. If the phase response of the MR is steep (see figure 2.19), only a small change in the refractive index is needed to bring the MR in and out of resonance and therefore a sensitive modulator can be build. By designing and fabricating the MZI such that both arms of the MZI are identical there is no wavelength dependence of the output induced by the MZI. The changes in the output are induced by changes in the MR only.

2.4.2 Thermal/electrical dependence

The dependence of the output on changes in temperature or electrical field can be found by looking at the phase in each of the two branches of the MZI.

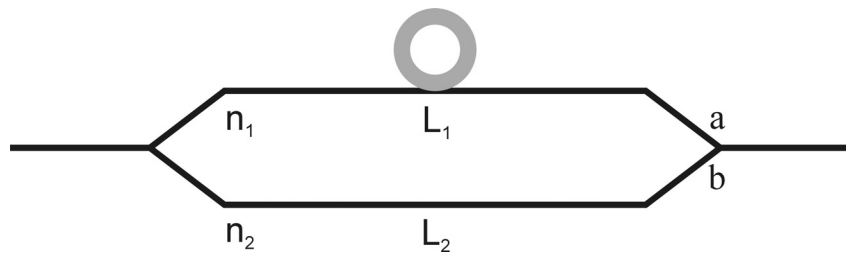


Figure 2.21: Schematic picture of parameters needed to calculate output MZI with MR

The phase change $\Delta\phi$ in equation (2-31) is the change in phase between point a and b in figure 2.21. $\Delta\phi$ can be found by using the following parameters.

- $\Delta\phi_1$ = the phase change induced by branch 1 of the MZI
- $\Delta\phi_2$ = the phase change induced by branch 2 of the MZI
- $\Delta\phi_R$ = the phase change induced by the MR
- L_1, L_2 = the length of branch 1, 2
- n_1, n_2 = refractive indices of the modes in branch 1, 2

The difference in phase between point 'a' and 'b' is given by.

$$\Delta\phi = \frac{n_1 L_1 2\pi}{\lambda} + \Delta\phi_R - \frac{n_2 L_2 2\pi}{\lambda} \quad (2-32)$$

THEORY

It can be seen that in a symmetrical MZI ($n_1=n_2$ and $L_1=L_2$) the change in the output amplitude is only determined by ϕ_r . Due to small errors in the fabrication process the realized MZI will not be completely symmetric. The asymmetry in the MZI is caused by a difference in the optical pathlength between the two branches.

This difference in optical pathlength ($n_1L_1-n_2L_2$) is caused by two effects.

- A difference between the effective refractive indices of the optical modes in the two branches.
 - o This difference can for instance be caused by a difference in waveguide width of the two branches.
- A physical length difference between the two paths (L_1-L_2).
 - o For instance caused by a fabrication error in the fabrication of the lithographic mask.

If the difference in path-length is only caused by a difference in the effective refractive indices of the optical modes (so $L_1=L_2=L$) the total phase difference can be kept to a minimum by keeping the MZI as small as possible (L is small in $(n_1-n_2)L$).

If the difference in path lengths is caused by a difference in the physical lengths of the paths (so $n_1=n_2=n$) making the MZI smaller has no effect on this path length difference ($n(L_1-L_2)$).

The MZI can be balanced by placing a heater on one of the branches and balancing it by changing the refractive index of this branch slightly. The maximum range of tuning needed is 2π because somewhere in that range both arms of the MZI are balanced. From paragraph 2.2.2 it can be seen that the thermo optic coefficient is approximately $1 \times 10^{-4} \text{ }^\circ\text{C}^{-1}$. Assuming that only one branch (of length L) is tuned, the phase change induced by a temperature change is given by:

$$\Delta\phi_r = \frac{1 \cdot 10^{-4} \Delta T \cdot L}{\lambda} 2\pi \quad (2-33)$$

From equation (2-33) it can be seen that an MZI of 1 cm only needs approximately 1.5°C of temperature change of one of the branches to tune over 2π (for a wavelength of 1550 nm). This shows that the MZI is sensitive for temperature changes and a very low thermal bias can be used to balance the MZI.

Making the MZI as short as possible increases the required thermal bias to balance the MZI ($\Delta\phi_T$ becomes smaller if L becomes smaller), but also decreases the sensitivity for thermal changes in the ambient temperature.

3 Device design

In chapter 1 the choice for a vertically stacked MR was motivated. This chapter will deal with the design of the MR structure. The different design choices will be motivated and structure parameters will be chosen.

The first step in device design is the choice of materials to be used in the device to be designed as shown in figure 3.1.

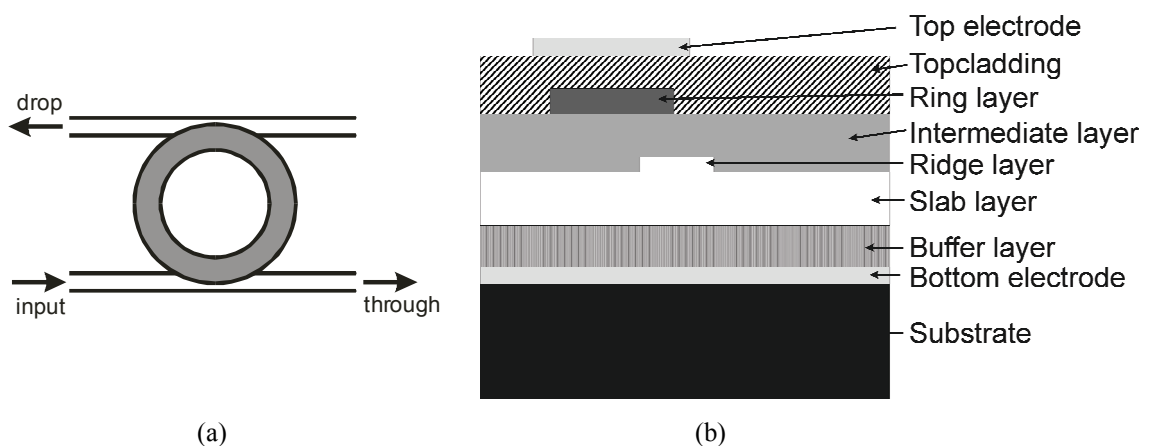


Figure 3.1: Top view (a) and cross section (b) of the device to be designed

Although the second type of device (figure 2.1) is an MZI combined with an MR, the design will be done for a single MR as this is the most critical component of the MZI with MR.

In figure 3.1.b the layers for which materials must be chosen are given. The choices that are made in selecting the materials are explained in the next paragraph.

For each material two important parameters that determine its applicability are the refractive index of the material and its resistivity.

To get high electrical field strengths in the ringlayer when applying a voltage over the top and bottom electrode (for poling), the resistivity of all the layers should be in the same order of magnitude (or lower) as the resistivity of the ringlayer (see also chapter 2.2.6).

Besides the resistivity, the applicability of the different materials is also taken into account in the choice of materials. Applying planarized layers of different material on top of each other should be possible.

When all the materials are chosen, the dimensions of the different layers and structures are designed in the rest of the chapter.

3.1 *Choice of materials*

For fabrication simplicity a bottom electrode over the entire wafer is deposited (which makes polymers the most obvious choice for the rest of the layers because of their easy applicability on metal layers). A few demands are set for all the different layers. These demands are:

- The materials should be transparent at the wavelength where the MR has to operate, i.e. 1550 nm (and 850 nm in order to be able to use devices like these in the THz project).
- The material should be stackable with the different materials used in the device-realization.

The motivation for choosing materials for the different layers is given in this paragraph.

- Substrate
 - There are no special demands for the substrate. It is only a carrier for the rest of the layerstack and has to be rigid with a smooth surface. It is convenient when the thermal expansion of the substrate isn't too much different from the rest of the layers. Because of simplicity and availability a <100> silicon wafer is chosen.
- Bottom electrode
 - There are no other demands for this layer other than that it should form a conductive layer underneath the device. To keep fabrication as simple as possible a layer of gold is chosen (with a thin layer of chromium as a sticking layer)
- Buffer layer
 - The bufferlayer has to meet the following demands:
 - Its refractive index should be lower than the index of the slab- and ridgelayer.
 - It has to be thick enough for the mode in the waveguide should not sense the bottom electrode.
 - Its resistivity should be in the same order of magnitude (or preferably lower) than that of the ringlayer.
 - For this layer the commercially available methyl-silicone Glassclad PS233 from United Chemicals Technology is chosen because it has a low refractive index and a high electrical strength with a relatively low resistivity.

-
- Slab layer
 - For fabrication simplicity the slab layer and ridge layer are of the same material.
 - Ridge layer
 - The ridgelayer has to meet the following demands:
 - The refractive index of the ridge layer must be higher than that of the buffer- and intermediate-layer
 - The ridge layer must be defined in lateral direction to form a channel waveguide. Preferable this is done by direct photo-definition instead of etching.
 - For both the ridgelayer and the slablayer a negative resist (SU8 fabricated by MicroChem Corp.) is chosen because of its refractive index compatibility with the ringlayer, easy definability and low loss around 800, 1320 and 1550 nm (page 39 [Musa.2002]).
 - Intermediate layer
 - The demands for the intermediate layer are:
 - It should have a refractive index lower than the index of the ridgelayer.
 - Layer-thicknesses in a large range should be possible to realize in order to control the coupling from the waveguide to the MR from 0 to 1.
 - The optical loss of this layer should be low because absorption losses in this layer influence the loss of the optical mode propagating in the MR and therefore influence to finesse of the MR.
 - To keep the waveguide symmetrical and the fabrication simple the same material as the buffer-layer is chosen.
 - MR layer
 - To change the properties of the MR by applying an electrical field over it, the MR must be fabricated of an EO material. The material synthesized in the IST project NAIS for this purpose is the PolyMethylMethAcrylate-Disperse Red 1 (PMMA-DR1) polymer. The following issues about this material should be noted here:
 - Relative high EO coefficients are feasible [Michelotti.2003]
 - Material has relatively high photochemical stability [Gonzalez.2000]
 - Material has relatively high thermal stability. Glass transition temperature is around 130°C.

- The material has low-loss windows in the absorption spectrum around 1550 and 850 nm (see chapter 2.2.1)
- Top cladding
 - The top-cladding should have a relatively high refractive index-contrast with the ringlayer to keep bending-losses in the MR as low as possible.
 - Also optical transparency is important in order to keep the losses of the bendmode in the MR as low as possible.
 - For these reasons and for fabrication simplicity also here Glassclad is chosen.
- Top electrode
 - The top electrode should be patternable easily and should have a high conductivity. It is therefore made of gold, which can easily be etched (without any aggressive etchants). A thin layer of chromium can be used as a sticking layer. This thin layer can easily be etched by a short dip in a chromium etchant.

3.1.1 Material parameters

For the different materials that are used, the properties of the materials have to be determined in order to be able to design the entire structure. This paragraph will describe the determination of the different relevant material parameters.

For each material the following parameters will be determined

- Spincurve (layer-thickness versus spin-speed)
- Refractive index
- Resistivity

Glassclad

The commercial available material chosen for the buffer-, intermediate- and claddinglayer is a methyl-silicone resin fabricated by United Chemical Technologies and sold under the name PS233 Glassclad[®] RC. The molecular structure of Glassclad is based on methyl-silicone (given schematically in figure 3.2).

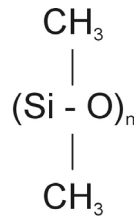


Figure 3.2: Molecular structure of a methyl-silicone

The PS233 material is dissolved in a 50% isopropanol solution.

By spin-coating layers at different spin-speeds on silicon wafers the spincurve can be determined. The layers were spin-coated (30 seconds), at various spinspeeds (as shown in table 3.1), with an acceleration of 3000 rpm/s and thermally cured on a hotplate of 150°C for 2 hours after a room temperature drying step of 1 ½ hours.

With a Woollam ellipsometer (chapter 5.1.1) the layerthickness and refractive index are measured and the values are given in table 3.1. The corresponding spincurve and refractive index vs. wavelength are given in figure 3.3 and figure 3.4.

Spinspeed (rpm)	Measured thickness (μm)	Refractive index at 1550 nm
1000	2.11	1.4077
2000	1.56	1.4066
3000	1.29	1.4076
4000	1.16	1.4075
5000	1.10	1.4075

Table 3.1: Measured layer-thickness and refractive index of Glassclad

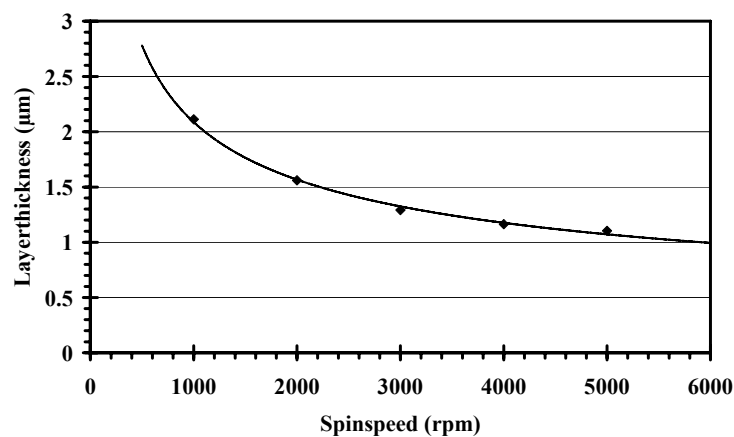


Figure 3.3: The spincurve of Glassclad

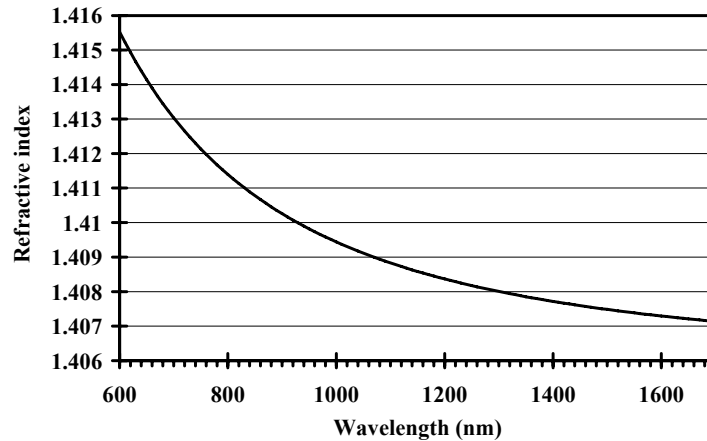


Figure 3.4: Refractive index dispersion of Glassclad as determined from the Cauchy parameters

From each layer also the resistivity of the layer is important and therefore this is measured with a setup as will be discussed in chapter 5.1.2. The resistivity is of importance at the temperature at which the sample is poled, because at this temperature a DC electric field is applied. In equation (2-13) it was shown that for the electrical field division during high frequency modulation, only the capacitance of the layer is important and the resistivity is only important when applying DC voltages (see chapter 2.2.6). The electrical field during poling will be something in the order of $120\text{V}/\mu\text{m}$.

At 130°C and an electrical field of $120\text{V}/\mu\text{m}$ the measured resistivity is $1.5 \cdot 10^{11} \Omega\text{m}$.

SU8

SU8 is a high refractive index, epoxy based photoresist designed for micromachining and other applications. It was originally developed and patented by IBM (US Patent No. 4882245 (1989) and others). The product is sold commercially by two companies (MicroChem Corp. (USA) and SOTEC Microsystems (Switzerland)). The resist consists of an epoxy resin and a photoacid generator dissolved in a solvent (i.e. γ -butyrolactone). The molecular structure of the epoxy is shown in figure 3.5.

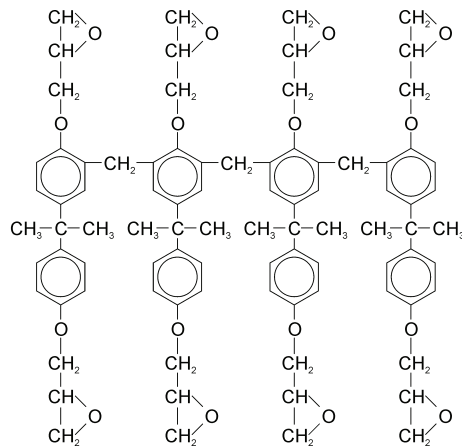


Figure 3.5: Molecular structure of the SU8 polymer

The 8 in the name SU8 comes from the 8 epoxy groups that take care of the cross-linking, which can be initiated when a catalyst for this process is present. This catalyst is an acid (HSbF_6), which is formed from the photoacid generator in the solution through the photochemical reaction given in figure 3.6.

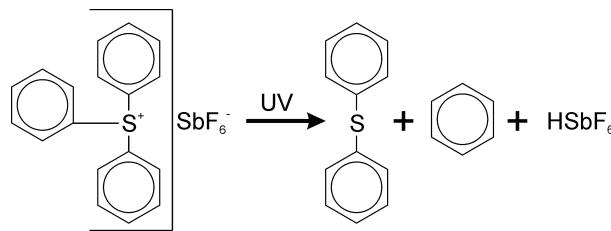


Figure 3.6: Schematic representation of the photochemical reaction of the photoacid generator

For the formation of the acid, the photoacid generator must be exposed to UV light, after which the cross-linking of the material can be thermally initiated by providing sufficient mobility of the SU8 molecules to react with each other.

After crosslinking of the epoxy groups, a dense network is formed, which is very resistant and is schematically shown in figure 3.7.

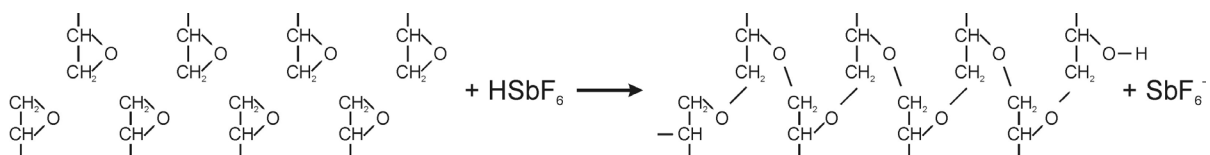


Figure 3.7: Crosslink reaction in SU8

The crosslinked SU8 is no longer soluble in organic developers and therefore the part of the polymer not exposed to UV light can be removed by developing in an organic developer.

SU8 is used in two of the layers of the device, meaning that the range of thicknesses to be spincoated must be relatively large (both slablayer and ridgelayer have to be spincoated from the same material). In order to vary the thickness of the material over a large range, the material is diluted to make thinner layers. The base material is SU8-25, which would give a layer-thickness off approximately 25 μm at spinspeeds around 3000 rpm (according to the product specifications by MicroChem Corp.). This material can be diluted with γ -butyrolactone (GBL) and for different dilutions the material properties are determined.

With the different solutions layers were spincoated on silicon wafers in the following steps

- Spincoat (30 seconds), at various spinspeeds, with an acceleration of 3000 rpm/s
- Thermally cure on a hotplate at 95°C for 3 minutes
- Apply a flood exposure of 1 minute on the Karl Zeuss MA55 maskaligner
- Thermally crosslink on a hotplate at 95°C for 3 minutes

The material properties for the different solutions are measured with a Woollam ellipsometer and given in table 3.2.

Figure 3.8 gives the spincurves for the different solutions.

	Layer-thickness (nm)				refractive index at 1550 nm			
SU8 : GBL ratio	2:1	1:1	1:4	1:6	2:1	1:1	1:4	1:6
Spinspeed (rpm)								
1000	5332	2048	335	223	1.572	1.572	1.576	1.575
2000	2569	1070	178	115	1.607	1.574	1.575	1.565
4000	1450	625	114	73	1.574	1.575	1.563	1.560

Table 3.2: Measured values of layer-thickness and refractive index for different solutions of SU8

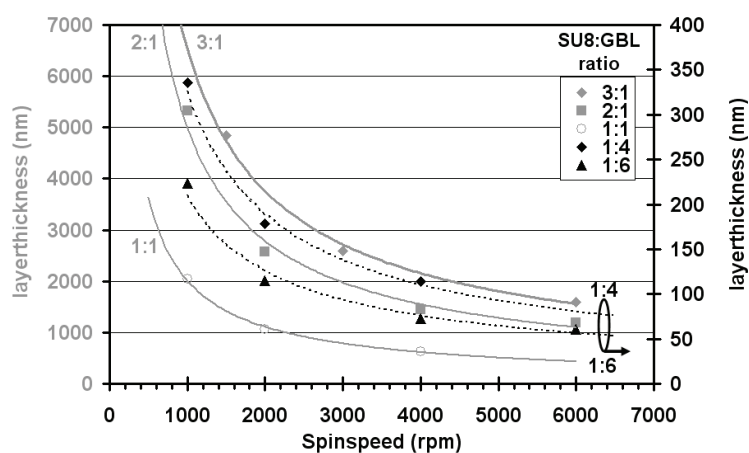


Figure 3.8: SU8 spincurve for different SU8:GBL mass-ratios

It can be seen from figure 3.8 that layer-thicknesses as thin as 60 nm can be spin-coated with this solution, which in undiluted form is used for 25 μm layers.

From all the different layers in figure 3.8 the Cauchy parameters are determined with the Woollam ellipsometer and an average of all these values is given in figure 3.9.

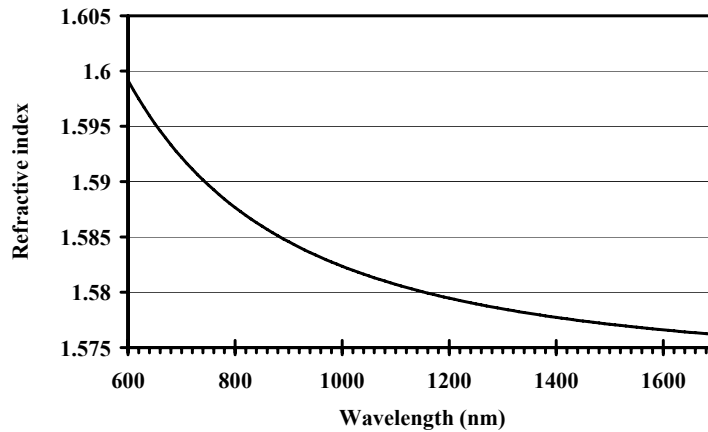


Figure 3.9: Average refractive index dispersion of SU8 layers

Also for SU8 the resistivity is measured at the glass transition temperature of PMMA-DR1 at an electric field of $120\text{V}/\mu\text{m}$. The measured resistivity was $9.2 \cdot 10^8 \Omega\text{m}$

PMMA-DR1

The ringlayer is fabricated from the PMMA-DR1 polymer, which is a combination of the monomer MethylMethAcrylate (MMA) and the NLO chromophore Disperse Red 1 (DR1). The structure of the DR1 molecule is given in figure 3.10.

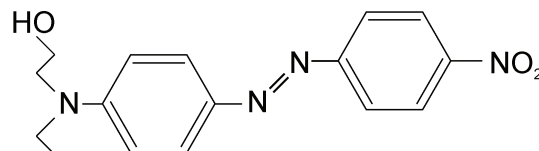


Figure 3.10: DR1 molecule

This DR1 molecule is coupled to a methacryloylchloride molecule to yield the molecule MMA-DR1. This molecule is given in figure 3.11.

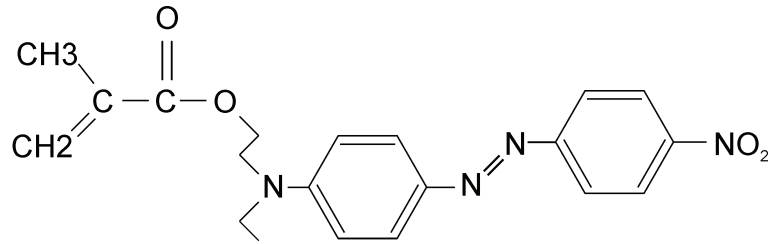


Figure 3.11: MMA-DR1 molecule

The EO polymer used was a polymer of 43% MMA-DR1 and 57% MMA.

This polymer mixture can be dissolved in 1,1,2 trichloroethane (1,1,2 TCE). The solution used had a concentration of 9% PMMA-DR1 in 1,1,2, TCE. On three silicon wafers a layer of PMMA-DR1 was spincoated (with an acceleration of 3000 rpm/s) at different spinspeeds (for 30 seconds). These layers were baked at 120°C for 2 hours to remove the solvent. With the Woollam ellipsometer the layerthickness and refractive index of these layers were measured and the spincurve is given in figure 3.12. The refractive index at 1550 nm was 1.606 and for different wavelengths the index is given in figure 3.13 (again calculated from the Cauchy parameters).

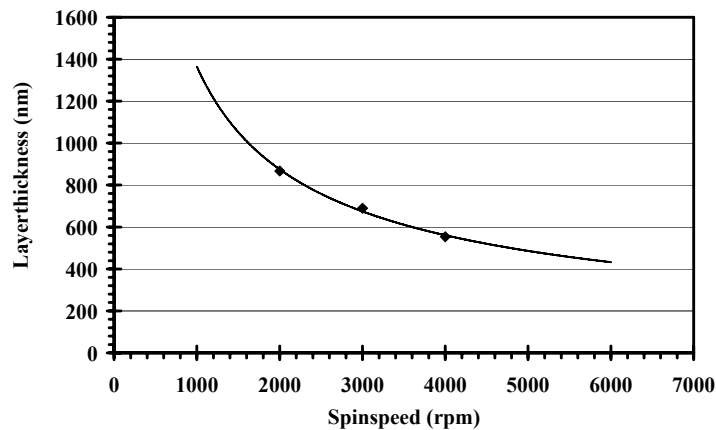


Figure 3.12: Measured layerthickness for different PMMA-DR1 layers as a function of spinspeed

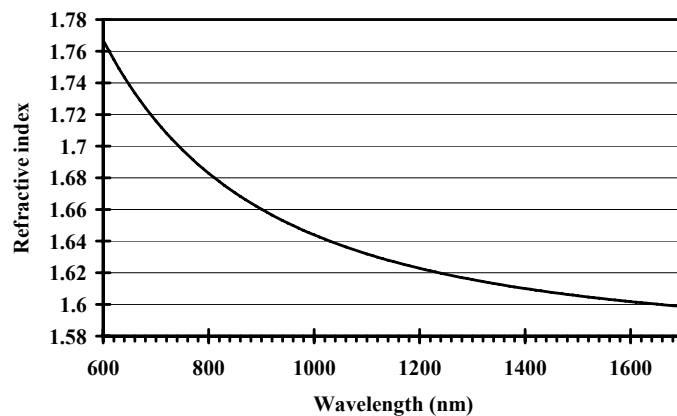


Figure 3.13: Refractive index unpoled PMMA-DR1 vs. wavelength

For PMMA-DR1 the resistivity is also measured around its glass transition temperature at 120 V/ μm and a value of $1.1 \cdot 10^{11} \Omega\text{m}$ is found.

It can be seen that the value for PMMA-DR1 is in the same order of magnitude as the resistivity of Glassclad and much larger than the resistivity of SU8. The electrical field will therefore be largely over the Glassclad and PMMA-DR1 layer.

3.2 Structure design

After the materials are chosen, the dimensions of the entire structure (shown in figure 3.14) can be determined. The design is split in waveguide, MR, total device and electrode design. As was already discussed in the introduction chapter, the design of the MR will be done for a wavelength of 1550 nm. All simulations in this chapter are therefore done for this wavelength.

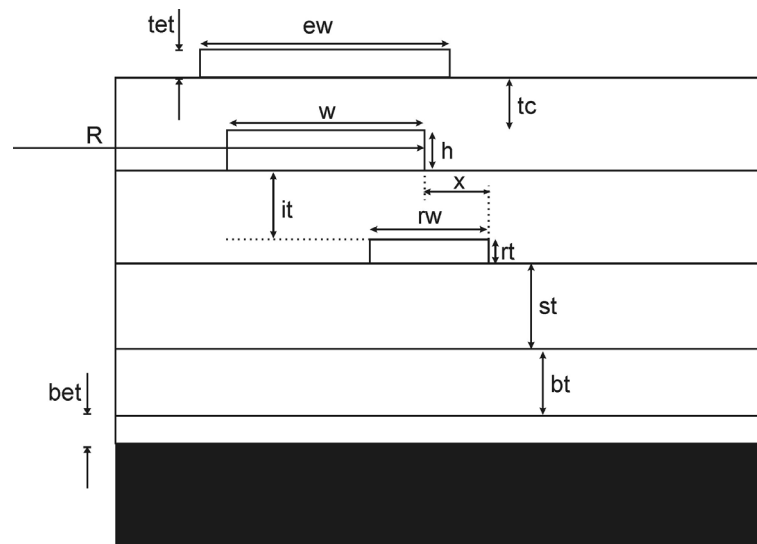


Figure 3.14: Cross section of waveguide and MR with design parameters

3.2.1 Waveguide design

The waveguide consists of an SU8 ridge surrounded by Glassclad. For this waveguide the following parameters have to be determined.

- Slablayer-thickness (st)
- Ridgethickness (rt)
- Ridgewidth (rw)
- Bufferlayer-thickness (bt)

An upper-boundary for the first two parameters combined ($st+rt$) can easily be found by calculating when the SU8 layer becomes multimodal for increasing layerthickness. The layer should be singlemode in order to let the realized device have a predictable behaviour.

To get an estimate for the upper boundary, an effective index simulation of an SU8 layer sandwiched between two Glassclad layers is done [ATR], while varying the thickness of the SU8 layer. By making a graph of these values, the thickness where the first order mode appears can be seen. This is shown in figure 3.15 for both the TE and TM polarization.

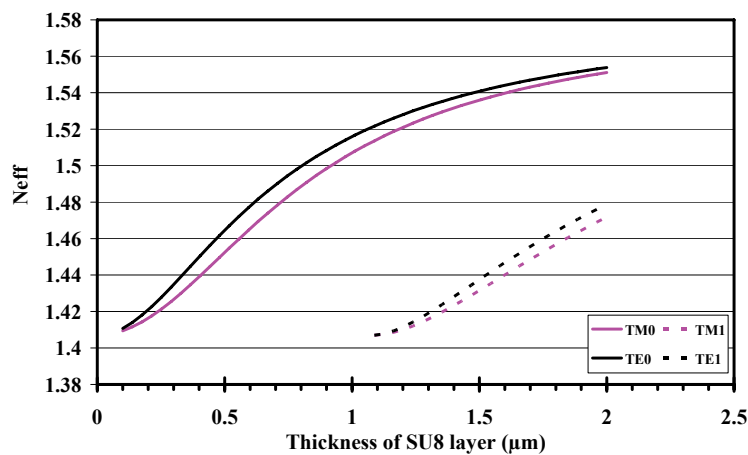


Figure 3.15: Effective index of the modes in an SU8 layer sandwiched between Glassclad for different SU8 layerthicknesses.

From figure 3.15 it can be seen that the layerstack is singlemode up to SU8 layerthicknesses a little over 1 μm . A total SU8 layerthickness of 1 μm is therefore chosen in the design.

➤ $st + rt = 1 \mu\text{m}$

With the thickness $st+rt$ known, a choice has to be made for the ridge-thickness ‘ rt ’. Again a critical demand for this choice is the fact that the waveguide should be singlemode, also in lateral direction. To know in which region the ridge waveguides can be designed, the maximum ridgewidth for singlemode operation, as a function of the ridgethickness, is determined by using the effective index method in 2D [ATR]. The result of this simulation is given in figure 3.16.

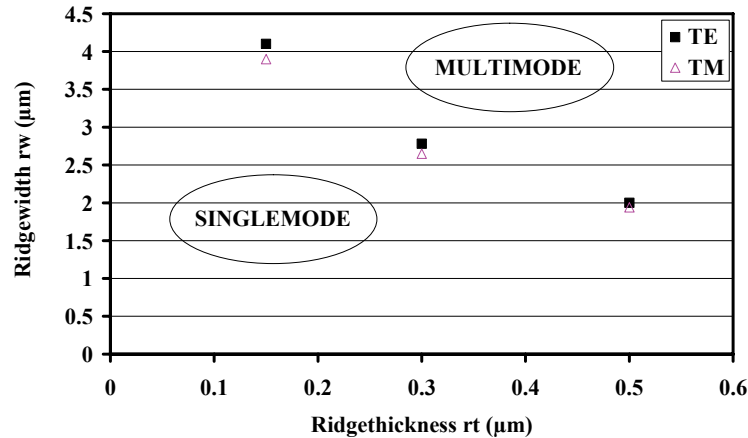


Figure 3.16: Maximum ridgewidth as a function of ridge-thickness for singlemode operation

With the range in which the parameters rw and st can be varied known, the mode profiles and the effective indices for different combinations of rw and st are calculated. This is done in order to design both MR and waveguide with approximately the same effective index (phase matching [Klunder.2002][Geuzebroek.2005]). The simulations were done with the Bend2D solver of TempSelene software [C2V]. The effective index (N_{eff}) of optical modes in different ridge waveguides is given in figure 3.17. For 3 different ridge-thickness (rt), the ridgewidth is varied until the point of bi-modality is reached. The result will be used later for the waveguide phase matching with the MR.

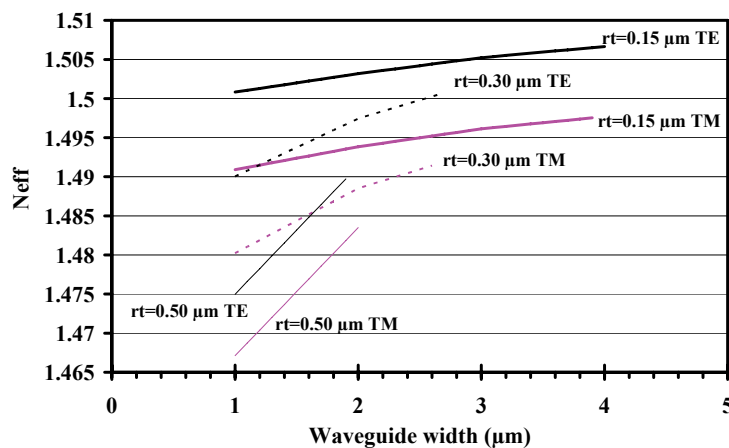


Figure 3.17: Effective index of waveguide modes for different ridge thickness (rt) and ridge width (rw). The ridge width is varied until the waveguide is bi-modal.

➤ $rt = 0.15, 0.30$ and $0.50 \mu\text{m}$

The last parameter to be determined for the complete waveguide design is the bufferlayer-thickness (bt), which should be large enough to let no evanescent tail of the optical mode in the waveguide extends into the bottom electrode. To determine this minimal thickness, a

waveguide (with realistic values of $r_w=2\mu\text{m}$ and $r_t=0.3\mu\text{m}$) is simulated with an electrode (with the same index as the Glassclad, however its imaginary index is 10) under it. By moving the electrode closer to the waveguide a change in imaginary index of the optical mode can be noticed. At the point where this imaginary index changes, the optical mode is sensing the electrode and this is therefore the minimal layer-thickness. This simulation was done in TempSelene [C2V] with the full vectorial complex Bend2D solver. And the result is given in figure 3.18.

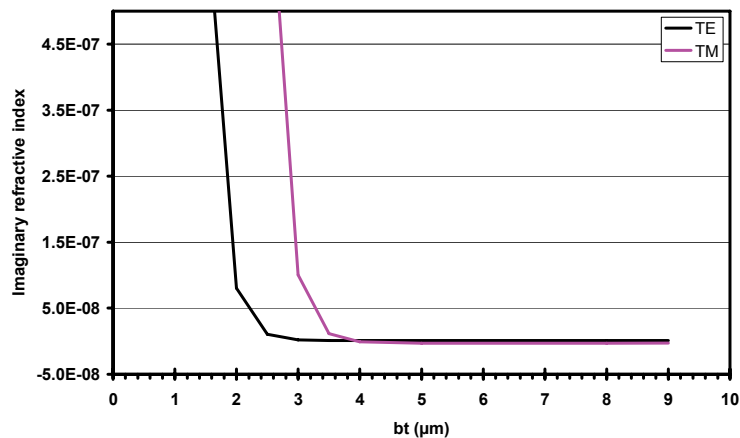


Figure 3.18: Imaginary index of SU8 ridge waveguide as a function of electrode distance.

From figure 3.18 the minimum thickness of the bufferlayer can be found. For the TE polarization this thickness is $3\mu\text{m}$ and for TM $4\mu\text{m}$. The realized thickness should be thicker than this, but should also be as thin as possible to make the electric field between the top and bottom electrode as large as possible, for a given applied voltage.

➤ $bt > 4\mu\text{m}$

3.2.2 Ringresonator design

The ringresonator consists of an etched PMMA-DR1 layer surrounded by Glassclad. The parameters that have to be determined for this MR are:

- MR-height (h)
- MR-width (w)
- MR-radius(R)
- Thickness of the cladding (t_c)

Because during poling of the PMMA-DR1 the dipoles in the material are aligned (chapter 2.2.5), the material has different properties for the TE and TM polarization. This poling induced birefringence can be relatively large [Horowitz.2001] if complete poling is achieved. In a realized device almost always partial poling is achieved and this will give rise to some birefringence, but the exact amount isn't taken into account because the MR is designed such that there is a range of indices for which it should operate properly

To determine the four parameters, it must be determined what the maximum thickness of the MR can be because the MR should be singlemode in vertical direction. A thick MR (large h) has less evanescent field than a thin MR and therefore an index change of the ringmaterial has more effect on the behaviour of the ringresonator in a thicker MR.

To see where the MR becomes multimodal an effective index method simulation is done with ATR guide for a layer of PMMA-DR1 sandwiched between two Glassclad layers. By varying the PMMA-DR1 layerthickness and determining the effective index of the sustained modes, the layer-thickness (h) where the layerstack becomes multimodal was found. The result of this simulation is given in figure 3.19.

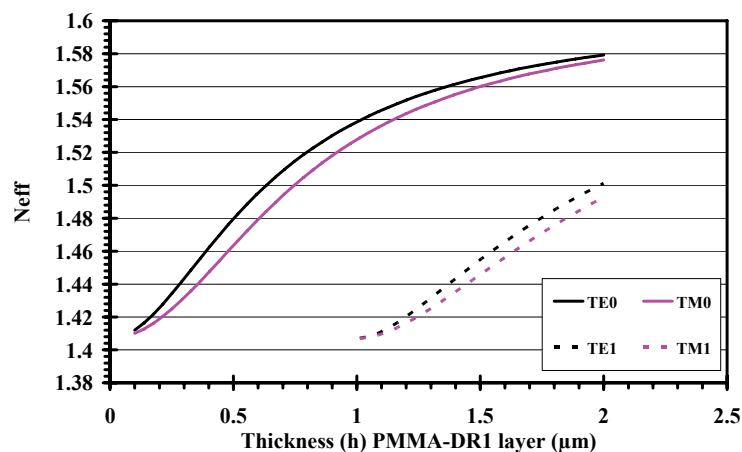


Figure 3.19: N_{eff} for different PMMA-DR1 layerthicknesses

As can be seen from figure 3.19 the layerstack is multimodal when the PMMA-DR1 layer is thicker than 1 μm . A thickness of 0.8 μm is therefore chosen to provide some fabrication tolerance.

➤ $h = 0.8 \mu\text{m}$

With the thickness (h) of the MR known, the width of the MR can be determined. The width of the MR should be large enough to prevent the optical field from sensing the inner boundary of the MR. The theoretical minimum width (w) can be calculated from [Blom.1998]:

$$k_0 w N_{eff} = 3.66 \sqrt[3]{k_0 R N_{eff}} \quad (3-1)$$

in which k_0 is the wavenumber in vacuum, N_{eff} the effective index of the MR and R the radius of the outer edge of the MR. Realistic values for N_{eff} and R are 1.5 and 150 μm respectively. With these values a minimal width of the MR of 5.8 μm is needed.

This can also be simulated by calculating the bendmode of the ringresonator for different ringwidth. As soon as the bendmode starts to “feel” the inner boundary of the MR the effective index of the mode will change. This is simulated in TempSelene [C2V] with the Bend2D solver. Again a realistic MR of 150 μm radius was chosen and the results of this simulation are given in figure 3.20.

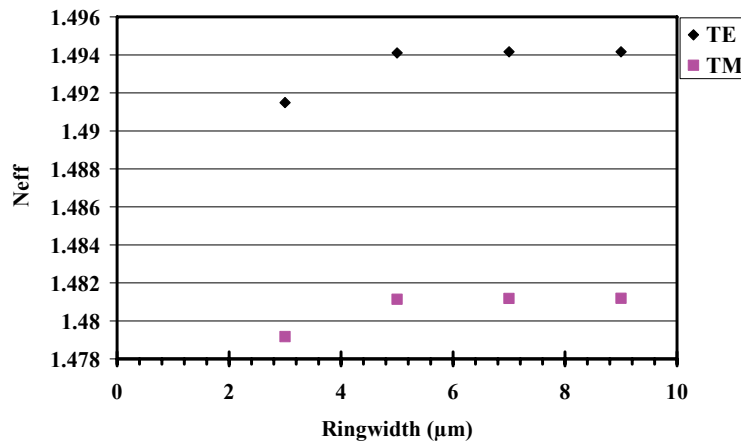


Figure 3.20: Effective index of the bendmode for different ringwidth (w).

As it can be seen in figure 3.20, the index of the bendmode changes when the width of the MR is smaller than 5 μm , which is consistent with the values found from equation (3-1). The minimum ringwidth is therefore 5 μm . To build in a margin for fabrication errors, a width of 7 μm is chosen.

➤ $w = 7 \mu\text{m}$

For the functionality of the MR as a modulator, an important parameter is the finesse, which is determined by the optical loss of the MR and the coupling to the port waveguides.

To determine different ringradii for which the losses due to bending of the waveguide are still acceptable, the loss of the bendmode and its mode profile is calculated for different bendradii. For this calculation a full vectorial Bend2D solver is used. A ringradius is acceptable as long as its bendloss is relatively low compared to the losses caused by fabrication, scattering and absorption. The results of this simulation are given in figure 3.21.

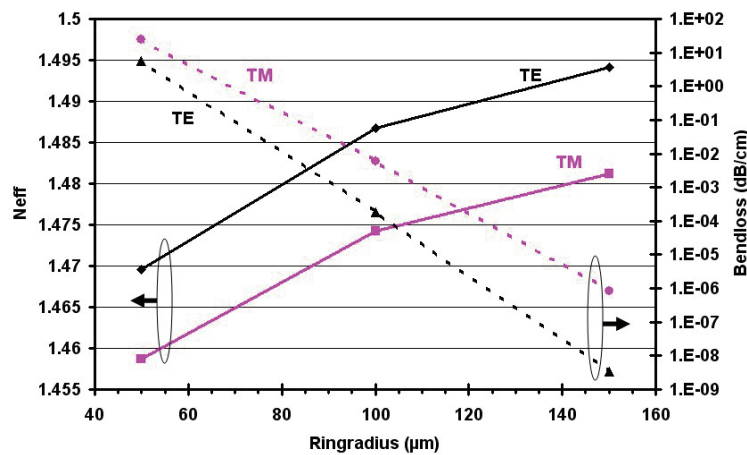


Figure 3.21: Effective index and bendloss as a function of ringradius

It can be noticed from figure 3.21 that the refractive index of the bendmodes is relatively low compared to the index of the PMMA-DR1 (1.606 at 1550 nm). Because the optical mode in a bend-waveguide propagates close to the outer rim of the bend, it will sense the lower index of the cladding relatively strong. For a large EO effect the optical mode should be confined within the active material as much as possible. For an MR with a radius of 150 μm approximately 80% of the light is confined in the PMMA-DR1.

If the maximum allowable bendloss is set to 1 dB/cm (this value is the absorption loss of the PMMA-DR1, derived from a reflow-experiment which will be explained in paragraph 5.1.4), it can be seen from figure 3.21 that the minimum bendradius for the TM polarization is around 70 μm and for the TE polarization around 50 μm. When the ringradius becomes larger, the absorption and scattering losses become more important. To get a realistic idea of the total losses in the MR, the material losses (~ 1 dB/cm at 1550 nm) should be taken into account. With these losses taken into account the total loss per roundtrip is calculated. These losses are given in figure 3.22.

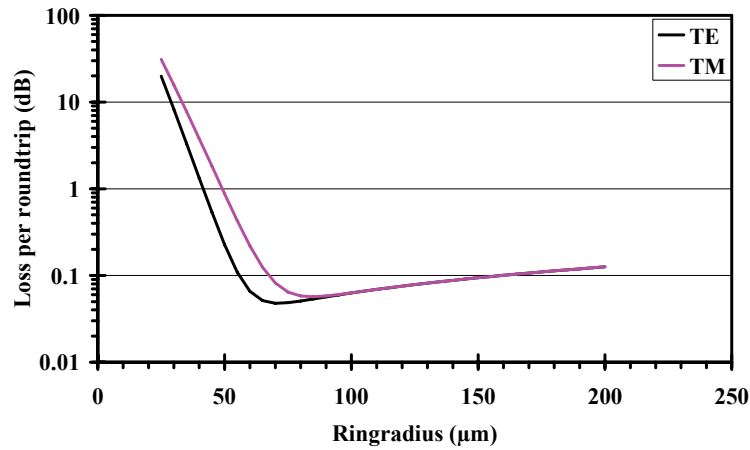


Figure 3.22: Loss per roundtrip vs ringradius

From figure 3.22 it can be seen that the loss per roundtrip shows a range in radii with low loss. In this range the ringradii for the design are chosen.

Ringradii of 50, 100 and 150 μm are chosen.

➤ $R = 50, 100 \text{ and } 150 \mu\text{m}$

In order to couple light from the waveguide to the MR (and back) and bring the MR in resonance it is necessary that the effective indices of the mode in the waveguide and MR are more or less matched [Klunder.2002][Geuzebroek.2005]. To see how close they are to each other, figure 3.17 and figure 3.21 are combined in figure 3.23.

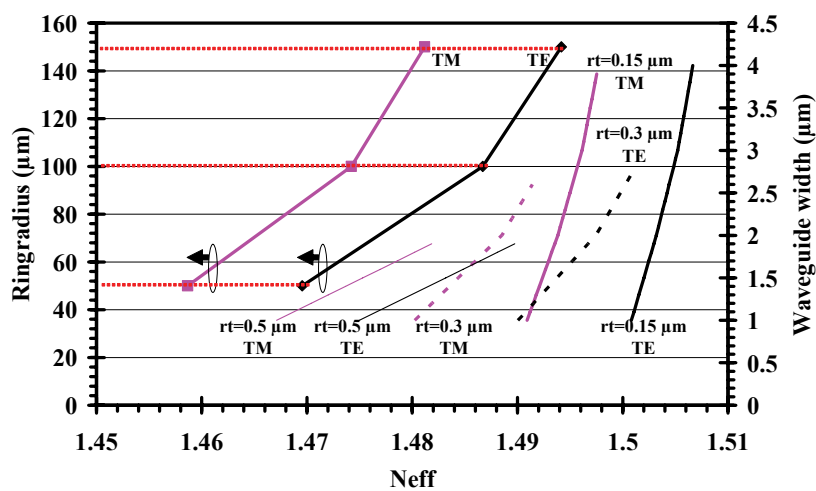


Figure 3.23: Comparison of the effective index of the MR modes with a certain ring radius, and the waveguide modes with a certain width.

From figure 3.23 it is seen that the effective index of the MR is in most cases lower than the index of the waveguides. For TE polarization phase matching is possible for ringradii from 50 to 150 μm and for the TM polarization this can be reached with “larger” rings only.

When poling PMMA-DR1, the layer will become birefringent and the refractive index of the TE mode is lowered. For the TM mode the refractive index increases. This makes phase matching possible for the TM polarization of a poled MR. The effective indices as given in figure 3.23 make it possible to measure and characterize the spectra of phase-matched MRs both for the poled (TM measurements) and unpoled (TE measurements) situation.

In order to build in a tolerance for fabrication errors in the ridge-thickness (rt), a value of $rt=0.3\mu\text{m}$ is chosen in the realized device.

$$\triangleright rt = 0.3 \mu\text{m}$$

The last parameter of the MR to be determined is the thickness of the cladding layer (tc). This thickness is determined in the same way as the thickness of the bufferlayer (see page 50).

Again the electrode is represented as a material with the same index as the Glassclad layer, however its imaginary index is 10. The cladding should be thick enough to prevent the evanescent tail of the mode in the MR from sensing the presence of the topelectrode. By calculating the imaginary part of the index of the bendmode for different values of tc , the minimum thickness can be determined. This is done for the bendmode with the largest evanescent tail, which is the one with the lowest effective refractive index and therefore it is calculated for an MR with a radius of 50 μm . The result of this simulation is given in figure 3.24.

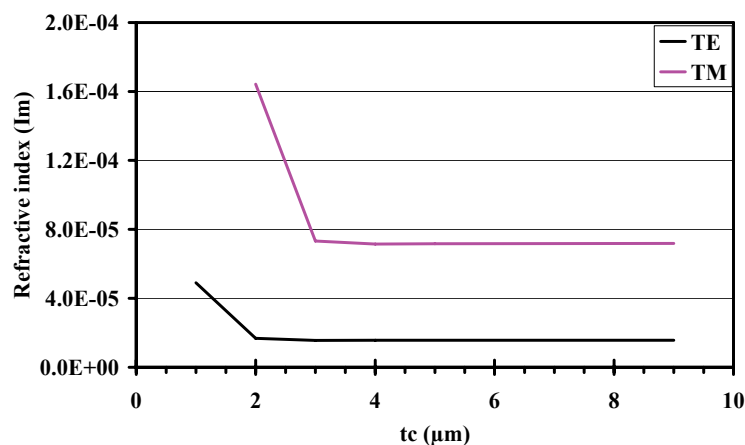


Figure 3.24: Imaginary part of the refractive index of the bendmode for a radius of 50 μm .

As can be seen in figure 3.24, the influence of the electrode becomes noticeable when the distance between MR and electrode is smaller than 3 μm . To build in a safety margin, a minimum distance of 4 μm is chosen in the design.

➤ $tc > 4 \mu\text{m}$

In the analysis of the behaviour of the MR, as given in chapter 2, the dispersion should be taken into account because the group index is used in these models instead of the effective index. In order to see the amount of dispersion, the effective index of the bendmode is determined as a function of wavelength by simulating the bendmode for different wavelengths. In the simulation the material dispersions derived from the Cauchy parameters (shown in figure 3.4 and figure 3.13) are taken into account.

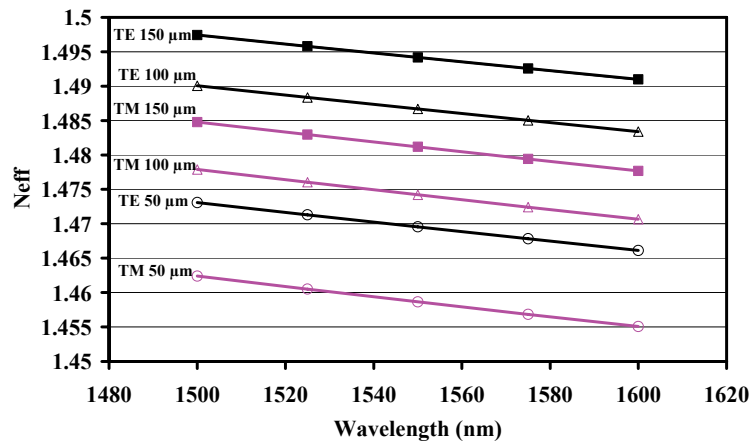


Figure 3.25: Effective index of the MR as a function of wavelength for different ringradii

From the slope of the lines in figure 3.25, the dispersion ($dn_e/d\lambda$ from equation (2-19)) can be calculated and a value of $-9 \cdot 10^{-5} \text{ nm}^{-1}$ is found. This value makes the group index approximately 0.14 higher than the effective index.

3.2.3 Total device

A range of device parameters is determined in the simulations and a choice can be made for the final device parameters. Table 3.3 summarizes the chosen parameters with some remarks.

Parameter	Chosen value	Comment
st	0.7 μm	st + rt < 1.05 μm , otherwise the waveguide becomes multimodal
rt	0.3 μm	
rw	2 μm	with st and rt as given above, rw should be < 2.6 to keep the waveguide singlemode
bt	4 μm	$\geq 3 \mu\text{m}$ for TE and $\geq 4 \mu\text{m}$ for TM
h	0.8 μm	Should be < 1 μm
w	7 μm	should be > than 4 μm
R	Various (50 - 100 – 150 μm)	
tc	4 μm	> 3 μm
bet	150 nm	should be conductive, therefore > 50 nm
ew	13 μm	Chosen 3 μm wider (at all sides) than the MR (will be explained in the next paragraph
tet	150 nm	should be conductive, therefore > 50 nm

Table 3.3: Summary of the designed parameters

After the determination of different parameters of the waveguide and MR, the last parameters of the total device can be simulated. These parameters determine the positioning of the MR with respect to the waveguide. They are (see also figure 3.26):

- Thickness of the intermediate layer (it)
- Horizontal offset of the MR (x)

These two parameters control the behaviour of the complete device. The combination of “it” and “x” determines the coupling constants (κ_1 and κ_2) and therefore the shape of the through- and drop-port amplitude spectrum and phase spectrum.

To determine realistic design values for “it” and “x” the amount of coupling is calculated/determined. This can be done by coupled mode theory [Okamoto.2000], but it can also be simulated by a 3D BPM, which simulates more realistic the amount of coupling from the waveguide to the MR.

With the software Olympios [C2V], a series of 3D BPM simulation were done for different values of the design parameters from table 3.3. In these simulations the coupling from waveguide to MR is calculated as a function of both “it” and “x”. The results of these simulations are given in figure 3.27. The positive x direction is from the edge of the MR to the centre of it (figure 3.26).

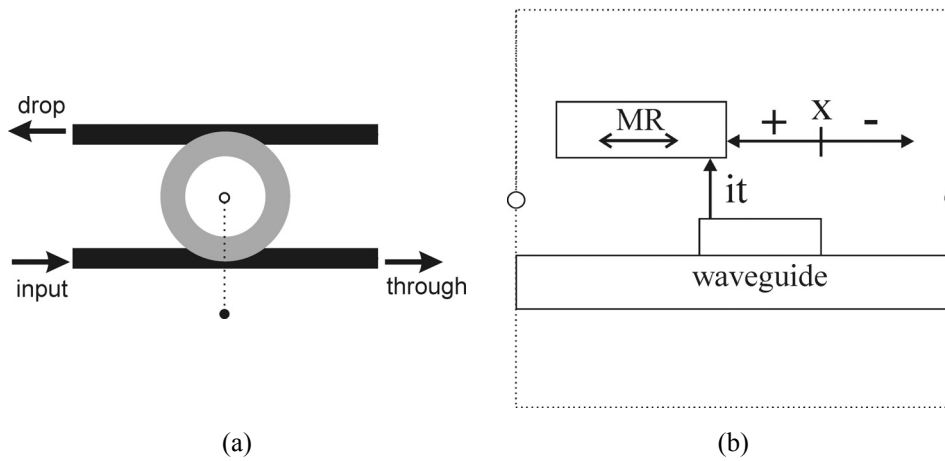


Figure 3.26: Topview (a) and cross-section (b) to define positive shift direction of MR (x)

From the data in figure 3.27 a choice can be made for “it” and “x”. “x” can be varied over the optical mask by varying the position of the waveguides relative to the MR. “it” can only be varied by changing the layer thickness and is therefore chosen such that a large range of coupling constants can be obtained by varying “x”. A value of “it” of either 600 or 700 nm is chosen because the coupling constant can be varied on a single wafer from approximately 0.2 to 0.95 by varying “x” from $-2 \mu\text{m}$ to $2 \mu\text{m}$.

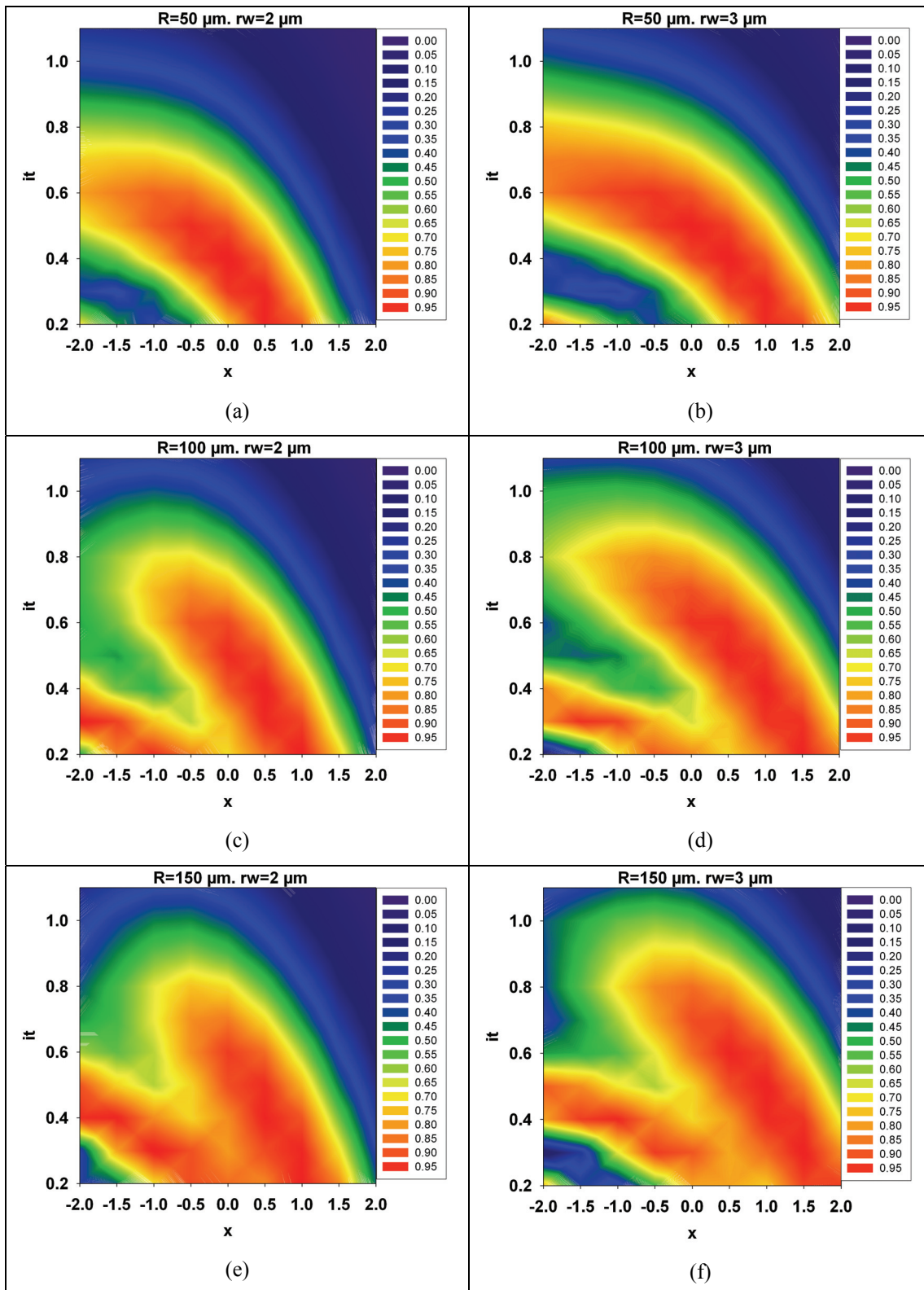


Figure 3.27: Power coupling constant from waveguide to MR for different ringradii and waveguide width (a) $R = 50 \mu\text{m}$ and $rw = 2 \mu\text{m}$ (b) $R=50 \mu\text{m}$ and $rw = 3 \mu\text{m}$ (c) $R = 100 \mu\text{m}$ and $rw = 2 \mu\text{m}$ (d) $R = 100 \mu\text{m}$ and $rw = 3 \mu\text{m}$ (e) $R = 150 \mu\text{m}$ and $rw = 2 \mu\text{m}$ (f) $R = 150 \mu\text{m}$ and $rw = 3 \mu\text{m}$

3.2.4 Electrode design

The electrode structure needed to apply an electrical field over the MR has to be designed, such that the device can function up to frequencies of 1 GHz.

For high speed operation the electrode structure can be represented by the scheme in figure 3.28.

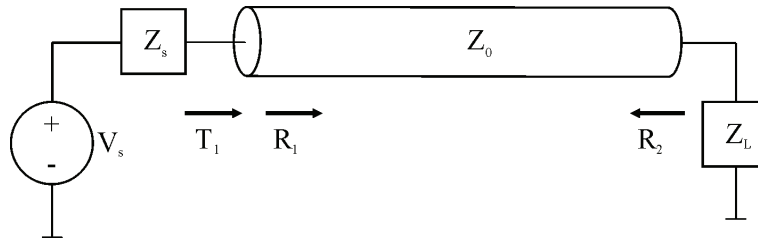


Figure 3.28: Electrical representation of the topelectrode

In figure 3.28 the topelectrode (with characteristic impedance Z_0) is driven by a voltage modulator supplying a voltage V_s and having an impedance Z_s . The end of the topelectrode is coupled to ground with a load resistance (Z_L). The ‘T’ and ‘R’ parameters in figure 3.28 are the transmission and reflection parameters at that point in the scheme.

To prevent reflection back into the electrode R_1 should be zero. Mathematically R_1 is given by:

$$R_1 = \frac{Z_s(\omega) - Z_0(\omega)}{Z_s(\omega) + Z_0(\omega)} \quad (3-2)$$

It can be seen that the characteristic impedance of the electrode should be matched to that of the source (50Ω). Matching the characteristic impedance of the electrode to the source causes a reduction of the transmission from the source to the electrode to 0.5. This factor T_1 is given by:

$$T_1 = \frac{Z_0(\omega)}{Z_s(\omega) + Z_0(\omega)} \quad (3-3)$$

This factor 0.5 can be compensated for by using the electrode as a lumped element. As a rule of thumb in RF design it is stated that if no feature of the electrode structure is longer than 10% of the electrical wavelength, the electrode can be used as a lumped element. For a frequency of 1 GHz in a material with a relative dielectric constant of 3 (~ for polymers) this

means that the maximum electrode length is 2 cm. When using the electrode as a lumped element the resistance Z_L in figure 3.28 is ∞ , resulting in a factor R_2 of 1.

$$R_2 = \frac{Z_L(\omega) - Z_0(\omega)}{Z_L(\omega) + Z_0(\omega)} \quad (3-4)$$

This total reflection at the end of the electrode will double the voltage (compensating for the factor 0.5) on the electrode because the reflected wave is added to the incoming (which is equal to the applied voltage times T_1). A lumped element electrode will therefore be applied on the device in order to have a large electric field over the MR.

In order to build in some fabrication tolerance for misalignment of the electrode structures, the electrode is 3 μm wider (on both sides) than the MR.

In order to be able to connect multiple MR-resonators at the same time a wide contact lead is deposited that connects the different top-electrodes (see figure 3.29).

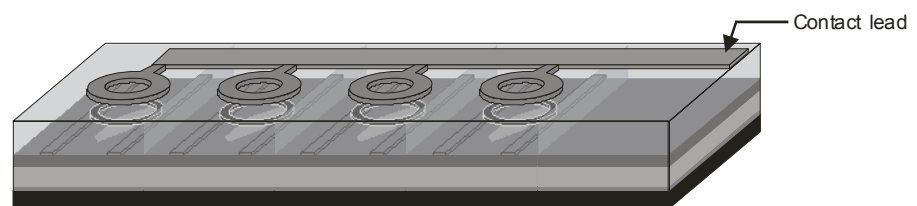


Figure 3.29: Contact lead to connect multiple devices

This contact lead largely determines the characteristic impedance of the electrode structure and the complete electrode structure is therefore considered as a single micro-stripline.

In [Johnson.1993] the formulas for the impedance of a micro-stripline can be found. When calculating the characteristic impedance as a function of the width of the micro-stripline (with a thickness of 200 nm) a graph as in figure 3.30 can be made.

From figure 3.30 it can be seen that an impedance of 50 Ω can be reached by making the stripline approximately 25 μm wide. An important frequency restriction, i.e. the RC time of the total electrode structure can easily be calculated if the area of the contact lead is known. For the fabricated device the calculated capacitance between top and bottom electrode is 5.5 pF. Resulting in a maximum allowable contact resistance of approximately 150 Ω to keep the RC time below 1 ns, making frequencies of 1GHz possible.

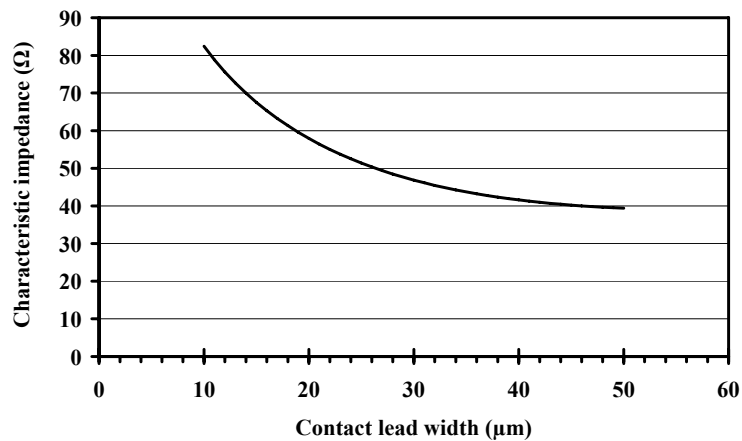


Figure 3.30: Characteristic impedance as a function of strip-width

3.3 Mask Design

After simulating the entire device, a series of masks for optical lithography is made. On these masks structures for both the MR and the MZI devices are realized. This paragraph will discuss the different masks needed (the complete specifications of all the mask parameters are given in appendix A1).

The entire device needs 4 mask layers, which are required for:

1. Defining the part of the slab under the MR that should be removed
2. Defining the ridge waveguides for the single MR and MR-MZI devices
3. Defining the MR
4. Defining the top electrodes.

For each mask the different choices that are made will be discussed.

Mask1:

This mask is used to define areas in the slab SU8 layer that must be removed in order to prevent light from coupling from the MR into the slab.

The slab should be removed completely below the MR. Because the ridge waveguide is also below the MR, it cannot be removed completely. A shape as given in figure 3.31 is chosen with a distance d_s between the part removed and the ridge waveguide.

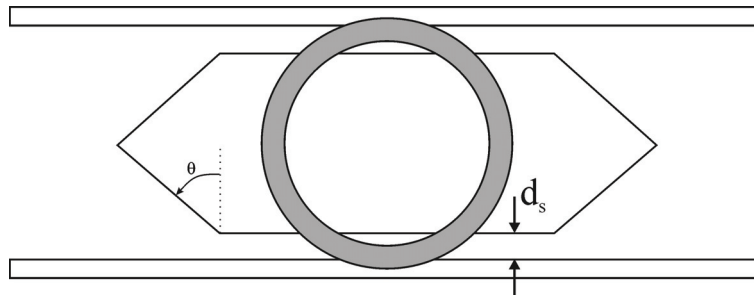


Figure 3.31: Shape of the slab removed and distance between ridge and removed slab

The distance d_s should be large enough so that the optical mode in the ridge waveguide will not sense the part of the slab removed. To see how large d_s must be, a 2D effective index method simulation is done [ATR] for a ridge waveguide with $rw=2\mu\text{m}$ and $rt=0.15\mu\text{m}$ ($0.15\mu\text{m}$ is chosen because this is one of the smallest ridges, with the largest field in lateral direction, within fabrication tolerances around $rt=0.3\mu\text{m}$).

To see the influence of a disturbance on the mode in the ridge waveguide an additional layer with a small imaginary index is added to the simulated structure and the influence of this layer can be seen in the effective index of the mode if d_s decreases. Schematically this simulation is shown in figure 3.32.

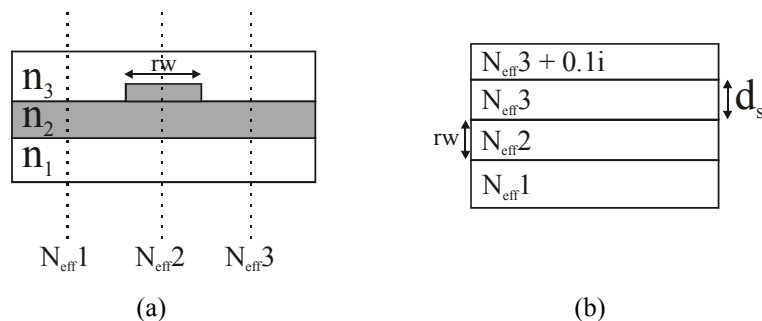


Figure 3.32: Representation of the 2D ATR simulation steps (a) first step (b) second step

From the simulation data, a graph of the effective index vs. d_s is made (figure 3.33)

From this graph it can be seen that a minimal distance of $\sim 5\mu\text{m}$ should be taken into account for d_s . To build in a margin for fabrication errors a distance d_s of $12.5\mu\text{m}$ is chosen. The angle (θ), in figure 3.31, is chosen 45° (this is not considered a critical angle).

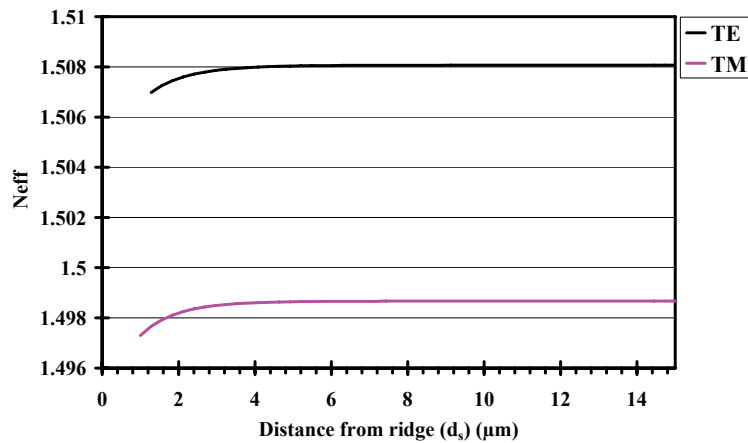


Figure 3.33: Neff of mode vs. d_s

Mask2:

For the characterization of the MR it is important that the through and drop port can both be measured when light is coupled in at the input port. Because the characterization will be done with a fiber coupling setup (paragraph 5.2), in which light is coupled in and out with an optical fiber, it is convenient that the in- and out-coupling are done on two different sides of the device. Therefore the drop waveguide is bend back, so it is coupled out at the same side of the sample as the through port (see figure 3.34).

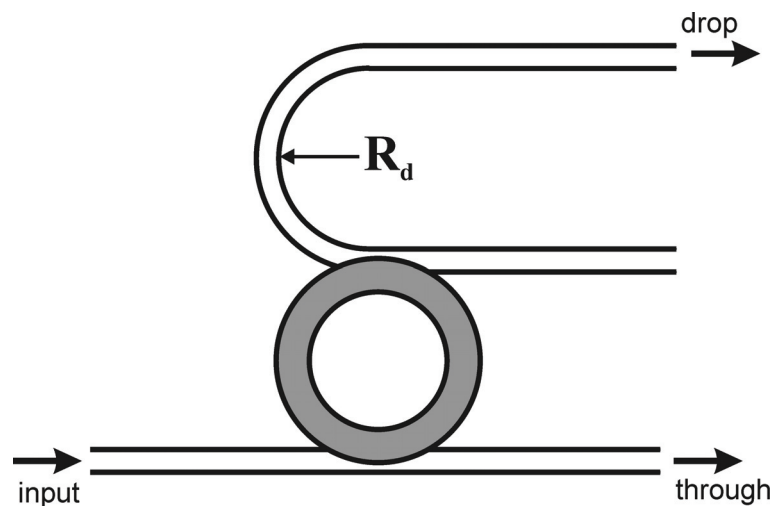


Figure 3.34: Return waveguide in drop port

To keep the device as small as possible the bend-radius (R_d) should be as small as possible. In order to know the minimal bend radius, a 2D-bend mode simulation is done in Tempsele [C2V] in which the bendloss of a $2 \mu\text{m}$ wide ridge (with $r_t = 300 \text{ nm}$) was calculated. The result of this simulation is given in figure 3.35. It was found that, if a minimal loss figure for this bend is set to 1 dB/cm , the bend-radius must be larger than $1000 \mu\text{m}$.

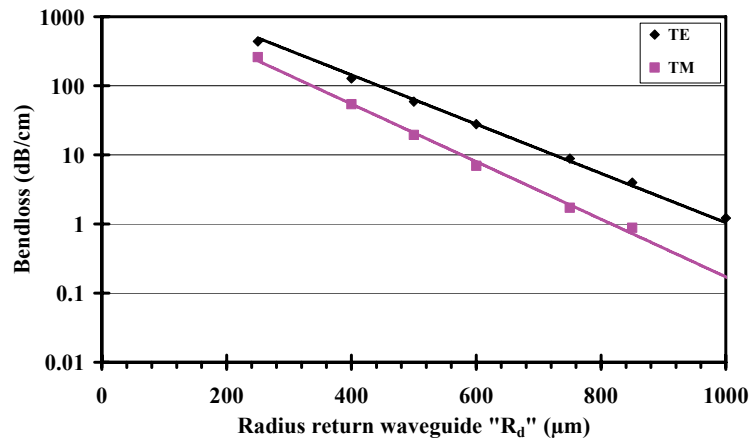


Figure 3.35: Bendloss of return waveguide vs. radius

In order to prevent the bend-loss to have a large influence a larger bend-radius of $2750 \mu\text{m}$ is chosen.

For the MZI an additional splitter and combiner must be designed in the ridge waveguide. Because the design specifications for this splitter and combiner aren't very stringent (a 3 dB splitter and combiner are needed), a simple y junction can be used for this. The y junction can be constructed from 2 S-bends with a certain radius. In figure 3.35 it was already shown that a bend-radius larger than $1000 \mu\text{m}$ in the ridge-waveguide has an acceptable loss. The radius of the S-bend is chosen much larger ($5000 \mu\text{m}$) and should therefore not cause any additional loss. The distance between the two branches of the MZI is chosen to be $150 \mu\text{m}$.

Mask 3:

This mask is the most critical one in the fabrication process. The alignment of this mask to the waveguide layer determines the distance (x) between the MR and the waveguides and therefore also the coupling constants. In order to have variation in the coupling constants over the mask, several positions of the MR (different values for x) are chosen on the mask.

The dimensions of the MR were chosen previous in this chapter

- Radii of 50 , 100 and $150 \mu\text{m}$
- MR width (w) is chosen to be 5 , 7 and R (the MR becomes a disc)
 - o This is done in order to have variation in the influence of the inner rim of the MR.

Mask 4:

This mask is used to pattern the topelectrode. The electrode should be concentrated above the MR in order not to be sensitive for defects in the layers over the entire wafer. In order to prevent sensitivity for misalignment, the electrode is designed to be 3 μ m wider than the MR on all sides (inner and outer rim).

As was discussed in chapter 3.2.4, the electrodes above the MR are connected via a large contact lead.

4 Realization

This chapter will discuss the realization of the MR and the MZI with MR in the MESA⁺ cleanroom. First the different steps in the fabrication process will be discussed, after which the problems and challenges of the different fabrication steps will be treated in some more detail.

4.1 Fabrication steps

The different fabrication steps will be discussed for the MR in the following pages. The steps for the MZI devices are the same (the devices are on the same wafer). A detailed description of the entire process (with all the process parameters) is given in appendix A2.

The basic device as realized is given schematically in figure 4.1. The cross-section in table 4.1 is along the dotted area in figure 4.1.

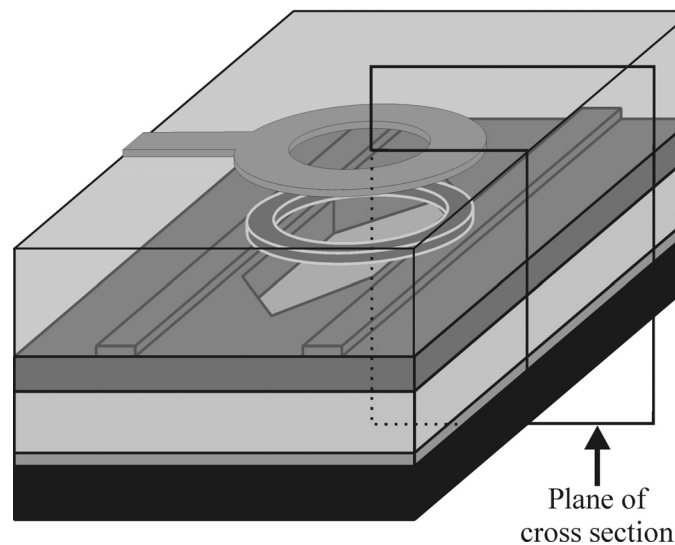











Figure 4.1: 3D schematic picture of the realized device

The start of the realization is the cleaning of a silicon wafer.	
On this wafer, a layer of gold of 150 nm thick is deposited by evaporation (a thin layer of 5 nm chromium is used as sticking layer under the gold). On the 150 nm gold another 5 nm of chromium is deposited to improve the adhesion of the next layer.	

REALIZATION

<p>The bufferlayer of minimal 4 μm of Glassclad is spincoated on the bottom electrode and thermally cured.</p>	
<p>The first layer SU8 with a thickness of 0.7 μm is spincoated on the Glassclad and thermally cured.</p>	
<p>With a lithographic process a part of this layer is removed. This is done to prevent coupling from the MR to the SU8 slablayer under the MR.</p>	
<p>A second thin layer (0.3 μm) SU8 is spincoated and thermally cured.</p>	
<p>A ridge waveguide is lithographically defined.</p>	
<p>The intermediate layer of Glassclad is spincoated and thermally cured.</p>	
<p>A layer of PMMA-DR1 is spincoated and thermally cured.</p>	

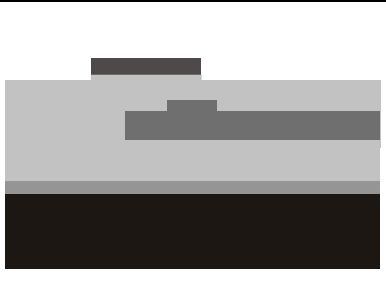
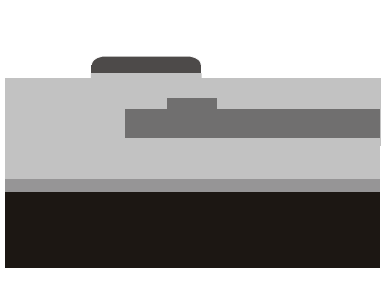
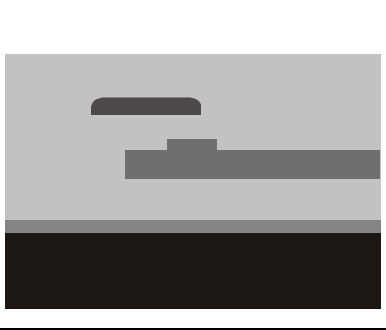


<p>Lithography followed by reactive ion etching defines the MR.</p>	
<p>By heating the MR above its T_g, the MR is reflowed to smoothen the surface roughness [Leinse.2004]</p>	
<p>The topcladding of Glassclad is applied by spincoating and thermally curing.</p>	
<p>A topelectrode of 150 nm gold (with 5 nm chromium as a sticking layer) is applied by sputtering.</p>	
<p>The top electrode is patterned by lithography and wet etching of the gold and chromium.</p>	

Table 4.1: Different steps in the fabrication process.

4.2 Fabrication issues

This paragraph will discuss some specific issues in the fabrication process as encountered and solved during the fabrication. The different issues are discussed chronologically in the fabrication process.

4.2.1 Buffer layer spincoating

Because the waveguide is placed on top of an electrode, the bufferlayer should have a minimal thickness of $4\ \mu\text{m}$ (see paragraph 3.2.1). When stacking multiple layers of Glassclad, the shear stress at the interfaces between these layers can result in cracking [Wicks.1998]. In practice it is possible to stack a maximum of three layers Glassclad on top of each other without cracking. It is therefore preferred to spin the Glassclad in as little layers as possible. To make layers as thick as possible, the spinspeed should be low. When spincoated at low speeds, the uniformity in thickness becomes less. To make uniformity better, the layer is spincoated in an enclosure which is saturated with the solvent of Glassclad (isopropanol). This saturation prevents the solvent from evaporating too fast during the spinning process, which otherwise would result in a typical star-shaped pattern on the wafer. Figure 4.2 shows a part of this pattern on a device-wafer. The pattern is seen as the lines going from lower left to upper right. It can be seen that the origin of the pattern is in the centre of the wafer. This wafer was spincoated without the saturated enclosure.

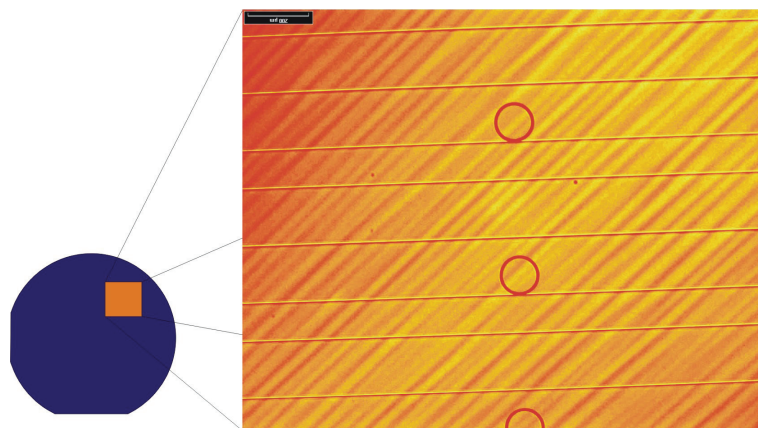


Figure 4.2: Spin pattern in Glassclad layer on a device wafer with schematically its position on the wafer: the rings shown have a diameter of $300\ \mu\text{m}$

These lines are layer thickness variations (with an amplitude of approximately $100\ \text{nm}$) of the Glassclad layer. These variations do not necessarily have to cause problems because they are gradual and should not cause scattering or optical loss. Preventing them makes it easier to

predict how the coupling between the MR and the waveguide will behave. A flat Glassclad layer is therefore preferred.

4.2.2 SU8 lithography

A description of the material SU8 is already given in chapter 3.1.1 and in this paragraph the lithographic process will be discussed further.

Because of the high optical transparency of the material for wavelengths above 360 nm, the material is well suited for imaging near vertical sidewalls in (even very thick) resistlayers.

The “standard” lithographic process for SU8 has the following general steps:

- Spincoating of the material
- Softbake (to remove the solvent)
- UV exposure (to generate the acid, which is a catalyst for the cross-linking)
- Post exposure bake (to crosslink the material)
- Develop (to remove the non-crosslinked material)
- Rinse and dry (to stop the developing process)
- Hard bake (to further crosslink the material and increase its T_g)

Depending on the type of SU8 (solvent content, layerthickness etc.) there are different parameters for each step.

The two most critical steps in the process are the UV exposure and the post exposure bake. These steps should be matched to each other. For a certain amount of generated acid, a suitable baking temperature/time should be found. When for instance the exposure time is too short for a certain baking step, the material doesn't cross-link and is flushed away during development. If on the other hand the exposure time is too long for a certain post exposure bake (or the post exposure bake is too long or too high in temperature for a certain exposure time), too much material cross-links and it is very difficult to remove the un-exposed material in the developing step. The first point where this effect occurs is at the edges of the defined waveguide. At these edges diffusion of the generated acid into the surrounding occurs and the material cross-links where the acid has diffused to. Figure 4.3 is an example of the result of such acid diffusion. In this figure a trench in SU8 can be seen in which the acid has diffused from the sidewalls to the middle of it.

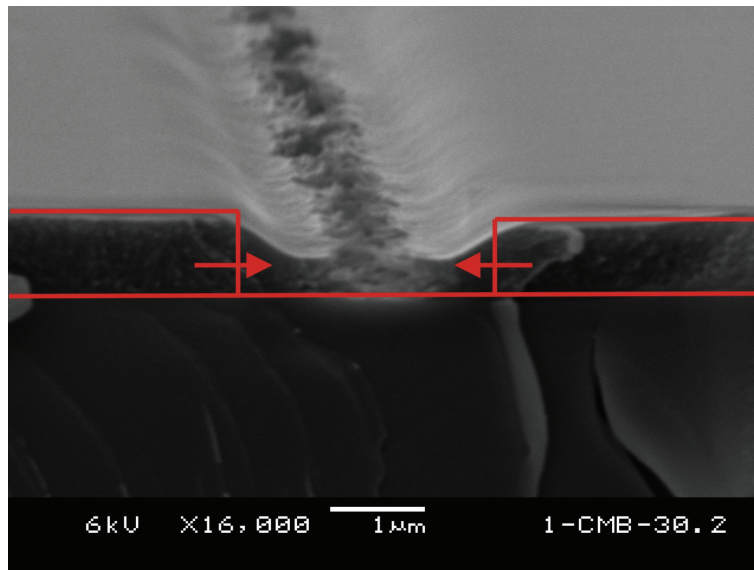


Figure 4.3: Trench in SU8 with diffusion of the acid towards the middle of the trench. The drawn lines give the original trench definition.

Another important issue with SU8 is the fact that the surface on which it is applied must be “free” of water to make the wetting uniform. This water-free surface can be achieved by baking the sample before applying the material. At temperatures of 120°C the water is removed in approximately 15 minutes. If the sample is not treated before spincoating, layers as shown in figure 4.4 can be formed.

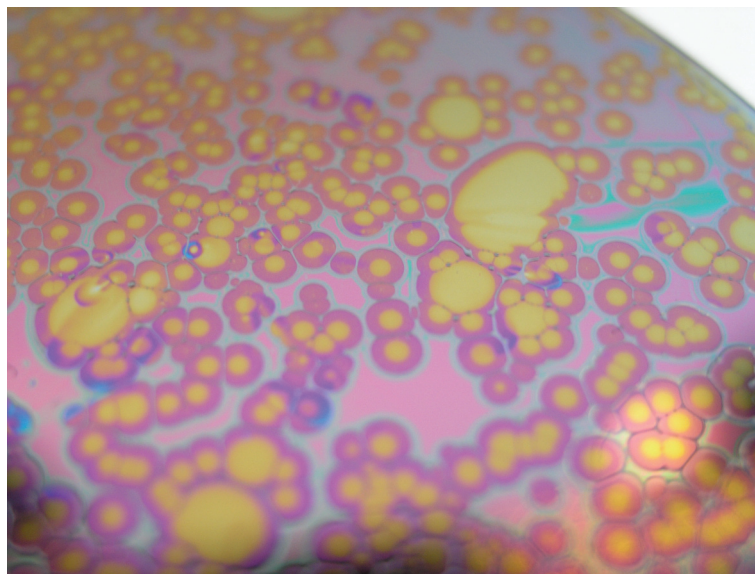


Figure 4.4: Part (1/4) of a (10 inch) wafer with an SU8 layer with poor wetting

It can be seen that the wetting is poor and that the surface tension of the SU8 forms islands all over the wafer.

Another effect occurring with water in a layer below the SU8 layer is the inhibition of the cross-linking which is caused by the presence of the water [Asperen.2003]. In order to fabricate reproducible structures (with reproducible dimensions) the presence of water should be minimum. A relative humidity between 40-46% is recommended [MRT.SU8]

4.2.3 Intermediate layer

After the SU8 ridge is defined, an intermediate layer between the waveguide and the MR is applied. The thickness of this layer determines largely the amount of coupling of light between the waveguide and the MR. It is therefore very important to control this thickness accurately. Because of the hydrophilic character of Glassclad it responds strongly to the properties of the surface on which it is spincoated. Mostly when spincoating layers of polymer over a ridge, a height difference in the layer occurs. Schematically this is shown in figure 4.5.



Figure 4.5: Schematic representation of layer variations around a ridge waveguide

To test how Glassclad behaves around an SU8 waveguide a relatively thick (approx 2 μm) SU8 waveguide is fabricated. This waveguide is made thicker than the ridge in the realized device, because it is the expectation that planarization is more difficult when the ridge becomes thicker. When Glassclad is spincoated on an SU8 ridge and baked on a hotplate of 150°C for 2 hours, the SEM picture of the cross-section of a waveguide looks as shown in figure 4.6.

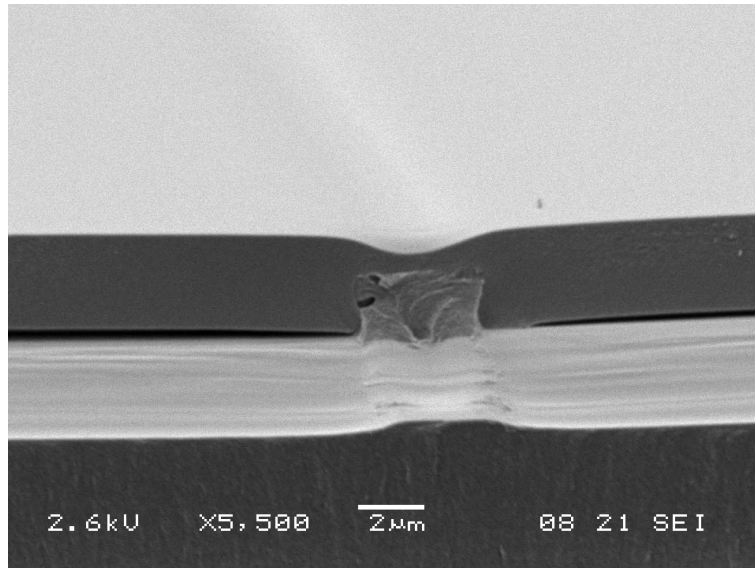


Figure 4.6: SEM picture of a Glassclad layer on an SU8 waveguide

It can be seen that the shape of the surface of the Glassclad is exactly opposite to what is expected. This is probably caused by a local difference in surface tension. As a result of the Marangoni effect, the low surface tension part of the film flows away from the waveguide trying to cover the surroundings higher surface tension (of the liquid Glassclad) [Wicks.1998]. This flow is schematically shown in figure 4.7.

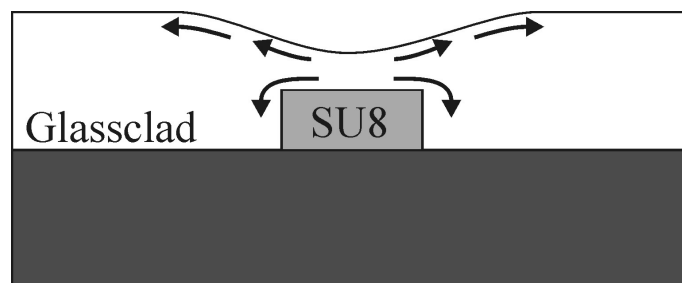


Figure 4.7: Schematic representation of the flow from the low surface tension SU8 waveguide

From figure 4.6 it can be seen that the rest of the top surface of the Glassclad is smooth and planarized with exception of the region above the waveguide.

Because this effect will be smaller when the ridge becomes lower this will probably not cause problems in the realized device. Would it be a problem, a solution could be to apply another layer of Glassclad which planarizes better and etch back the Glassclad layer to the desired thickness [Mulder.2004].

4.2.4 Surface modifications

Glassclad reacts with glass and siliceous surfaces to form a covalent bond. It has excellent abrasion resistant properties and can be applied to materials as a protective coating. The material has silica with CH₄ groups on the interface of an applied layer. With the organic (CH₄) part at the surface, the wetting on and sticking to this layer are poor because the surface energy of the layer is too low. Modification is needed to raise the surface energy.

There are different techniques for modifying polymeric surfaces. These different techniques are discussed in [Mittal.1996] and are based on oxidizing the surface of the polymer, which leads to elevated surface energy levels and to increased adhesion. A few examples of different techniques (with their drawbacks) are [Mittal.1996]:

- Corona-discharge treatment
 - o Is easy to use for high speed inline applications, but is difficult to use on three dimensional objects.
- Plasma treatment
 - o The biggest drawback of this technique is the need for a high vacuum environment and therefore high capital cost.
- Flame treatment
 - o Is relatively low cost, but not very suitable for thermally sensitive materials.

Another technique (used in the fabrication process of the MR) is using ozone generating UV light to modify the polymer surface. The most important drawback of this technique is the fact that it takes relatively long time to treat a surface. [Peeling.1983] states that "...the time scale for ozonation and photo-oxidation to produce fully oxidized surfaces is in the order of several hours". A benefit of this is that the process is easier to control.

In a UV-ozone reactor a mercury lamp is used that emits two main wavelengths of interest. (184.9 nm and 253.7 nm). The 184.9 nm wavelength causes the ozone to be formed from oxygen present in the reactor. This ozone will absorb the higher UV wavelength of 253.7 nm, resulting in a photodecomposition of which one of the products is molecular oxygen.

This molecular oxygen can initiate the oxidation reaction with the methyl groups of the Glassclad and therefore change the surface (to silica) such that the adhesion of materials on top of this layer improves.

4.2.5 PMMA-DR1 etching

The EO MR is created from the polymer PMMA-DR1 in a solution consisting of 9 mass-percent of PMMA-DR1 in 1,1,2 trichlorethane (TCE). Using this, a layer of approximately $0.8\ \mu\text{m}$ can be spincoated (see also spincurve page 46).

This layer is etched by a Reactive Ion Etch (RIE) process. In this process a mixture of O_2 and SF_6 gas is used. The O_2 is used to etch the PMMA-DR1 and the SF_6 to etch the Glassclad underneath (the next paragraph will discuss the need to etch part of the Glassclad). A problem that arises with this etchprocess is the removal of the resist after etching. Because PMMA-DR1 is a non-crosslinked polymer (not very resistant to different solvents), it is practically impossible to remove a resistlayer after the RIE process without partially dissolving the PMMA-DR1. To have an MR without resist after etching, the thickness of the resist must be controlled such that the resist is able to sustain the etchplasma slightly longer than the PMMA-DR1. The resist can be etched away completely in the RIE. Figure 4.8 shows 4 different stages in the etching process schematically.

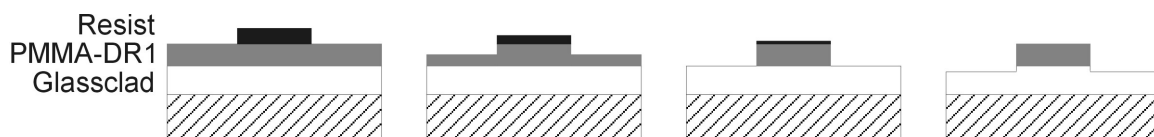


Figure 4.8: Four steps in the Reactive Ion Etching process of PMMA-DR1

During etching, the edges of the resist-profile round off because the resist etches faster at the edges of the MR. Etching all the resist from the MR implies that the edges of the MR are also rounded off and that the perfectly square MR-definition is distorted. This should not cause a problem because the induced change by the distortion in the effective index of the optical MR mode is small compared to the index change caused by the poling fabrication step (chapter 4.2.11).

The cross section of the MR is further changing during reflowing which will be discussed in the next paragraph.

4.2.6 PMMA-DR1 reflowing

After etching, the MR has a relatively high roughness. The sidewalls are always rough in a RIE-ed sample, but because the resist is etched away completely, also the top surface of the MR has become rough. This roughness can be reduced by a technique called reflowing. Because the etchdepth of the RIE was a bit larger than the thickness of the MR (also part of

the Glassclad layer was etched away), the MR is placed on a ridge. Figure 4.9.a shows a SEM photo of such an MR in a DANS (4-dimethylamino-4'-nitrostilbene) [Diemeer.1998] containing EO side chain polymer, that was processed in the same way as the PMMA-DR1 MR. For this MR it can clearly be seen that it is placed on a ridge. If the MR is heated slightly above the T_g of the ringmaterial, the surface tension in the softened polymer smoothens the surface of the MR. The non-reflowable ridge, on which it is placed, keeps the lateral dimensions intact [Leinse.2003].

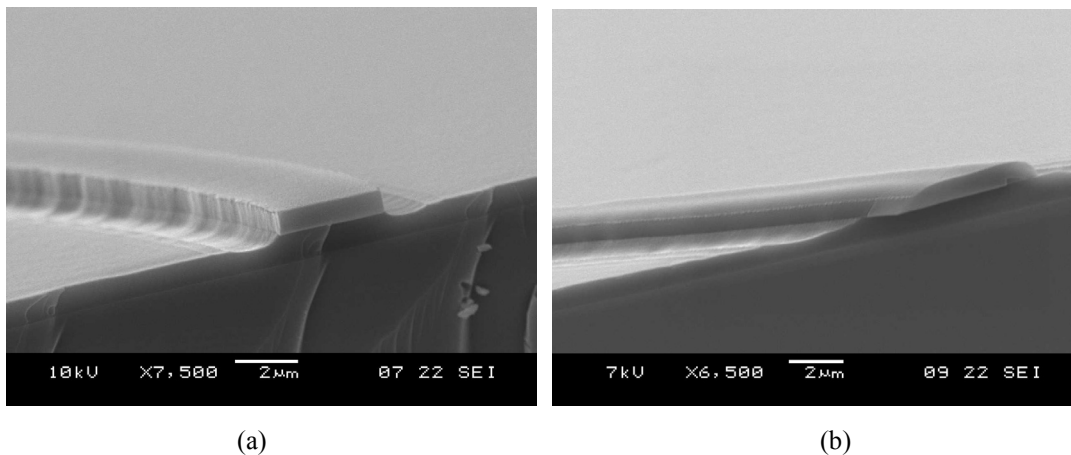


Figure 4.9: SEM photo of an RIE DANS MR on a Glassclad ridge a) before reflowing b) after reflowing

For PMMA-DR1 the same procedure is carried out and the smoothing of the MR reduced the scatterlosses from about 3dB/cm to approximately 1 dB/cm [Leinse.2004]. The measurements to obtain these values are discussed in the characterization chapter.

4.2.7 Topcladding spincoating

On top of the MR another layer of Glassclad is spincoated as a topcladding onto which the topelectrode can be deposited. In chapter 3 it was seen that this layer should have a minimum thickness of 4 μm above the MR. Two issues related to this topcladding are explained in some more detail here.

- The first issue is the wetting and adhesion of the Glassclad (intermediate) layer. Because the sample was etched by reactive ion etching, this layer was oxidized (see 4.2.4) and adhesion and wetting of the claddinglayer on top of this are good. A problem arises when the device is not processed directly after the etching and reflowing. If they are stored in a plastic waferbox, the plasticizers of the box condense

onto the Glassclad layer and another UV-ozone treatment is needed to prepare the surface again for applying a cladding layer.

- The second issue is the thickness of the claddinglayer. This layer should have a minimal thickness of 4 μm above the MR, which can't be applied in a single layer because a layerthickness of 4 μm in addition to the thickness of the MR is needed. This thickness can be reached by deposition of two layers, which makes planarization of the topcladding also better. A UV-ozone treatment in-between these two layers is needed to make sure that the adhesion of the cladding layers is good.

4.2.8 Electrode deposition

The final step in device realization is the deposition (over the entire wafer) and patterning of the topelectrode. In this last step another problem occurred. In a "standard" lithographic process the wafer undergoes a post exposure bake of 120 °C. Glassclad is a material which contains a lot of water when it is at room temperature. At 120 °C this water will be removed from the layerstack and with a topelectrode completely covering the layerstack, the water has no way out and will make the metal layer on top of the device crack. A picture of such a cracked/buckled electrode is given in figure 4.10.

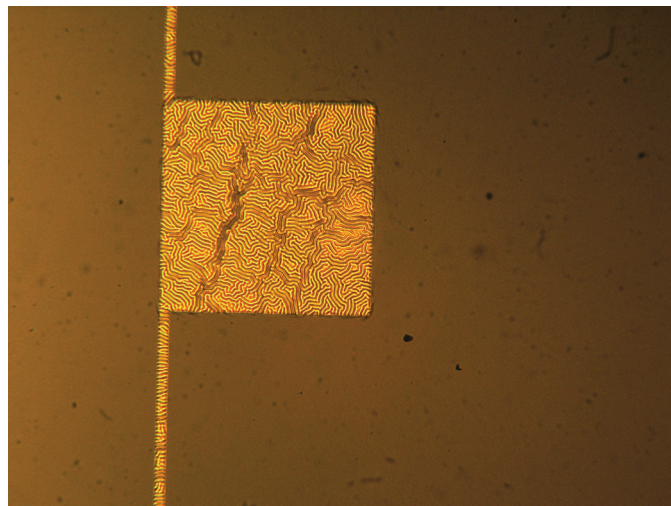


Figure 4.10: Buckles in topelectrode

This cracking can be prevented by not heating the sample during the lithography process. The soft bake before exposure can be left out by simply letting the resist-layer dry at ambient temperature. The solvent is removed slowly from the layer. The post exposure bake can be left out totally. It will only result in a small error in the electrode dimensions. Because the

electrodes are already a few microns larger than the MR, this doesn't matter and crack-free electrodes can be made using this procedure.

4.2.9 Interruptions in the fabrication process

When fabricating devices with polymer layer-stacks it is important to process the entire layerstack in one time interval. The time between applying two additional layers should be kept to a minimum. Two witnessed effects of inserting a break in the middle of the fabrication process are:

- The plasticizers of the plastic waferbox, in which the wafers are stored, will condense onto the toplayer of the stack, altering the wetting properties of this layer. Applying another layer on top can result in poor wetting and adhesion properties.
- By storing the wafer over a long period of time, the layerstack will densify by physical aging [Bradshaw.1997]. Applying another layer (with solvent) on top of this layer will result in local absorption of the solvent (and therefore local expansion), which can result in cracking of the layerstack.

4.2.10 Dicing

After the wafer is processed, a single wafer containing 6 groups (see appendix A1) of devices is ready for further processing. These devices have to be separated from each other for which, in integrated optical devices, there are normally 2 options. These options are:

- Cleaving. The device is broken along the crystal axis of the silicon wafer. This technique has two disadvantages.
 - o The exact position of the cleave-line is difficult to predict.
 - o The polymer-stack on this wafer doesn't break but tears. Therefore a smooth endface is very difficult to define. Schematic the cleaving of a polymer stack on a silicon wafer is given in figure 4.11.



Figure 4.11: Schematic representation of four steps in cleaving a silicon wafer with polymer layer stack

- Dicing. With a dice-blade, a cut is made through the wafer. This technique also has two disadvantages.
 - o The surface of a diced cut is relatively rough (compared to a cleaved one). This can partially be solved by using an index matching gel or adhesive when coupling light in (or out) with a fiber at such an endface.
 - o Because the dice-blade becomes hot during dicing, the blade must be cooled with water. Some polymers absorb this water and changes in the layerstack are induced. This issue can be overcome by spincoating a layer of positive resist over the entire devicewafer. This layer of resist will shield the device from the cooling water. An additional benefit of this resist-layer is that all the grit released in the dicing process will stick in this layer and can easily be developed away afterwards.

4.2.11 Poling

For the MR to become EO, it first has to be poled. The type of poling used to align the dipoles in the MR is electrode poling as described in chapter 2.2.5. During the poling the process is monitored by measuring the temperature and the current applied by the source. From the applied current the point of maximum poling (for a given voltage) can be estimated. In figure 4.12 an example of a measured polingcurve is given.

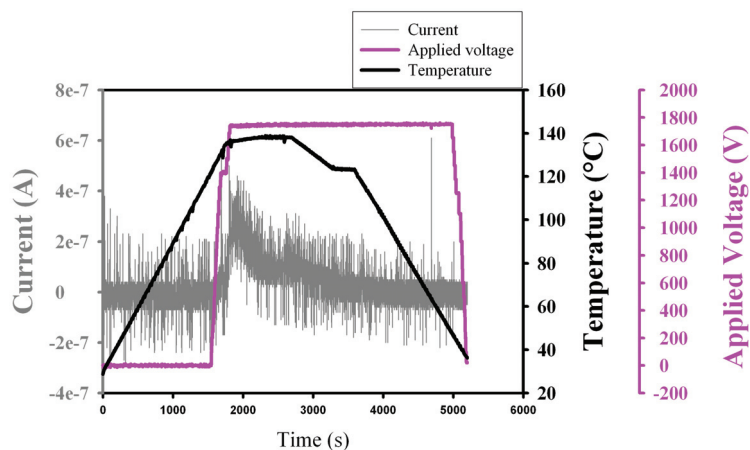


Figure 4.12: Measured polingcurve

From this curve it can be seen that the current delivered by the source reduces asymptotically for a given voltage. This means that the charge needed to compensate for the alignment of the dipoles decays. When the temperature is lowered a drop in ohmic conductivity can be

witnessed. From figure 4.12 it can be seen that for this case the dipoles need approximately 800 seconds to align.

4.2.12 Packaging

After poling the electrodes must be connected to a modulation source in order to characterize the device. Because the electrodes are used as lumped elements and the operating frequency will be around 1 GHz, these connections should be short. Less than 10% of the electrical wavelength as was described in chapter 3.2.4, which means 2 cm for this 1 GHz. The use of large probe pins to drive the electrodes should be avoided. To keep the connections to the electrodes as short as possible an RF connector is glued to the piece of device wafer and with short wires this connector is connected to the top and bottom electrode. A photograph of this connection is shown in figure 4.13.

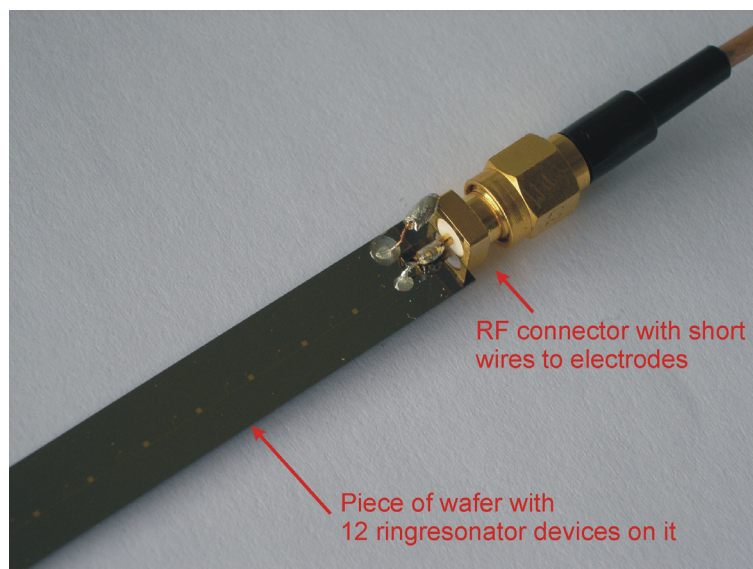


Figure 4.13: Photograph of the RF connector with wires connected to the top and bottom electrode. The width of the strip is 1 cm.

Because the wires from the connector to the device electrode are short the device-electrode can almost completely use the 2 cm of available length.

5 Characterization

For the design and characterization of the different devices, several measurement techniques are used to determine the properties of the materials and devices. This chapter will discuss these techniques and the outcome of the measurements. First the techniques and results of material characterization are described. The device behaviour is discussed in the second part of this chapter, after which conclusions are drawn. The specifications of all the measurement equipment used in this chapter is given in appendix A4.

5.1 Material properties measurements

In order to predict the behaviour of a designed device, the properties of the materials must be known. This paragraph will discuss the different characterization techniques and their results.

5.1.1 Ellipsometry

For the three device-materials, the spincurves (layer-thicknesses vs. rotation speed) and refractive indices had to be determined. An easy way to do this is using an ellipsometer setup (an M44 Woollam ellipsometer).

In an ellipsometer the polarization dependent reflection at interfaces with different refractive indices is used to measure the thickness and refractive indices of the different layers. The basic setup of an ellipsometer is shown in figure 5.1.

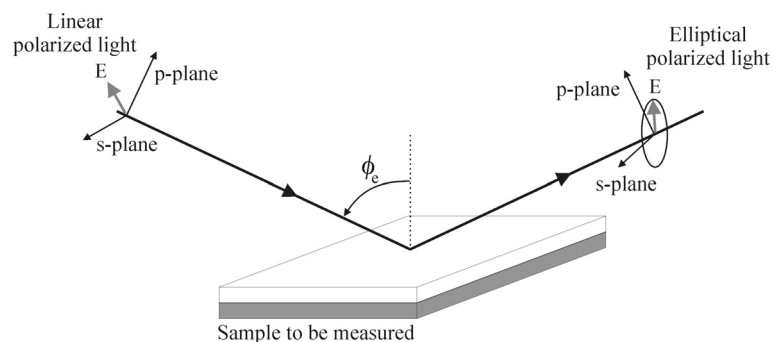


Figure 5.1: Basic principle of an ellipsometer

The measurement consists of shining a beam of light, of a known linear polarization under a certain angle (ϕ_e) on the layer to be measured. The layer will influence the polarization of the reflected beam and will change it to elliptical polarization. From this change in polarization the thickness and refractive index of the layer can be determined, because the reflected beam has different reflection coefficients for the two different polarizations (s and p). These coefficients are known as the Fresnel reflection coefficients (R_p and R_s) [Azzam.1977].

From the ellipsometry measurement ψ and Δ values are determined. These values are directly linked to the Fresnel coefficients by [Azzam.1977]:

$$\frac{R_p}{R_s} = \tan(\psi)e^{i\Delta} \quad (5-1)$$

ψ is the ratio of the magnitudes of R_p and R_s and Δ is the difference in their phase. Equation (5-1) alone isn't sufficient to determine both thickness and refractive index of a layer. To determine the thickness of a layer, the interference effect in a thin layer is utilized.

Multiple reflections of the incident beam lead to interference of the reflected light, which is schematically shown, with the different reflection and transmission coefficients, in figure 5.2.

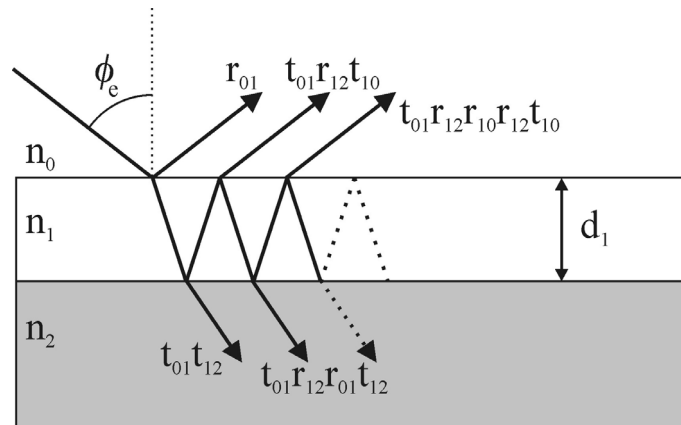


Figure 5.2: Multiple reflections in thin layer

The thickness of layer 1 (d_1) can be found from the propagation constant β_e and the Fresnell reflection coefficients. The following equations are needed for this.

$$\beta_e = 2\pi \left(\frac{d_1}{\lambda} \right) n_1 \cos(\phi_e) \quad (5-2)$$

in which λ is the wavelength used and n_1 the refractive index of layer 1. The addition of the infinite series of reflected waves leads to a resultant of the reflection which has been derived by [Azzam.1977]

$$R = r_{01} + t_{01}t_{10}r_{12}e^{-i2\beta_e} + t_{01}t_{10}r_{10}r_{12}^2e^{-i4\beta_e} + t_{01}t_{10}r_{10}^2r_{12}^3e^{-i6\beta_e} + \dots \quad (5-3)$$

Whose summation for the different polarizations gives [Azzam.1977].

$$R_p = \frac{r_{01}^p + r_{12}^p e^{-i2\beta_e}}{1 + r_{01}^p r_{12}^p e^{-i2\beta_e}} \quad (5-4)$$

$$R_s = \frac{r_{01}^s + r_{12}^s e^{-i2\beta_e}}{1 + r_{01}^s r_{12}^s e^{-i2\beta_e}}$$

The values for the refractive index and layer-thickness are found by measuring ψ and Δ and fitting a model (supplied by the manufacturer Woollam Co. Inc) to these measured values.

The measured values for the three different materials used in the devices were presented in chapter 3.1.1.

5.1.2 Resistivity measurements

As was already discussed in chapter 2, the EO material in the MR must be poled in order to have a net nonlinear effect. During the poling a DC electric field is applied, of which the division over the layerstack is determined by the resistivities of the different materials in this layerstack. In order to determine these resistivities samples are fabricated with the different materials. These samples consist of a layer of polymer sandwiched between a top and bottom electrode and these electrodes are shaped such that both can be reached by probe pins without mutual interference. This means that at the position where a probe pin on the top electrode is applied no bottom electrode is allowed. The electrodes are drawn schematically in figure 5.3.

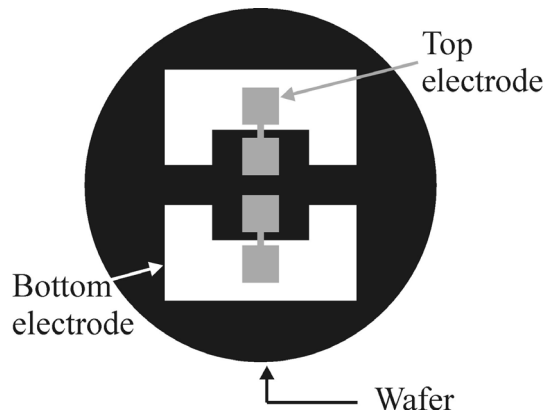


Figure 5.3: Schematic representation of the electrodes for the resistivity measurements

By applying a DC voltage between the top and bottom electrode, while heating the sample, and measuring the current (as a function of temperature) the resistivity can be calculated by,

$$\rho = \frac{RA}{l} \quad (5-5)$$

Where,

ρ is the electrical resistivity (Ωm)

R is the resistance of the layerstack (Ω)

A is the surface of the layer between top and bottom electrode (m^2)

l is the thickness of the layer between the electrodes (m)

The measurements were done at the Ecole Normale Supérieure de Cachan by Patrice Nagtegale, with the setup as shown in figure 5.4.

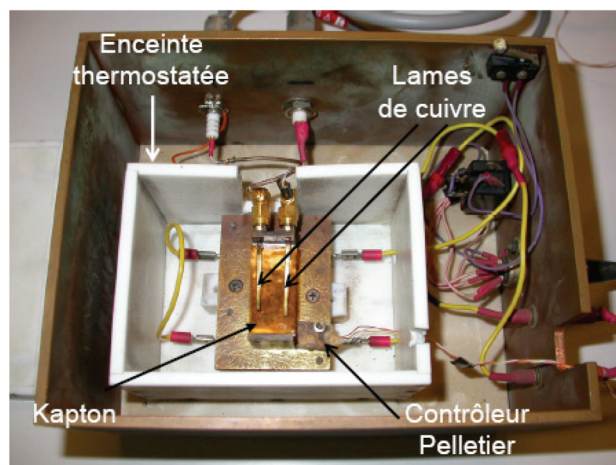


Figure 5.4: Photograph of the measurement setup used to measure the resistivities of the different layers (Source: P. Nagtegale).

The measured values are already discussed in chapter 3.1.1

5.1.3 Surface scattering measurements

An important cause of waveguide losses in integrated optical waveguides is the scattering caused by surface/sidewall roughness of the waveguide. These losses are in particular seen in RIE-ed waveguides and for the devices in this thesis these losses will therefore occur in the MR. To see how large these losses are and how much they can be reduced, a characterization setup is used [Leinse.2004] (appendix A3). This setup takes a photograph of scattered light from the top of a waveguide. In this case a spiral waveguide is used in order to make it as long as possible. The setup is schematically shown in figure 5.5.

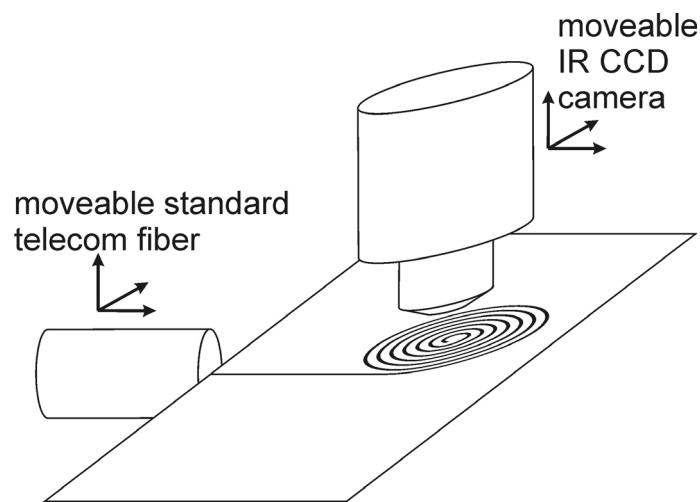


Figure 5.5: Schematic representation of the setup used to measure vertical scattering from a spiral waveguide

With the measurement-setup, the amount of scattered light from the waveguides in vertical direction can be measured. It is assumed that this is proportional to the amount of light in the waveguide. By analyzing the photographs taken by an IR sensitive CCD camera and determining the scattered light intensity at different distances along the waveguide, the decay of power in the waveguide can be determined. The measurement was done with a tunable laser at a wavelength of 1550 nm.

As explained in chapter 4.2.6 the loss induced by scattering can be reduced by reflowing the waveguide. From an etched waveguide, CCD camera-pictures are taken before and after reflowing. These pictures are given in figure 5.6.

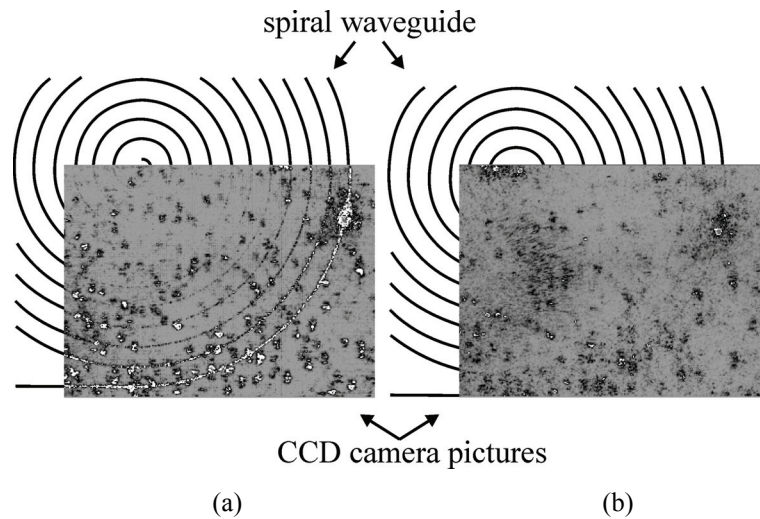


Figure 5.6: CCD Camera photos before (a) and after (b) reflowing of the spiral waveguide

From the pictures in figure 5.6, the pixel-intensities at different positions along the waveguide are determined by calculating the average pixel-intensities over a certain area/window in the picture with image processing software [LSPEC]. Schematically this is shown in figure 5.7.

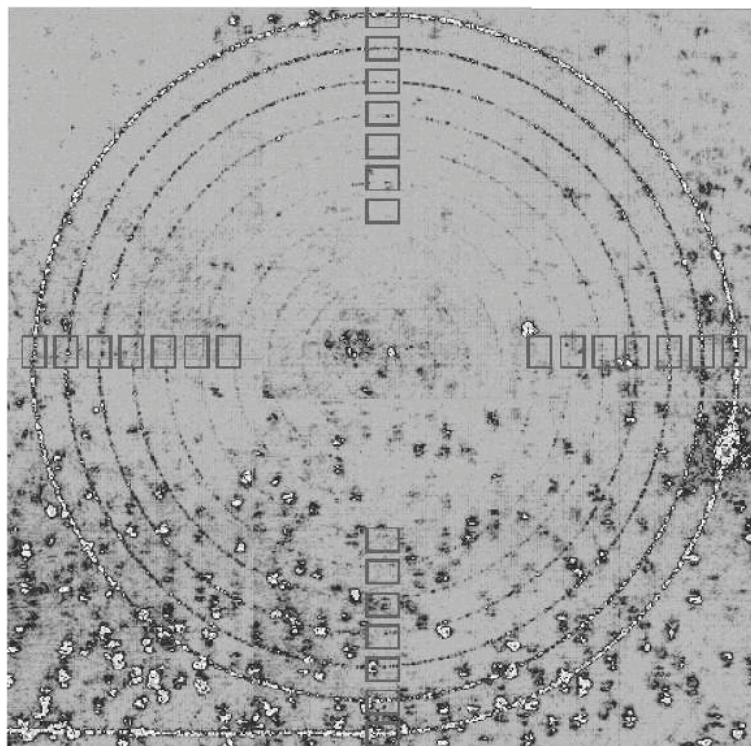


Figure 5.7: Positions of windows for calculating average pixel-intensity (before reflowing)

For each of the windows in figure 5.7 an average pixel-intensity over the window and the distance from the first window is known. With these values a graph can be made with the scattered light intensity vs. the distance along the waveguide. The slope of this graph will give

the loss of the waveguide. The measurements are done before and after reflowing and are given in figure 5.8.

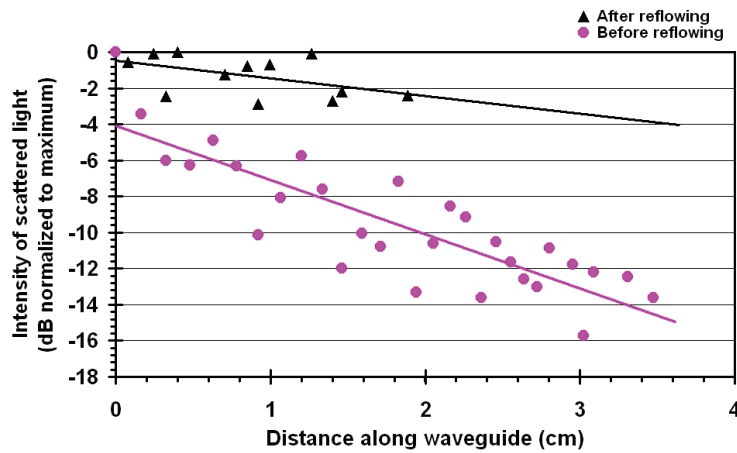


Figure 5.8: Amount of scattered light before and after reflowing.

From figure 5.8 it can be seen that the loss in the waveguide decreases from 3 dB/cm to 1 dB/cm when reflowing the layer.

5.1.4 Prism coupler loss measurements

After decreasing the scatter-losses it is very interesting to see which part of this loss is caused by scattering and which part is material loss. To see the difference between scatter and absorption losses, a prism coupling measurement is done. From a planar polymer waveguide almost no scattering is noticeable and the loss measured on this waveguide is therefore mainly caused by material losses. For these measurement, a layer of PMMA-DR1 of 0.8 μm thick is spincoated on a thick (approx 4 μm) Glassclad layer. By coupling light from a tunable laser in this layer with a prism, a propagating mode through a planar waveguide is launched. At a certain distance “d” a glass-plate is placed on top of this PMMA-DR1 layer in order to scatter the evanescent field in the direction of a camera placed above the glass-plate. The glass-plate is positioned on top of a thin layer of oil with the same index as the glass-plate. The same assumption as in the reflow-experiment is valid: The amount of scattered light is proportional to the amount of light in the propagating mode. Schematically this measurement setup is given in figure 5.9.

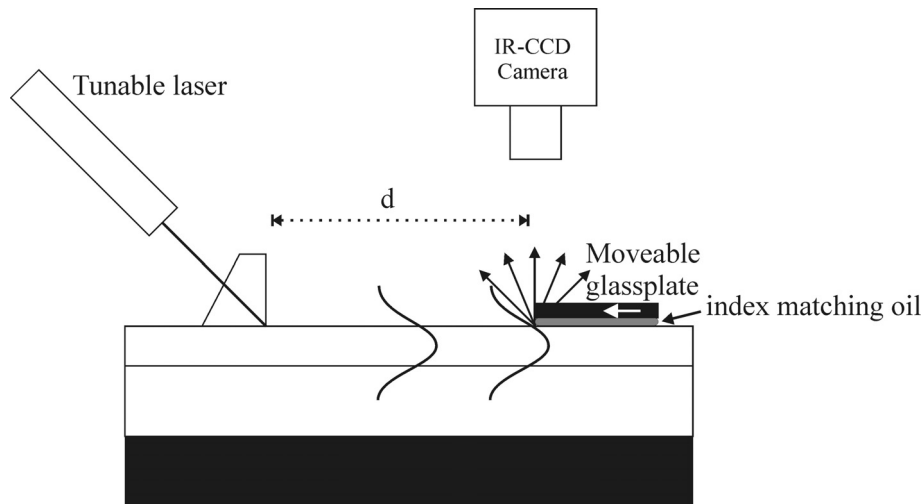


Figure 5.9: Schematic view of the prism coupling loss measurement setup

By varying the distance ‘d’, the loss can be calculated by the decline in the intensity of the scattered light. In figure 5.10 the measured values are given as a function of wavelength for different values of ‘d’. The four dots in figure 5.10 mark the results at 1550 nm.

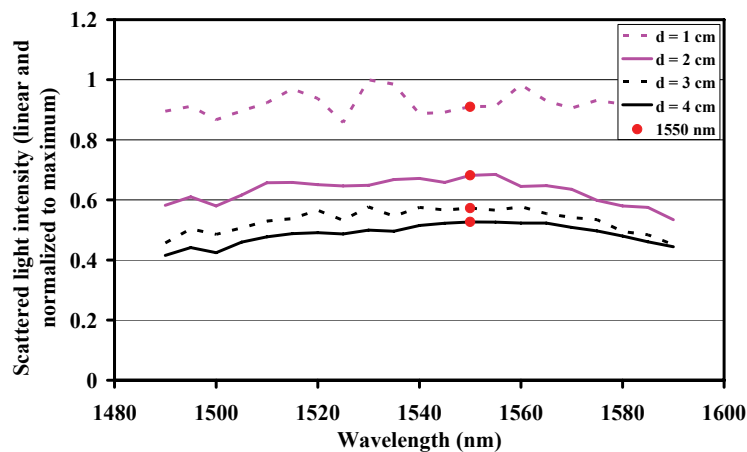


Figure 5.10: Amount of scattering measured with the camera for different wavelengths

From these values the optical loss per centimeter at 1550 nm can be found. The calculated loss is 0.8 dB/cm. Comparing this value to the 1 dB/cm found in the reflow experiments shows that the loss of the MR after reflowing mainly consists of material losses and has a small contribution (≈ 0.2 dB/cm), caused by scattering.

5.2 Device-measurements

To see whether the realized devices show the designed behaviour, they are characterized by coupling light in at the input waveguide and out again at one of the output ports. This

coupling is done by placing a cleaved fiber directly to the waveguide endface (butt coupling). Positioning the fibers relative to the waveguides is done with 6 different translation stages, all having an accuracy of at least 50 nm (a Newport PM500 alignment setup). A photograph of the setup is given in figure 5.11.

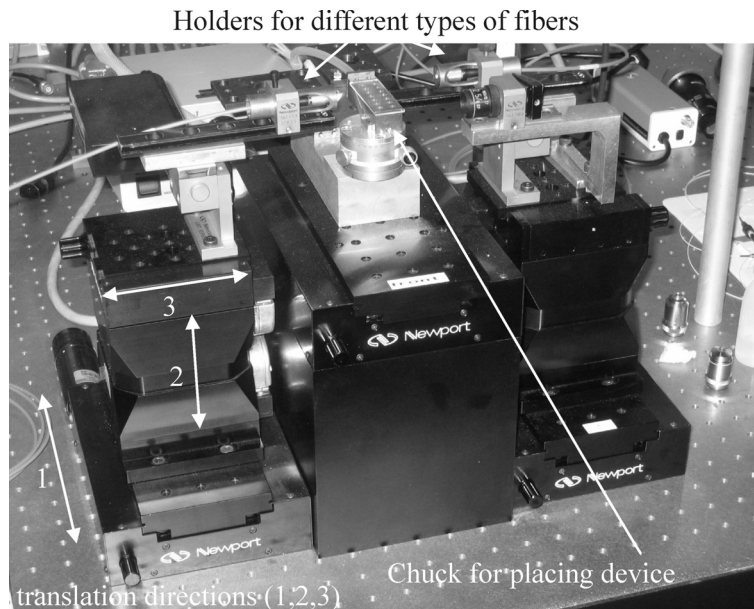


Figure 5.11: Newport PM500 setup used to align fibers to the optical device.

This paragraph will discuss the different measurements done on different devices. First the passive and active behaviour of an MR will be discussed, after which the MR combined with MZI will be discussed.

5.2.1 Passive MR-behaviour

In order to use the MR as an EO modulator, the optical spectrum of the device should have sharp dips in the through port spectrum. As was discussed in chapter 2 the MR-properties can be estimated from the measured spectra.

The setup that was used to measure the spectra from the MR is schematically given in figure 5.12.

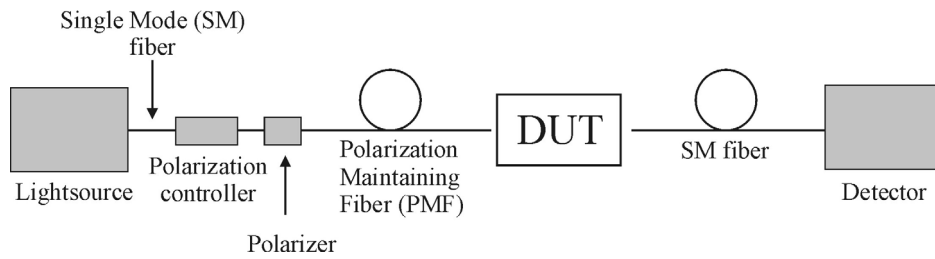


Figure 5.12: Setup used to characterize the passive behaviour of the MR.

The light-source can either be a tunable laser or a broadband light-source as for instance an Erbium Doped Fiber Amplifier (EDFA). With the tunable laser a ‘normal’ photodiode can be used as a detector because only one wavelength at a time is measured. When the EDFA is used, the detector must be substituted by a spectrum analyzer. Both measurement techniques have their pros and cons.

When using the tunable laser, the spectral resolution of the measurement is better compared to the EDFA/spectrum-analyzer measurement (here the spectral resolution is determined by the resolution of the spectrum analyzer). With the tunable laser, steps of 1 pm in wavelength can be measured.

A benefit of the measurements with the EDFA is the fact that the duration of measuring a spectrum is much shorter than scanning all individual wavelengths with the tunable laser. A faster measurement has less influence of thermal fluctuations and drift in it.

Because the high spectral resolution is only needed for very high finesse MRs, most measurements in this paragraph are done with the EDFA and spectrum analyzer, because the realized devices had a relatively low finesse.

For different MR-radii on several device-wafers the spectra were measured. In some cases only the through port spectrum could be measured and for a few larger rings the drop port spectrum could also be measured. When using the MR as a modulator, the through port spectrum is the most interesting, because the amount of optical power that can be measured is larger than at the drop port and this makes it easier to measure the modulation. Also in case an MR is placed at one of the branches of an MZI only a through port is used.

The first measurement shown here is a through port measurement of an MR with a radius of 100 μm . The separation (it) between disc and waveguide was designed to be approximately 0.35 μm (the spinspeed was 5000 rpm, resulting in a Glassclad layer of approximately 1.1 μm). The offset (x) between MR and waveguide was designed to be +3 μm . In figure 5.13 the TE and TM spectrum of this MR before poling are shown.

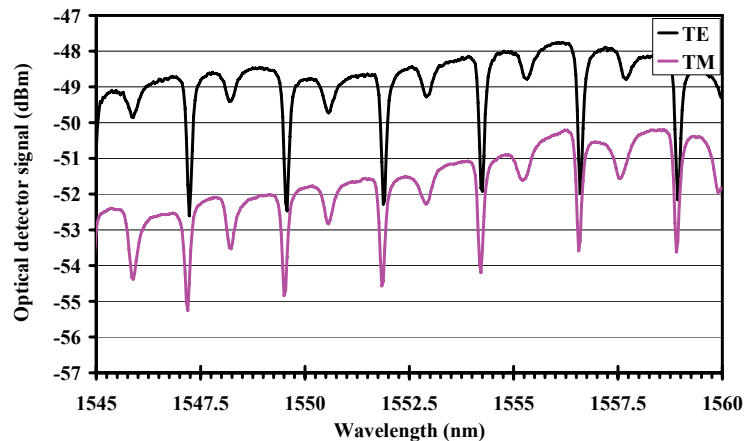


Figure 5.13: Through port spectrum of a PMMA-DR1 MR with a radius of 100 μm (before poling)

It can be seen that the shape of the MR-spectrum is caused by more than one optical mode. In between the sharp dips, smaller dips of a higher order mode can be noticed. When the MR is used as a modulator, these modes don't matter because only a flank of a dip of the zero order mode is used. From figure 5.13 it can also be seen that the birefringence in the unpoled MR is close to zero because the position of the resonance wavelengths for both TE and TM is equal.

From figure 5.13 the typical MR-parameters (FSR and finesse), as were described in chapter 2, are derived. The derived FSR is 2.4 nm, which is in accordance to the theoretical value (equation (2-18)) of an MR with a radius of 100 μm and an effective index of the bend-mode of approximately 1.5. The finesse derived from figure 5.13 is approximately 10 and is dependent of the loss of the MR, as was shown in equation (2-22)

$$m = \frac{F}{2\pi} \quad (2-22)$$

In which m is the number of roundtrips after which the optical power of the mode in the MR is reduced by a factor of $1/e$. Determining F gives a value of m and from this value an order of magnitude for the optical loss can be determined. In figure 5.14 a graph is made of the optical loss versus the finesse for different ring-radii.

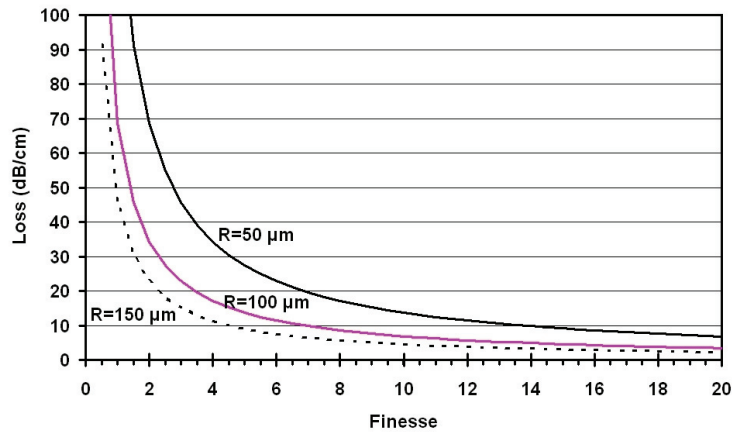


Figure 5.14: Ringloss as a function of finesse for different ringradii

From figure 5.14 it can be seen that for the finesse of 10 (derived from figure 5.13) the loss of the MR should be in the order of 5 to 10 dB/cm.

This is relatively large compared to the 1 dB/cm found after reflowing a PMMA-DR1 waveguide (paragraph 5.1.3). This difference is probably caused by the Glassclad cladding around the MR. At the Ecole Normale Supérieure de Cachan, spectro-photometric measurements were done on the Glassclad and a loss of approximately 9 dB/cm was found. Because part of the evanescent field of the MR is propagating through this layer, this loss will contribute to the total bend-loss of the MR.

Besides deriving the FSR and finesse from figure 5.13, the measured data can further be analyzed with analytical software [RFIT]. This software fits a theoretical model to the measured data, with the two coupling constants (κ_1, κ_2) and the bend-loss in the MR as the variable fit parameters.

For a realistic fit, the approximate values of the MR's coupling constants and loss should be known. The coupling constants can be found from figure 3.27, in which they were obtained from simulation (for TM polarization) for different values of 'it' and x (which were respectively the vertical and horizontal offset between MR and waveguide). The different coupling constants are given in figure 5.15, for different values of 'it'. The measured MR has a value of 'x' around 3 μm.

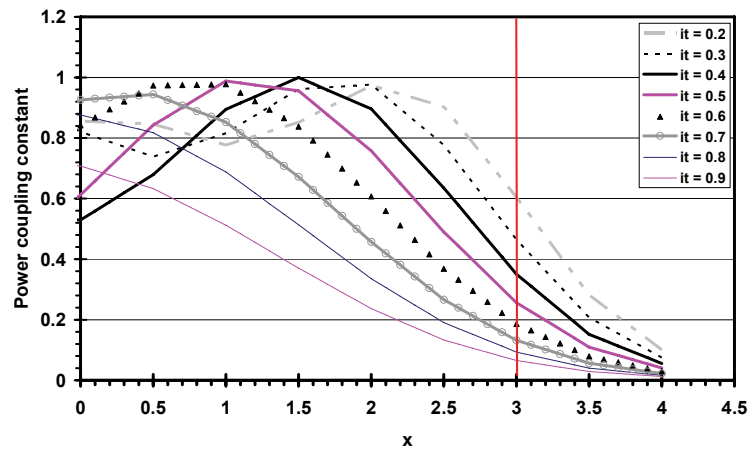


Figure 5.15: Coupling constants from simulation of an MR with a radius of $100 \mu\text{m}$ with a $4 \mu\text{m}$ wide waveguide.

From figure 5.15 it can be seen that the coupling constants should be approximately between 0.1 and 0.6 because the vertical distance ('it') between MR and waveguide should be in the range from 0.2 to 0.9 μm . This range can be used in finding a model for which the fit will match the measurements. The loss is chosen in a range from 4-16 dB/cm, because from figure 5.14 it was concluded that the loss should be in the order of magnitude of 5-10 dB/cm. In order to see how unambiguous a fit result (with minimum error) is, the software also calculates the difference between the calculated model-spectrum (output vs. wavelength) and the measured spectrum. The model with the lowest error has the best fit. For the measured spectrum from figure 5.13 there was a range with low error values. When plotting the points where these low error-values occur in a 3D plot (with the two coupling constants and the loss as variables) a clear trend can be seen. Figure 5.16 shows the points with the lowest error for the different κ_1 , κ_2 and loss values.

It can be seen that there is a single κ_1 ($\kappa_{1\text{fit}}=0.3$) for which the error is lowest and that for these low error values $\kappa_2 \neq \kappa_1$, which implies a misalignment of the MR to the waveguides. From figure 5.16 the theoretical model for an MR, as was described in chapter 2 (figure 2.16), can be seen because the coupling from the MR to the drop port can also be represented by a discrete drop (or loss) of power in the MR. After a single roundtrip through the MR, the optical field will need a certain amount of power coupled in, to compensate for this loss, in order to build up resonance. If the loss in the MR increases, this should be compensated by coupling less light from the MR to the drop port waveguide. From figure 5.16 it can be seen that κ_2 is in the order of 0.4-0.6. Figure 5.17 shows two of the fit results, one on the low side of the loss range and one on the high side of the loss range, with the corresponding κ_2 values.

It can be seen that the two fits are almost identical. In order to determine κ_2 unambiguously, also the drop port spectrum must be measured.

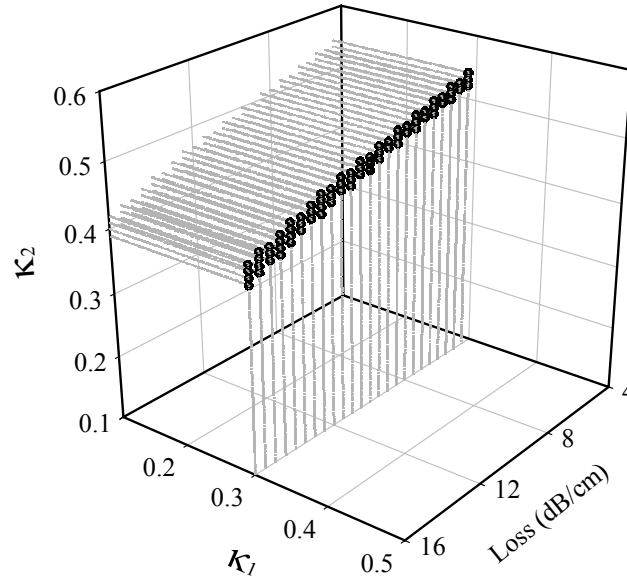


Figure 5.16: Points with the lowest fit error as a function of κ_1 , κ_2 and the loss in the MR

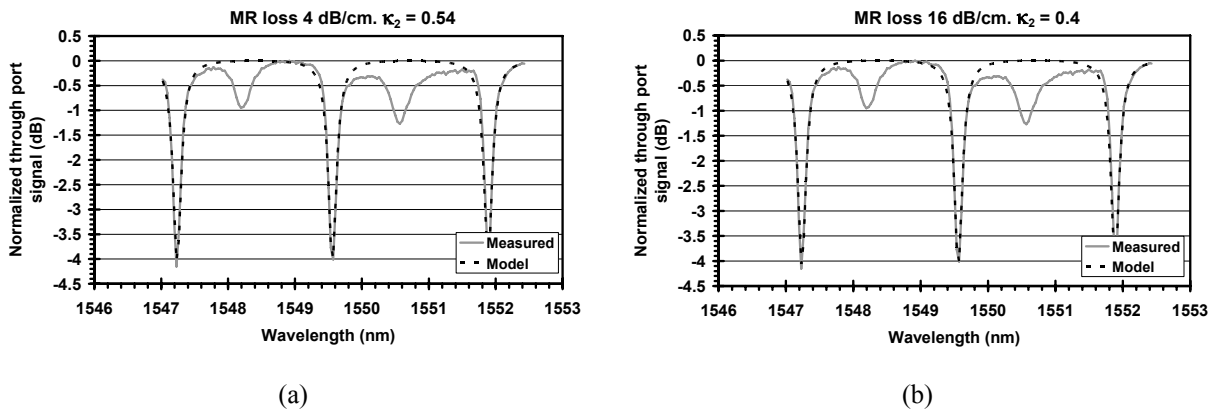


Figure 5.17: Comparison of two fits (a) Lower loss with higher κ_2 . (b) Higher loss with lower κ_2

In order to get an estimate of the vertical spacing and horizontal misalignment between the MR and the waveguides, the data from figure 5.15 and 5.16 is combined. On the fabricated mask, the MR has a spacing (x) between MR and waveguide of $3 \mu\text{m}$. A small misalignment of the MR will result in a different spacing for the through and drop port, and therefore also different coupling constants (κ_1 and κ_2). Schematically this misalignment is shown in figure 5.18.

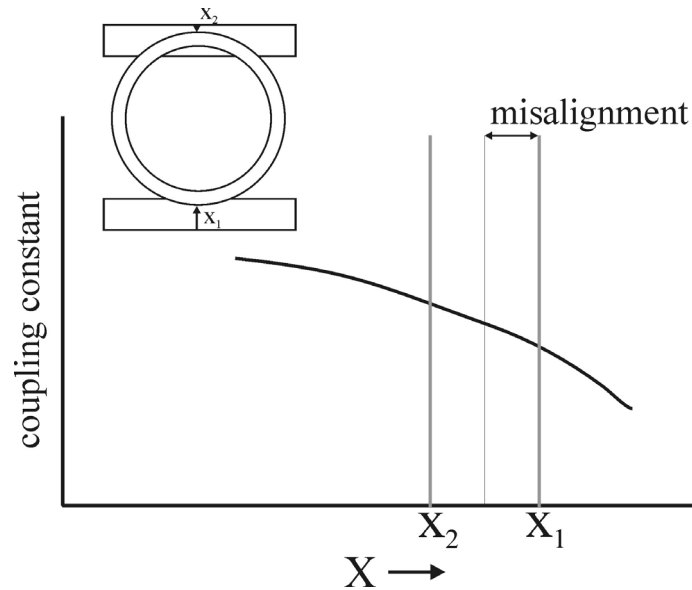


Figure 5.18: Asymmetric coupling constants caused by misalignment

It was already seen that $\kappa_{1\text{fit}}$ is 0.3 and κ_2 somewhere between 0.4 and 0.6. From the coupling constants simulations (figure 3.27), the simulated coupling constant κ_1 ($\kappa_{1\text{sim}}$) can be found (figure 5.15). A misalignment means a variation in the coupling constants (due to a variation of 'x') around $x=3\mu\text{m}$. In order to get an estimate for the misalignment, the difference between the simulated κ_1 ($\kappa_{1\text{sim}}$) and the fitted κ_1 ($\kappa_{1\text{fit}}=0.3$) is calculated for different misalignment values (with $\kappa_{1\text{sim}}$ from figure 5.15). This is done for each different vertical spacing ('it'). The results of this calculation are in figure 5.19.

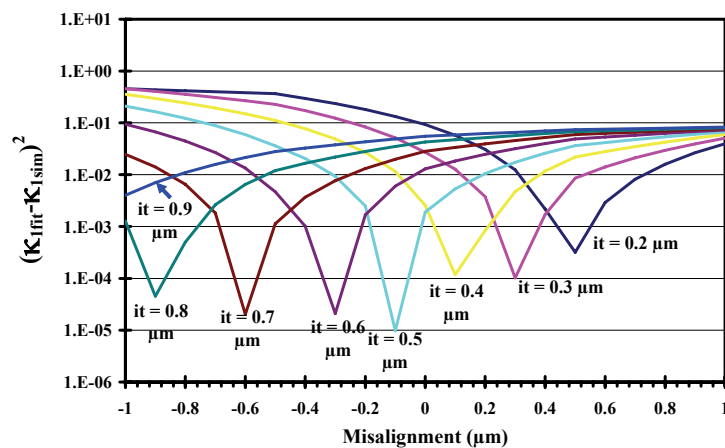


Figure 5.19: Difference between simulated and fitted coupling constant for different misalignment.

From figure 5.19 the amount of misalignment for which the simulated $\kappa_{1\text{sim}}$ and the fitted $\kappa_{1\text{fit}}$ are closest can be found. With x_1 known for the different values of 'it', x_2 is also known and

the corresponding coupling constants can be calculated from figure 5.15. This is done for each vertical spacing ('it') and a graph is made from κ_2 vs. 'it'. This graph is shown in figure 5.20.

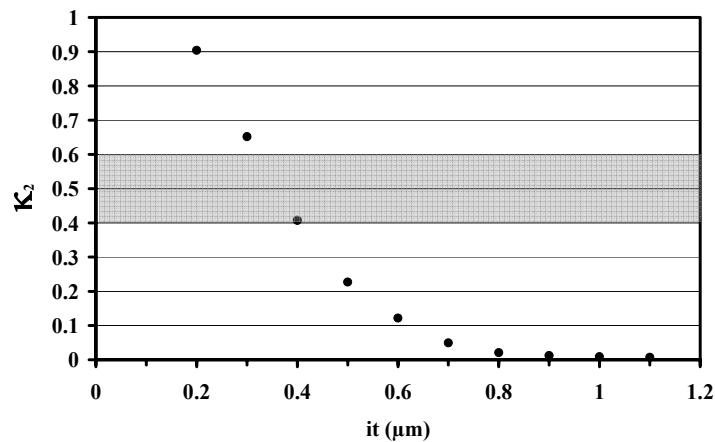


Figure 5.20: κ_2 (at the calculated values of x_2) for the different layer-thicknesses.

Because it was found that κ_2 should be between 0.4 and 0.6, it can be seen that the vertical gap between the MR and waveguide should be between 0.3 and 0.4 μm . This is well in accordance to the designed 0.35 μm gap. With this spacing ('it') the misalignment of the MR can be found from figure 5.19. It can be seen that the misalignment is approximately 0.2 μm . The second device that will be discussed is an MR on a different device-wafer than the previous one. The largest difference between these two device-wafers is the spinspeed at which the intermediate layer between MR and waveguide is applied. The spinspeed at this wafer was around 4000 rpm (which should result in a Glassclad layer of 1.2 μm), resulting in a gap ('it') between MR and waveguide of approximately 0.45 μm . The device consists of an MR with a radius of 150 μm and the horizontal offset (x) is designed to be -0.5 μm . This MR was poled at a voltage of 1500 volts, applied over a layerstack of 11 μm for 15 minutes at 145°C. On this device it was possible to measure both the through and the drop port spectrum for both TE and TM polarization. Poling induced birefringence can be seen in this spectrum because the TE and TM resonance wavelengths are different.

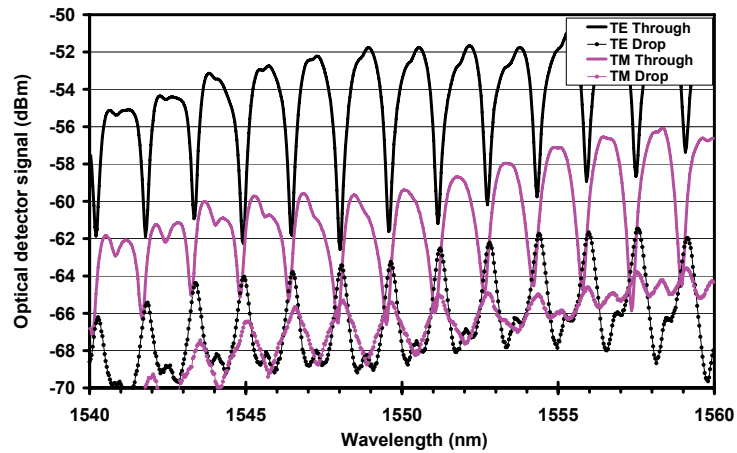


Figure 5.21: Through port spectrum of a PMMA-DR1 MR with a radius of 150 μm

In this case, the characteristic parameters can be estimated from a fit to both the through and the drop port spectra.

The values found for the fit with a minimum error are given in table 5.1.

	TE	TM
κ_1	0.77	0.85
κ_2	0.72	0.83
Loss (dB/cm)	30	38.5

Table 5.1: Fit values from program Rfit [RFIT]

The coupling constants for this MR, simulated in chapter 3 (figure 3.27) are given in figure 5.22 for the TM polarization. From figure 5.22 it can be seen that the fit values for the coupling constants are in accordance to the simulated values for a vertical spacing ('it') between MR and waveguide of approximately 450 nm.

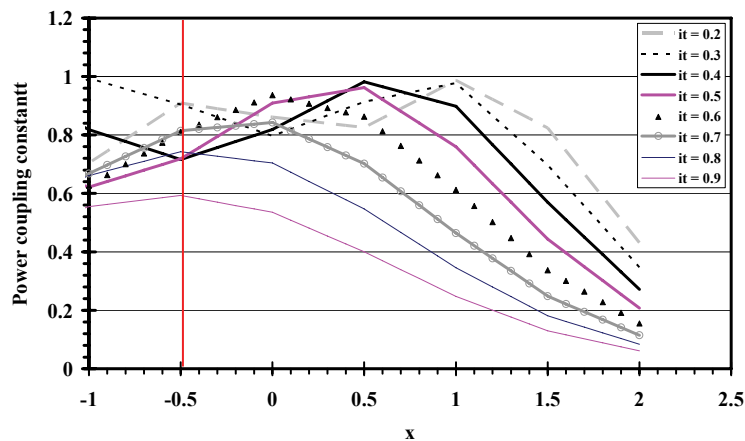


Figure 5.22: Simulated coupling constants for an MR with a radius of 150 μm for different values of 'it'

Estimating the misalignments from these fit values is almost impossible because the coupling constants are not very sensitive to the position x , as can be seen in figure 5.21.

5.2.2 Thermal tuning

The high thermo optic effect of polymers can be an advantage and a disadvantage. For thermo optic tuning/modulation this large effect is useful to reduce power dissipation, but when the MR is used as an EO modulator, the position of the resonance dips shouldn't change at ambient temperature changes. Very accurate temperature control is needed (see also chapter 2), because the shift in resonance wavelength is theoretically in the order of 10^2 pm/°C. To see how large the effect on the position of the resonances is in practice, a through port spectrum of an MR was measured while heating the chuck on which it was placed in the characterization setup. The MR on which the measurement was done had a radius of $150\ \mu\text{m}$, a vertical distance (it) of $0.5\ \mu\text{m}$ and a horizontal offset of $-0.5\ \mu\text{m}$. The measurement was done for the TE mode with a setup as schematically shown in figure 5.23. The TM mode shows the same behaviour.

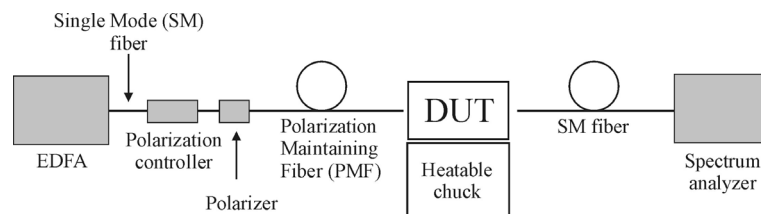


Figure 5.23: Schematic representation of the thermal tuning measurement setup

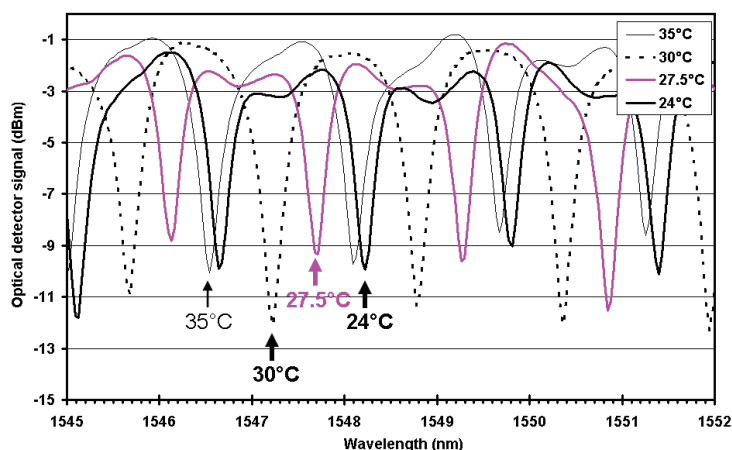


Figure 5.24: Through port spectrum for TE of a PMMA-DR1 MR with a radius of $150\ \mu\text{m}$ for different temperatures.

From figure 5.24 the thermo optic coefficient of the MR can be found. The average shift in resonance wavelength in figure 5.24 is $150\ \text{pm}/^\circ\text{C}$. For a wavelength of $1550\ \text{nm}$ and a group

index of the mode in the MR of 1.5 this results, with equation (2-27), in a thermo optic coefficient of $1.5 \cdot 10^{-4}$, which is in accordance to the typical values for polymers already discussed in chapter 2.2.2.

5.2.3 Electro-optic modulation in MR

After successful poling of an MR (the poling curve was already given in chapter 4 figure 4.12) the MR could be modulated. In order to apply an electric field over the MR, the top and bottom electrode of the device are connected to a modulation source via RF probe connections (as were shown in chapter 4.2.12). The setup is schematically shown in figure 5.25.

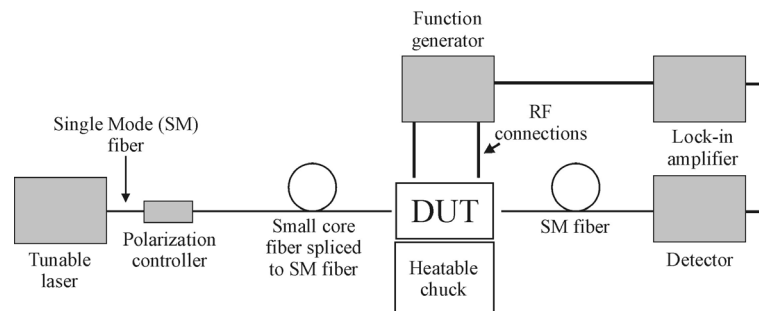


Figure 5.25: Schematic representation of the thermal tuning measurement setup

Coupling in with a polarization maintaining fiber wasn't needed because the TM mode had about 20 dB more loss than the TE mode. The higher loss for the TM polarization is probably caused by an error in the thickness of the buffer-layer. Because this layer is slightly thinner than designed, the TM mode senses the electrode underneath, giving it higher loss than the TE mode. The measurements are therefore done for TE polarization only.

The device consisted of a PMMA-DR1 MR with a radius of $100 \mu\text{m}$. On this MR no dips in the through port were measurable, but in the drop port “large” peaks could be measured for the TE polarization. The lack of dips in the through port is probably caused by “high” losses in the MR and asymmetric coupling constants. For certain combinations of ring loss and coupling constants it is possible to have a “flat” through response and large peaks in the drop port. The spectrum of the drop port is given in figure 5.26. This MR was poled at a voltage of 1500 volts, applied over a layer stack of $11 \mu\text{m}$ for 15 minutes at 145°C .

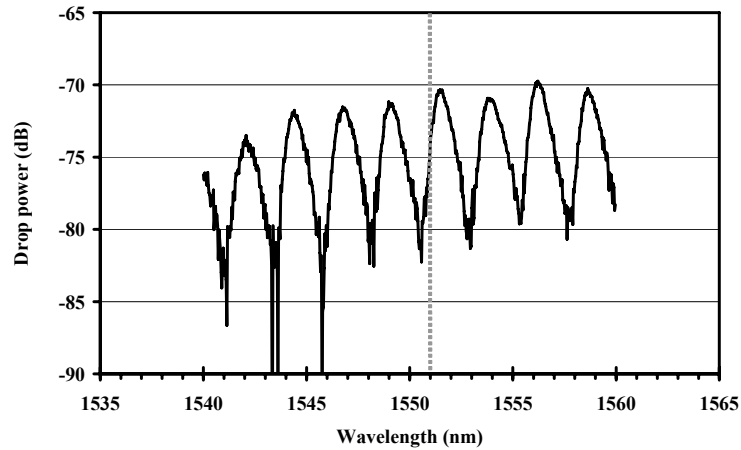


Figure 5.26: Measured drop port spectrum of a PMMADR1 MR with 100 μm radius for TE polarization

The tunable laser was set to a wavelength of 1550.9 nm (on the flank of the peak around 1550 nm, the dotted grey line in figure 5.26) and -38 dBm was measured at the end of the drop port. A modulation signal of 5 Vpp (1 kHz) was applied between top and bottom electrode and with a lock-in amplifier (phase sensitive detection) the signal from the optical detector was measured. A modulation ripple of around 1.5 % was measured on the drop port signal. Because this signal is already at -38 dBm, the modulation signal is in the order of -55 dBm, which is close to the background noise when shown on an oscilloscope (high speed measurements were therefore not possible with this sample).

The depth of the optical modulation ripple was calculated from the measured lock-in values (in combination with the specifications of the detector). This ripple is caused by a shift of the wavelength spectrum and with the slope of the peak at 1550.9 nm, the wavelength shift can be calculated and has a value of about $4 \cdot 10^{-3}$ nm.

With $\frac{\lambda \Delta n_g}{n_g} \approx \delta \lambda$ equation (2-27) the value for Δn_g can be calculated if $\delta \lambda$ is known. $\delta \lambda$ is

$4 \cdot 10^{-3}$ nm and $n_g \approx 1.49$. At $\lambda = 1550.9$ nm this gives a value of Δn_g of $4 \cdot 10^{-6}$.

With $\Delta n_1 = -\frac{1}{2} r_{13} E_3 n_1^3$ (equation (2-9)) given for the index change in the MR due to an applied electric field, a minimum value can be calculated for r_{13} , when assuming that $\Delta n \approx \Delta n_g$ (in reality $\Delta n > \Delta n_g$ depending on the amount of light in the MR and cladding). Assuming a homogenous electric field in the layerstack, the value for r_{13} is estimated to be between 2.5 and 4.5 pm/V. Using a ratio between r_{13} and r_{33} of 3 (chapter 2), this will give a value of r_{33} of approximately 7.5 – 14 pm/V, which is in accordance to the values found in literature [Liang.1994] [Michelotti.1999] [Michelotti.2003].

Another device on which modulation has been measured was a PMMA-DR1 MR with a radius of 150 μm . This MR was poled at a voltage of 1500 volts, applied over a layerstack of 11 μm for 15 minutes at 135°C. In this sample the TM dips in the through port were again much lower (higher loss) than the TE dips (the device was on the same wafer as the previous measurements, consequently it has the same buffer-layer thickness). The TE dips were used for modulation measurements.

The spectrum of the MR is given in figure 5.27.

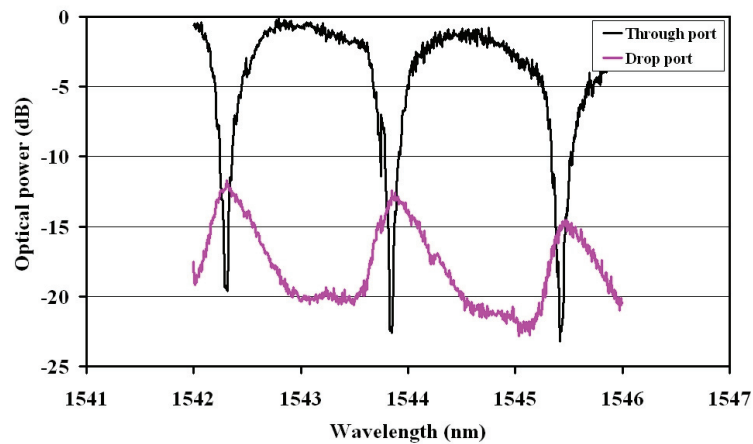


Figure 5.27: Through and drop port spectrum of a PMMA-DR1 MR with a radius of 150 μm

Unfortunately the poling of this sample wasn't as good as the previous one. The r_{33} values measured with this device were between 2 and 4 pm/V.

For the TE mode of this sample the parameters of the MR were determined again with the Rfit [RFIT] software. The parameters that were determined are given in table 5.2.

κ_1	0.83
κ_2	0.7
Loss (dB/cm)	15.2

Table 5.2: Device parameters determined with the Rfit software [RFIT]

These parameters are in accordance to the loss that can be estimated from figure 5.14 and the order of magnitude of the coupling constants that were found in the simulations in chapter 3.

Due to photo-degradation (as will be described in paragraph 5.3) the EO effect diminished while measuring and no high speed modulation could be measured.

A third device (a PMMA-DR1 disc with a radius of 150 μm) on which modulation was measured showed again a through port spectrum with a TM mode having a lot more loss than the TE mode. Because of the stronger signal from the TE mode, the modulation measurements were done with this polarization. The poling of this MR was done by applying 1600 volts over the layerstack of 10 μm . The voltage was applied at 145°C for 15 minutes. The measured spectrum of this device is given in figure 5.28.

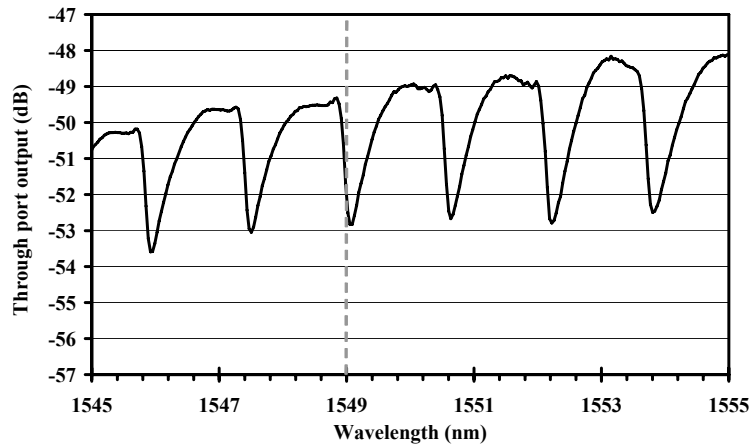


Figure 5.28: Through port spectrum for TE polarization of a disc with a radius of 150 μm .

The wavelength at which the modulation was measured was set to 1549 nm (grey dotted line) and again a modulation voltage of 5Vpp was applied between top and bottom electrode. The measured r_{33} was again measured with the lock-in amplifier and a value around 12 pm/V was determined. The optical signal from the through port was also measured with an optical detector and an oscilloscope (instead of the detector lock-in combination). The modulation was measurable up till 50 MHz (figure 5.29)

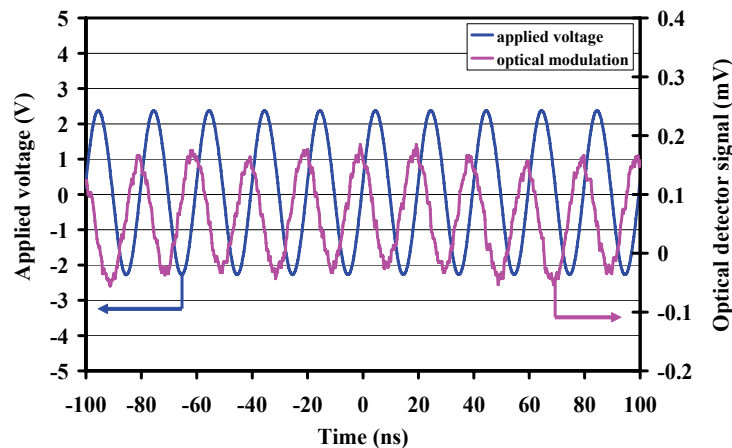


Figure 5.29: 50 MHz modulation signal of PMMA-DR1 MR with a radius of 150 μm

Beyond 50 MHz the modulation depth diminishes. This was probably caused by two reasons.

- The optical detector used in this measurement was suitable to measure signals up to 125 MHz and already started to lose sensitivity around 50 MHz.
- The top-electrode of the MR was used as a lumped element and therefore the reflection at the end of the electrode doubled the modulation voltage (paragraph 3.2.4). When measuring the electrical reflection of this top electrode (with a network component analyzer) it was seen that it reduced for frequencies above 10 MHz (figure 5.30). This is probably caused by the decrease in the capacitance reactance for higher frequencies. The capacitance reactance (X_c) is given by [Lorrain.1988]

$$X_c = \frac{1}{\omega C} \quad (5-6)$$

In which ω is the frequency of the electrical signal and C the capacitance of the layerstack. Reducing this value brings the capacitance reactance closer to 50Ω , which lowers the reflectance and therefore lowers the applied voltage by at most a factor of 2.

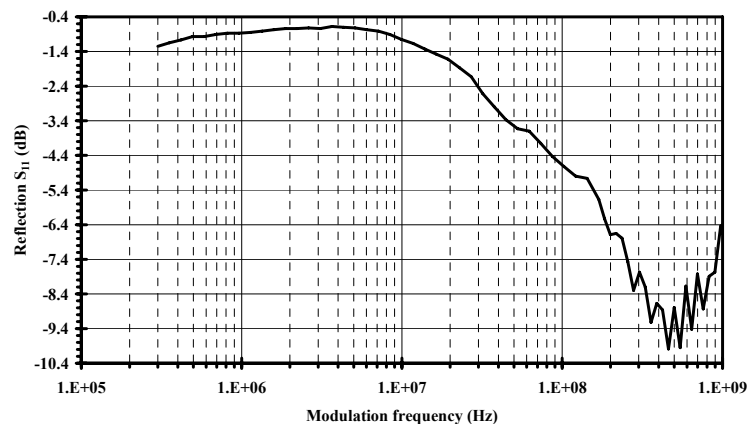


Figure 5.30: Electrical reflection of topelectrode vs. modulation frequency

5.2.4 Electro-optic modulation in MR with MZI

As was already described, also MZI devices with an MR on one of their branches are realized. These devices are less sensitive for misalignment of the MR relative to the waveguides. A device on which successful measurements were done, consists of a disc of PMMA-DR1 with a radius of $150 \mu\text{m}$. This disc was poled with a total voltage of 1600 volts over the $9.5 \mu\text{m}$ thick layerstack for 15 minutes at a temperature of $145 \text{ }^\circ\text{C}$. There is only a through port to

measure and also for this device (fabricated in the same batch as the previous ones) the TM mode has much higher loss than the TE.

While coupling in light at the input waveguide, the spectrum is measured at the output waveguide. For the TE mode this spectrum shows two sets of resonance lines originating from two resonator modes, see figure 5.31.

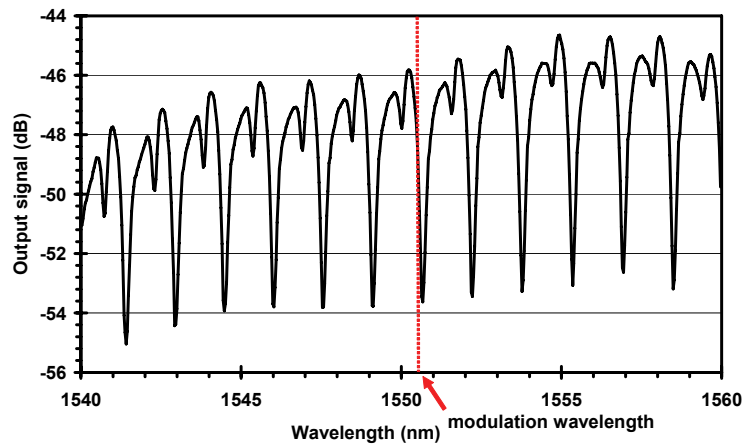


Figure 5.31: Measured spectrum (TE) of the MR-MZI device. The vertical line is the wavelength of the CW tunable laser at which modulation was measured

While applying a modulating voltage between top and bottom electrode, the amount of optical modulation is measured. Again from the depth of the modulation ripple combined with the detector properties and the measured spectrum, the wavelength shift of the spectrum is determined. The change in the refractive index of the MR-material can be calculated from this shift because it's only caused by the MR and not by the MZI. With the electric field applied known, the EO coefficient is determined and an r_{33} value of approximately 10 pm/V is found for this device, indicating successful poling of this device [Liang.1994] [Michelotti.2003].

The frequency of the applied modulation voltage is changed by a network component analyzer (NCA) and the modulation depth as a function of the electrical frequency is determined. These measurements were done with and without an electrical amplifier between the NCA and the electrode, and the optical detector is shielded from electrical disturbances by packing it in metal foil. The amplifier is used to increase the limited voltage applied by the NCA and the setup is schematically shown in figure 5.32.

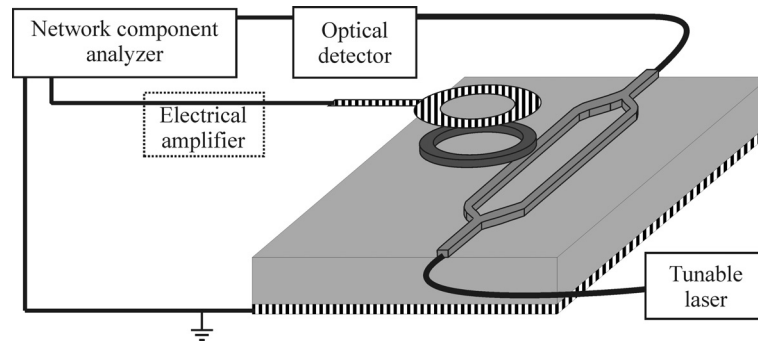


Figure 5.32: Schematic representation of the used measurement setup

The detector that was used had a spectral response which started to decay around 1 GHz. This spectral response was measured and the device response was corrected for this response. The detector response and the different measurements are shown in figure 5.33 and 5.34.

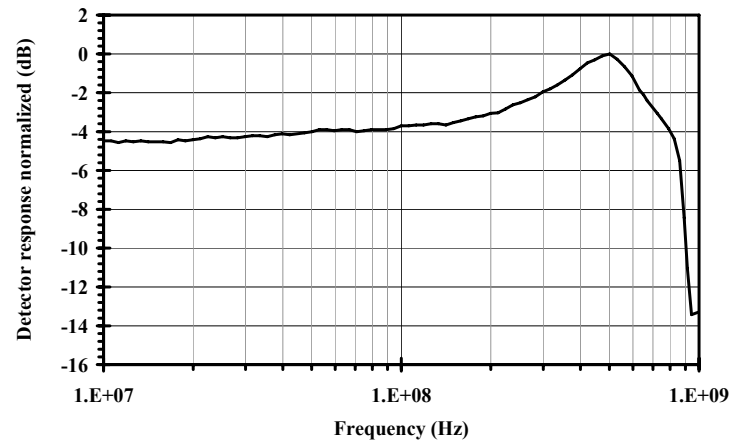


Figure 5.33: Detector response of the used detector.

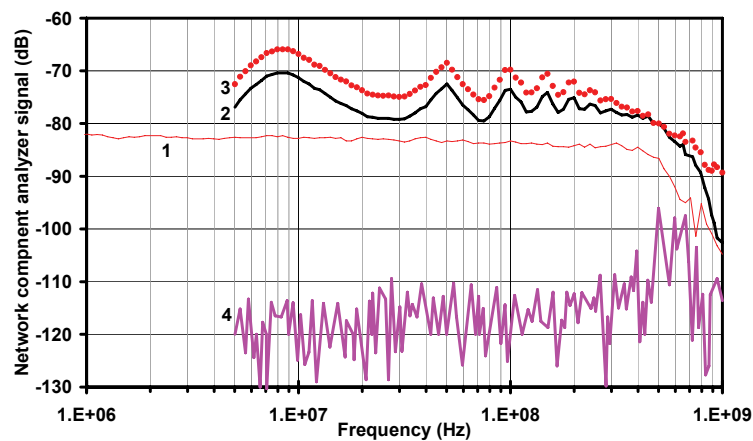


Figure 5.34: Measured frequency spectrum of the MR MZI device

In figure 5.34 four traces are shown. These are:

1. Measured frequency response of the device without electrical amplification and detector correction
2. Measured frequency response of the device with electrical amplification and without detector correction
3. Measured frequency response of the device with electrical amplification and with detector correction
4. The noise signal of the detector (with the laser power off)

In lines 2 and 3 a modulation can be seen with a periodicity of 50 MHz. This is probably caused by the amplifier which gets back reflections from the electrodes. This modulation is not caused by the device because in trace 1 the frequency response is flat. It can be seen that modulation frequencies up to 1 GHz can be measured. With this performance, data-rates exceeding 1 Gbit/s can be transmitted. With some specific modulation techniques (like for instance quadrature amplitude modulation [Couch.1993]), data-rates of 2 to 3 Gbit/s will be possible. The roll-off above 500 MHz is probably caused by the layerstack. The capacitance reactance equation (5-6) decreases for increasing frequency, which makes the current through the layer to increase. Because the NCA drives the electrodes with a constant modulation power, a higher current also means a lower voltage over the electrodes and therefore the electrical field decreases.

The roll off is probably not caused by bandwidth limitations of the MR itself, because the characteristic time for an MR to build up the optical field is equal to:

$$\tau_{cav} = \frac{FRn_g}{c} \quad (2-29)$$

With realistic values of R and n_g (150 μm and 1.5 respectively) it can be seen that for 1 GHz modulation ($\tau_{cav} < 1$ ns) the finesse can be as high as 1300 before this effect would be dominant. As can be seen from figure 5.31 the finesse in this disc is much lower.

5.3 *Photo-stability measurements*

During some of the measurements a change in the spectral and EO behaviour of the MR was witnessed. In order to find the cause of this instability a long measurement was done on the

last MR from paragraph 5.2.3, because the instability is probably caused by singlet oxygen breaking down the chromophores of the PMMA-DR1 induced by high power IR light which is coupled in the MR [Dalton.2001][[Ren.2000].

For this measurement a setup as schematically given in figure 5.35 is used.

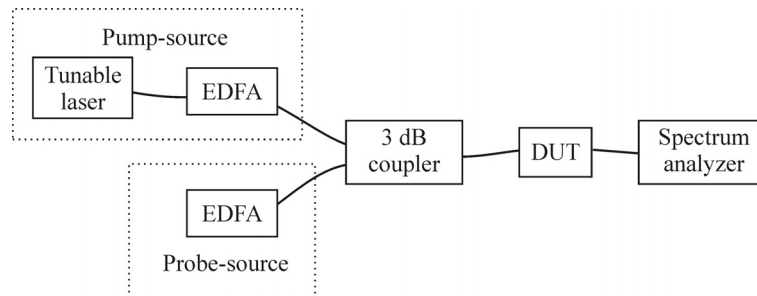


Figure 5.35: Schematic representation of the setup used for the stability measurement.

The first EDFA is used to couple a broad spectrum in the device in order to measure its spectrum (probe-source). The tunable laser is coupled to an EDFA in order to increase its optical power to approximately 10 mW in the fiber (pump-source). Its wavelength is set to a resonance wavelength of the MR (see figure 5.36).

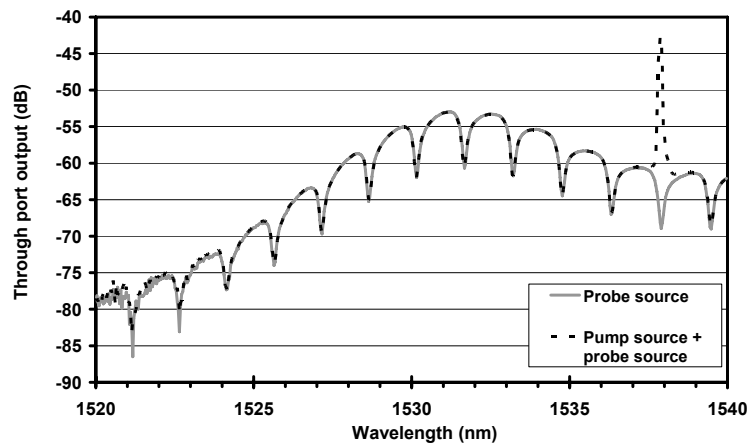


Figure 5.36: Spectrum of probe source peak compared to MR spectrum

The 10 mW from the fiber is coupled to the input waveguide by a simple butt coupling thereby losing probably somewhere between 5 or 10 dB, before the light reaches the MR (leaving 1 to 3 mW of optical power in the waveguide when approaching the MR). The coupling constants in this device are approximately 0.7-0.8, so approximately 70 to 80% of the optical power is coupled from the waveguide to the MR. The amount of optical power in the MR is therefore in the order of 1-2 mW (enhancement of the field by resonance is not

taken into account because this ring has a relatively low finesse, giving it low resonance induced field enhancement).

The spectrum is measured in a wavelength window (1540-1560 nm) just above the wavelength of the tunable laser. The MR is placed on a temperature controlled chuck and this temperature is kept stable within 0.1 °C (so the resonance wavelength is stable within approximately 15 pm).

Every 10 minutes the spectrum of the MR is measured and making a graph of these different spectra results in figure 5.37.

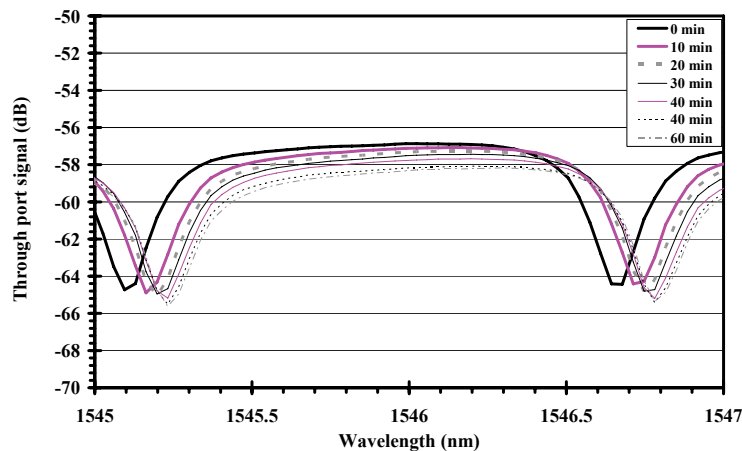


Figure 5.37: TE spectrum of a PMMA-DR1 MR with a radius of 150 μm

When looking at the position of the resonance dips it can be noticed that the position of the resonance dip shifts to a higher wavelength. This means that the effective index (and consequently the refractive index) of the MR increases. The largest increase is witnessed in the first 10 minutes and a refractive-index change of approximately $7 \cdot 10^{-6}$ /minute can be calculated with equation (2-27). The breakdown of chromophores would normally result in a decrease of the polarizability and therefore a decrease in refractive index. The measurement is done for TE polarization on a poled device. After poling the chromophores are aligned perpendicular to the electrical field of the TE polarization and therefore polarizability is low for this polarization. Probably the breakdown of chromophores in this perpendicular orientation results in degradation products with an increased polarizability for the TE polarization, and therefore an increase in the refractive index.

When the spectrum shifts, the tunable laser (pump) isn't at the resonance wavelength anymore and therefore less field is build up in the MR. The shift in wavelength will therefore level off.

To see if the effect is caused by singlet oxygen breaking down the chromophores in the PMMA-DR1, the same experiment is done again using a showerhead with nitrogen mounted over the sample. A photo of this setup is given in figure 5.38.

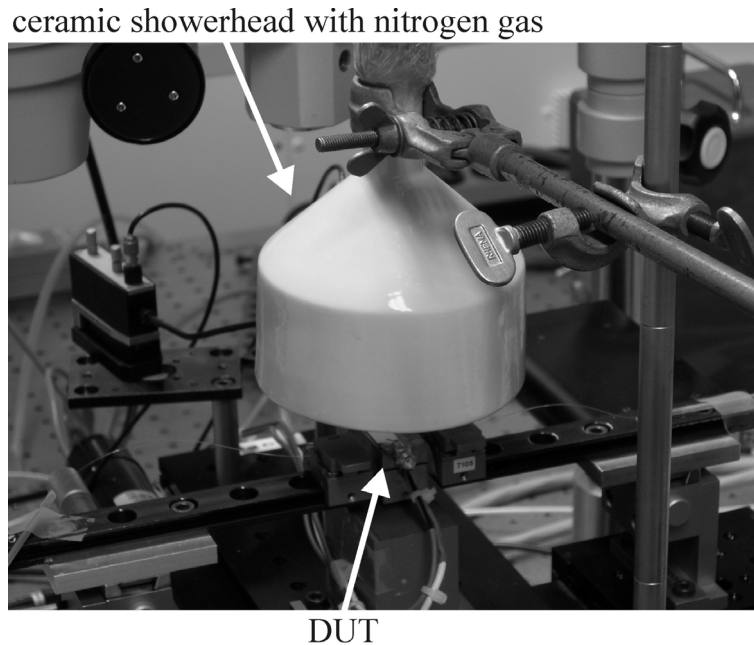


Figure 5.38: Ceramic showerhead to create a nitrogen atmosphere around the device

The different spectra of this measurement are given in figure 5.39.

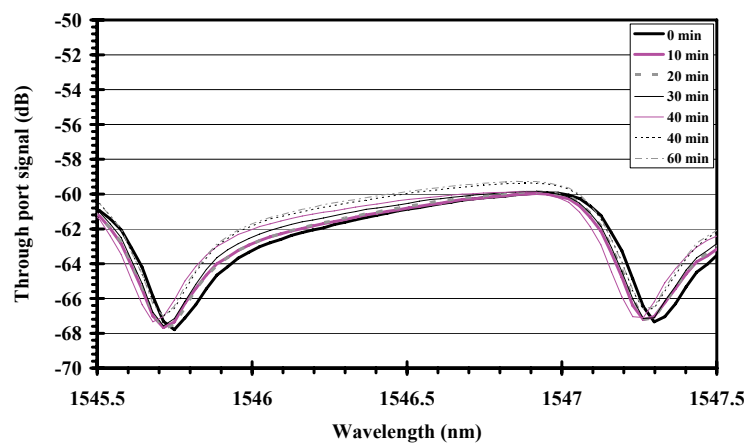


Figure 5.39: TE spectrum of a PMMA-DR1 MR with a radius of $150\ \mu\text{m}$ under nitrogen enclosure

It can clearly be seen that the drift in resonance wavelength is strongly reduced, especially when it is considered that in this measurement the tunable laser stays at the resonance wavelength and therefore a relatively large optical field is coupled to the MR continuously.

CHARACTERIZATION

When determining the resonance wavelengths of a single dip in the through port, a graph can be made to show the relation between resonance wavelength and time. This is done for both the air and nitrogen environment and shown in figure 5.40.

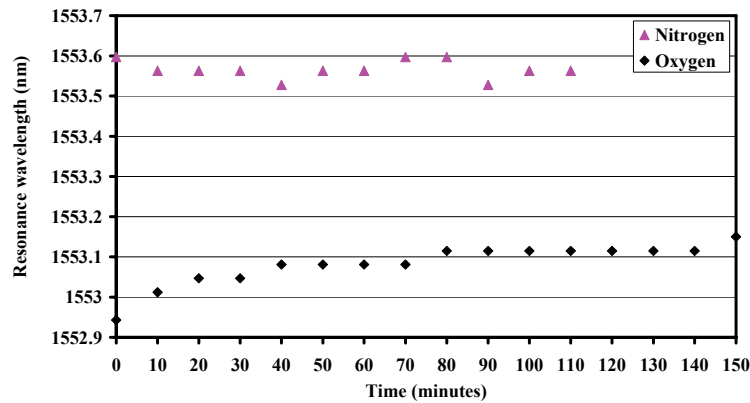


Figure 5.40: Position of the resonance wavelength vs. time for both an oxygen and nitrogen environment

From this figure the more stable behaviour of the MR in a nitrogen environment can be seen. In order to prevent the photochemical degradation of the PMMA-DR1 the sample should therefore be packaged hermetically free of oxygen.

6 Conclusions

After designing and realizing the MR structures, conclusions can be drawn and recommendations for future work can be done. This will be done for both the realization and characterization part of the thesis

Realization:

The fabrication process of polymeric MR devices was optimized, after which it was possible to stack 6 layers of polymers on top of each other without defects. Surface modifications by UV-ozone treatments were needed between some of these layers.

Waveguide definition can be done conveniently by merely lithography (without etching) by using a negative photoresist (SU8) as a waveguide layer. With this resist ridge, waveguides with ridge-heights of 300 nm are realized

Lowering of the losses in the MR can be done by placing it on a ridge of non-reflowable material and heating it up to its glass transition temperature to let it reflow. The waveguide losses were lowered from 3 dB/cm to 1 dB/cm (which are for the larger part (≈ 0.8 dB/cm) caused by material losses).

A fabrication step that should be added to the process is (oxygen free) packaging of the device in order to prevent singlet oxygen from reaching the MR. This will prevent breakdown of the chromophores.

Characterization:

From several of the realized MR devices, passive MR behaviour could be measured. Both through and drop port spectra were measured and MR loss and coupling constants could be fitted to this data. The losses were relatively high (~ 10 dB/cm) compared to the values of 1 dB/cm found for the PMMA-DR1 in a reflow-experiment. This difference is most likely caused by high losses in the Glassclad cladding-layer surrounding the MR.

The spectra of the MR could be tuned thermally (by heating the entire sample) with a shift in the resonance wavelengths of 150 pm/ $^{\circ}$ C, which corresponds to a thermo optic coefficient of $1.5 \cdot 10^{-4}/^{\circ}$ C.

CONCLUSIONS

On both the MR and the MR-MZI devices the optical signals could be modulated electro-optically with r_{33} constants which had values of 10-14 pm/V, which is close to optimal poling as can be found in literature [Liang.1994] [Michelotti.1999] [Michelotti.2003]. This optimal poling implies a layerstack with resistivities such that a large part of the electrical field is applied over the MR.

Also for the MR coupled to an MZI the spectral behaviour could be determined, in which more than one optical mode appeared to be in resonance. On a flank of one of the dips in this spectrum, the MR could be modulated electro-optically at 1 GHz. EO coefficients of 10 pm/V were found from these measurements. The modulation effect can be doubled by using the device in a push-pull configuration [Xie.2003]. An advantage of such a configuration is the symmetry in the device, which increases the thermal stability.

The most important conclusion to be drawn at the end of this thesis is that the device principle of a high speed EO polymeric MR modulator works. Modulation frequencies up to 1 GHz were demonstrated with simple lumped element electrodes. With proper modulation techniques this might result in bitrates $> 1\text{Gbit/s}$. Measurements higher than 1 GHz were not possible because of a roll-off in the frequency response of the device. Above 500 MHz the device response decreased, which was probably caused by the Glassclad layer.

Recommendations

The work for this thesis was done for two different projects (THz and NAIS). The functionality of the modulator for the NAIS project was shown by measuring 1 GHz of modulation, but the operating wavelength for the THz project is lower ($< 850\text{ nm}$) and in order to use the modulator in this project, some redesign is needed. If the structure is redesigned it is advisable to replace the Glassclad layer by a different “low” index material, which doesn't cause a roll off in the frequency response (for instance a passive polysiloxane [Sarat.1993]). Also modulation measurements at low temperatures still have to be done in order to show full functionality in the THz project.

Another issue that should be solved is the photo stability of the EO polymer. The PMMA-DR1 devices require oxygen free packaging of the entire device, which makes fabrication of the device more difficult and therefore more expensive. Substituting the PMMA-DR1 by a more stable EO polymer could solve this issue, making simple fabrication of high speed EO modulators possible. The EO polymer that replaces the PMMA-DR1 should in the ideal case also have a higher EO coefficient. A higher coefficient makes large modulation depths possible.

7 Summary

This thesis will describe the design, realization and characterization of an EO polymeric MR resonator, which was fabricated in the framework of a MESA⁺ Strategic Research Orientation TeraHertz and an IST project NAIS. The thesis is organized in the following chapters.

Chapter 1

A short introduction of the two projects for which the work of thesis was done is given, after which the device principles of two different device variations are discussed. Each of the two projects sets different demands for the structure to be realized and the difference between these two projects will be discussed briefly.

Chapter 2

In order to predict the behaviour of the EO MR modulator, the theoretical background of the device is discussed. The first part of the chapter deals with polymer related theory, in which the different properties of polymers and the basic structure of the active polymer are discussed. The second part of the chapter deals with the theoretical description of both the MR and the MR-MZI device.

Chapter 3

With the theoretical descriptions from the previous chapter, a design of the modulator was made. The first part of this chapter describes the choice for the different materials used in the device. The properties (refractive index + spincurve) of these materials are determined in this part of the chapter. The second part of the chapter deals with the dimensions of the complete device and both 2D and 3D simulations for both waveguide and MR are done. The electrode structure is designed and the different mask-layers are discussed.

Chapter 4:

The realization of the designed device is discussed in this chapter. First the different fabrication steps in the process are summarized, after which the second part of the chapter deals with different problems/issues that arose during the fabrication process. A description of

SUMMARY

each issue is given, with a solution for the problem that this issue causes. The problems are discussed in chronological order in the fabrication process.

Chapter 5

After realizing the devices, characterization is needed in order to confirm their behaviour. Different measurement techniques that were used to determine material or waveguide properties are discussed. The measurements of realized devices are discussed in the second paragraph of the chapter. First the passive MR behaviour is measured, after which from these measurements conclusions can be drawn about the dimensions and properties of it. Fitting software [RFIT] is used in order to determine the loss in the MR and the distance between MR and waveguide. Thermo optic tuning of a single MR is done by heating the entire structure and looking at the spectral shift. On these single MRs 50 MHz EO modulation is measured. On an MR device combined with an MZI, EO modulation up to 1GHz could be measured. The reason for the relatively low 50 MHz on the single MR is partly explained in the last paragraph in which photo-stability measurements are done.

Chapter 6

Conclusions regarding the fabrication and characterization process will be drawn in this chapter and also some recommendations for any future work on the subject of this thesis will be given.

Appendix

A1 MASK LAYOUT

This appendix will give a detailed description of the different lithographic masks that were used in the fabrication of the MR devices. The masks contain both MR devices and MZI with MR devices. They are divided over the mask as shown in figure A1.1.

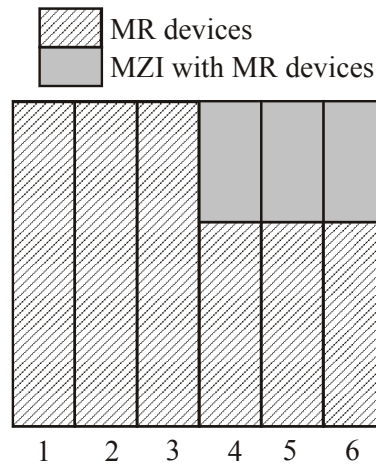


Figure A1.1: Division of mask in 6 strips with schematic position of MR and MZI with MR devices

The mask is build-up in 6 strips of devices (1-6 in figure A1.1). Strip 1-3 consist of MR devices. Strip 4-6 consist of MR and MR-MZI devices. All 4 mask-layers are shown below in one picture for strip 1 and 6 (both strips are rotated by 90°).

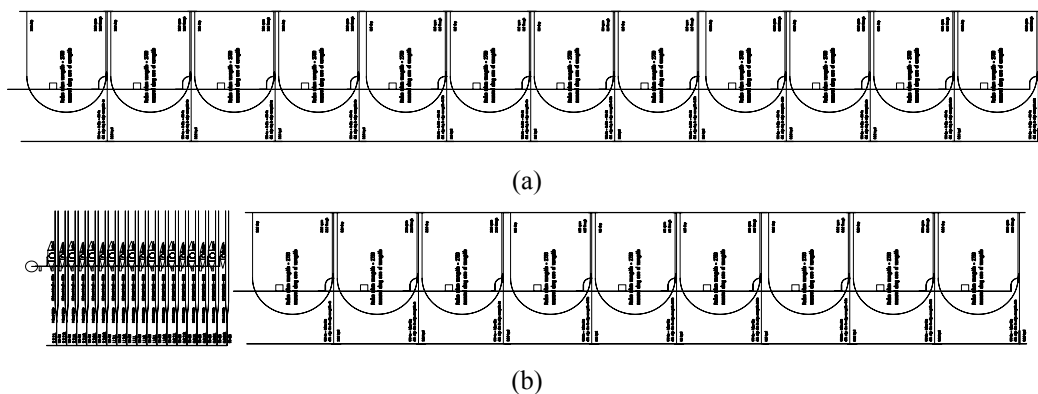


Figure A1.2: Schematic view of strip 1 and 6 (a) strip 1 rotated left 90° (b) strip 6 rotated left 90°

The 4 complete mask layers are shown in figure A1.3, in which only the alignment markers are left out. The devices are numbers from the bottom of the strip. The first device at the bottom of the strip is number 1.

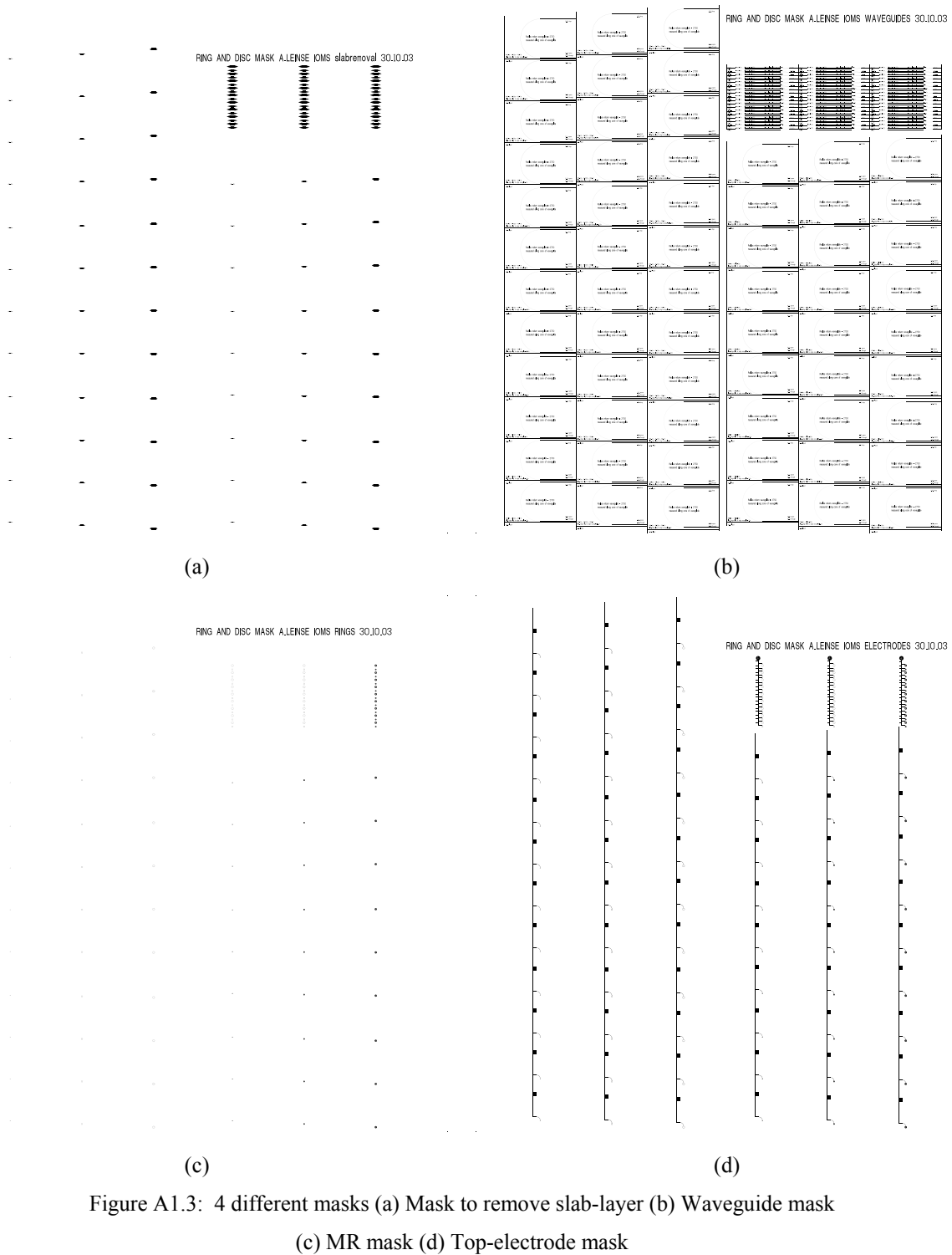


Figure A1.3: 4 different masks (a) Mask to remove slab-layer (b) Waveguide mask
(c) MR mask (d) Top-electrode mask

The design of the different dimensions on the mask was already discussed in chapter 3. In this appendix all the different dimension are summed up. The parameters are only given for the waveguide and the ring, because mask (a) and (d) are linked to these values as is discussed in chapter 3.3

For each device the different parameters are given in table A1.1. In this table the following properties are given (see also page 47)

- Radius of the MR in μm (R)
- With of the ridge in μm (rw)
- Horizontal offset between MR and waveguide in μm (x)
- Width of the MR in μm (w).

Device- number	MR	12	50	4	-1	7	100	4	-1	7	150	4	-1	7
		11	50	4	0	7	100	4	0	7	150	4	0	7
		10	50	4	1	7	100	4	1	7	150	4	1	7
		9	50	4	3	7	100	4	3	7	150	4	3	7
		8	50	3	-0.75	7	100	3	-0.75	7	150	3	-0.75	7
		7	50	3	0	7	100	3	0	7	150	3	0	7
		6	50	3	0.75	7	100	3	0.75	7	150	3	0.75	7
		5	50	3	2.25	7	100	3	2.25	7	150	3	2.25	7
		4	50	2	-0.5	7	100	2	-0.5	7	150	2	-0.5	7
		3	50	2	0	7	100	2	0	7	150	2	0	7
		2	50	2	0.5	7	100	2	0.5	7	150	2	0.5	7
		1	50	2	1.5	7	100	2	1.5	7	150	2	1.5	7
		Strip 1					Strip 2					Strip 3		
Device- number	MZI with MR	27	150	4	-1	5	150	4	-1	7	150	4	-1	disc
		26	100	4	-1	5	100	4	-1	7	100	4	-1	disc
		25	150	4	1	5	150	4	1	7	150	4	1	disc
		24	100	4	1	5	100	4	1	7	100	4	1	disc
		23	150	4	3	5	150	4	3	7	150	4	3	disc
		22	100	4	3	5	100	4	3	7	100	4	3	disc
		21	150	3	-0.75	5	150	3	-0.75	7	150	3	-0.75	disc
		20	100	3	-0.75	5	100	3	-0.75	7	100	3	-0.75	disc
		19	150	3	0.75	5	150	3	0.75	7	150	3	0.75	disc
		18	100	3	0.75	5	100	3	0.75	7	100	3	0.75	disc
	17	150	3	2.25	5	150	3	2.25	7	150	3	2.25	disc	
	16	100	3	2.25	5	100	3	2.25	7	100	3	2.25	disc	
	15	150	2	-0.5	5	150	2	-0.5	7	150	2	-0.5	disc	
	14	100	2	-0.5	5	100	2	-0.5	7	100	2	-0.5	disc	
	13	150	2	0.5	5	150	2	0.5	7	150	2	0.5	disc	
	12	100	2	0.5	5	100	2	0.5	7	100	2	0.5	disc	
	11	150	2	1.5	5	150	2	1.5	7	150	2	1.5	disc	
	10	100	2	1.5	5	100	2	1.5	7	100	2	1.5	disc	
	MR	9	50	4	-1	disc	100	4	-1	disc	150	4	-1	disc
		8	50	4	1	disc	100	4	1	disc	150	4	1	disc
7		50	4	3	disc	100	4	3	disc	150	4	3	disc	
6		50	3	-0.75	disc	100	3	-0.75	disc	150	3	-0.75	disc	
5		50	3	0.75	disc	100	3	0.75	disc	150	3	0.75	disc	
4		50	3	2.25	disc	100	3	2.25	disc	150	3	2.25	disc	
3		50	2	-0.5	disc	100	2	-0.5	disc	150	2	-0.5	disc	
2		50	2	0.5	disc	100	2	0.5	disc	150	2	0.5	disc	
1		50	2	1.5	disc	100	2	1.5	disc	150	2	1.5	disc	
Strip 4					Strip 5					Strip 6				

Table A1.1: Detailed parameters for each device in the mask series

A2 FABRICATION DETAILS

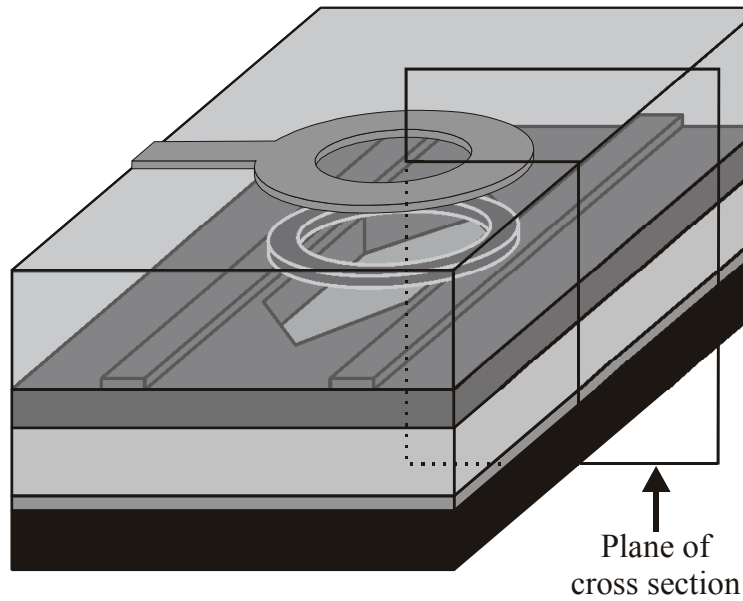







Figure A2.1: 3D schematic figure of the realized device




Substrate material				
Material	Silicon			
Diameter	100 +/- 0.5 mm			
Type	P/Boron/<100>			
Thickness	525 +/- 25 μm			
Resistance	5-10 Ωcm			
Standard wafercleaning in liquid HNO_3 10 minutes in 100% HNO_3 at 20°C and 15 minutes in 70% HNO_3 at 95°C.				
Evaporation of bottom electrode in the BAK600 Balzer.				
Layer	Thickness (nm)	Current (mA)	Rate nm/s	Pressure (mbar)
Cr	5	50	0.1	1e-6
Au	150	250	0.3	8e-7
Cr	5	50	0.1	1e-6





FABRICATION DETAILS

<p>The bufferlayer 4 μm of filtered (0.2 μm acrodisc filters) Glassclad is spincoated on the bottom electrode. The layer is spincoated in two layers with the following recipe in an environment saturated with isopropanol (this is done by placing cups of isopropanol in the spinbowl)</p> <ul style="list-style-type: none"> - Acceleration: 3000 rpm/s - Speed: 1000 rpm - Time: 30 sec. - Air dry for 1 hour - Hotplate 25°C => ramp up (2°C/min) to 150°C => dwell for 1 hour => ramp down (2°C/min) to 25°C - Apply 45 minutes of UV-ozone treatment in the UV PRS-100 Ozone reactor. - Directly after the UV-ozone treatment another layer with the same recipe as above is spincoated. 	
<p>The first layer SU8 with a thickness of 0.7 μm is spincoated on the Glassclad.</p> <ul style="list-style-type: none"> - SU8-25 from Microresist technology. - Dilute this with γ-butyrolactone (GBL) in a mass-ratio of 1:1 - Filtered with a 0.2 μm acrodisc filter and left to saturate for 1 hour. - Apply a UV-ozone treatment of 45 minutes on the Glassclad layer - Spincoat a layer of SU8 - Acceleration: 3000 rpm/ - Speed: 3500 rpm - Time: 30 sec. - Hotplate 95°C => 4 minutes - Hotplate 120°C => 2 minutes 	

<p>With a lithography process a part of this layer is removed. This is done to prevent coupling from the ring to the SU8 slablayer under the ring.</p> <ul style="list-style-type: none"> - Use the Karl Süss Mask aligner MA55 with an optical mask to define the part of the slab that should be removed. The exposure time was 20 seconds - A post exposure bake is done to crosslink the UV-cured material (hotplate 85°C => 4 minutes) - Develop in RER600 for 45 seconds - Rinse with isopropanol and spin dry - Hotplate 25°C => ramp up (2°C/min) to 120°C => dwell for 1 hour => ramp down to 25°C 	
<p>A second thin layer (0.3 µm) SU8 is spincoated.</p> <ul style="list-style-type: none"> - SU8-25 from Microresist technology. - Dilute this with γ-butyrolactone (GBL) in a mass-ratio of 1:4 (SU8:GBL) - Filtered with a 0.2 µm acrodisc filter and left to saturate for 1 hour. - Spincoat a layer of SU8 - Acceleration: 3000 rpm/s - Speed: 1100 rpm - Time: 30 sec. - Hotplate 95°C => 3 minutes - Hotplate 120°C => 3 minutes 	
<p>With a lithography process the waveguide is defined.</p> <ul style="list-style-type: none"> - Use the Karl Süss Mask aligner MA55 with an optical mask to define the ridge waveguide. The exposure time was 13 seconds - A post exposure bake is done to crosslink the UV-cured material (hotplate 85°C => 3 minutes) - Develop in RER600 for 50 seconds - Rinse with isopropanol and spin dry - Hotplate 25°C => ramp up (2°C/min) to 120°C => dwell for 1 hour => ramp down to 25°C 	

FABRICATION DETAILS

<p>The intermediate layer of Glassclad is spincoated. The thickness of the layer above the ridge should be ~ 700 nm. This was spincoated with the following recipe in an environment saturated with isopropanol</p> <ul style="list-style-type: none"> - Acceleration: 3000 rpm/s - Speed: 5000 – 6000 rpm - Time: 30 sec. - Air dry for 1 hour - Hotplate 25°C => ramp up (2°C/min) to 150°C => dwell for 1 hour => ramp down (2°C/min) to 25°C 	
<p>A layer of PMMA-DR1 is spincoated</p> <ul style="list-style-type: none"> - Dissolve the PMMA-DR1 mixture in 1,1,2-Trichlorethane (9 mass-% solution) - Filter with 0.2 μm spiralcap filter (Gelman sciences) - Apply a UV-ozone treatment of 30 minutes on the Glassclad layer - Spincoat a layer of PMMA-DR1 - Acceleration: 3000 rpm/ - Speed: 2400 rpm - Time: 30 sec. - Hotplate 25°C => ramp up (2°C/min) to 120°C => dwell for 2 hours => ramp down (2°C/min) to 25°C 	
<p>Lithography followed by reactive ion etching defines the ringresonator.</p> <ul style="list-style-type: none"> - Spincoat 907/17 resist - Acceleration: 5000 rpm/s - Speed: 4000 rpm - Time: 20 seconds - Hotplate 95°C => 1 minute - Use the Karl Süss Mask aligner MA55 with an optical mask to define the microring. The exposure time was 3.9 seconds - Hotplate 120°C => 1 minute - Develop in OPD4262 for 50 seconds - Rinse with water and spin dry - RIE (using “Elektrotech Twin system PF 340”) until 	

<p>completely etched through the resistlayer with the following parameters</p> <ul style="list-style-type: none"> - Pressure: 10 mTorr - Temperature: 10°C - Power: 50 W - SF₆ flow: 10 sccm - O₂ flow: 10 sccm - Time: 5 minutes 																			
<p>By heating the ring above its T_g the ring can be reflowed to smoothen out surface roughness [Leinse.2004]</p> <ul style="list-style-type: none"> - Hotplate 25°C => ramp up (2°C/min) to 135°C => dwell for 2 hours => ramp down (2°C/min) to 25°C 																			
<p>The topcladding of Glassclad is applied by spincoating directly after reflowing. Topcladding needs a thickness of 4 μm (above the ring). Therefore the layer is applied in two different layers with the following recipe in an environment saturated with isopropanol (this is done by placing cups of isopropanol in the spinbowl)</p> <ul style="list-style-type: none"> - Acceleration: 3000 rpm/s - Speed: 750 rpm - Time: 30 sec. - Air dry for 1 hour - Hotplate 25°C => ramp up (2°C/min) to 130°C => dwell for 2 hours => ramp down (2°C/min) to 25°C - No UV-ozone treatment to prevent exposing the PMMA-DR1 to UV too long. - Directly after taking the wafer of the hotplate another layer with the same recipe as above is spincoated. 																			
<p>A topelectrode of 150 nm gold (with 5 nm chromium as an adhesion promoter) is applied by sputtering in the “UT-Sputterke” with the following parameters (both sputtersteps with 1 minute pre sputtering).</p> <table border="1" data-bbox="217 1845 1086 2027"> <thead> <tr> <th></th> <th>Argon flow (sccm)</th> <th>Pressure (bar)</th> <th>Power (W)</th> <th>Time (m:s)</th> <th>Thickness (nm)</th> </tr> </thead> <tbody> <tr> <td>Cr</td> <td>45.0</td> <td>0.0066</td> <td>200.0</td> <td>0:30</td> <td>5.0</td> </tr> <tr> <td>Au</td> <td>45.0</td> <td>0.0066</td> <td>200.0</td> <td>4:00</td> <td>150.0</td> </tr> </tbody> </table>		Argon flow (sccm)	Pressure (bar)	Power (W)	Time (m:s)	Thickness (nm)	Cr	45.0	0.0066	200.0	0:30	5.0	Au	45.0	0.0066	200.0	4:00	150.0	
	Argon flow (sccm)	Pressure (bar)	Power (W)	Time (m:s)	Thickness (nm)														
Cr	45.0	0.0066	200.0	0:30	5.0														
Au	45.0	0.0066	200.0	4:00	150.0														

FABRICATION DETAILS


<p>The top electrode is patterned by lithography and wet etching of the gold and chromium.</p> <ul style="list-style-type: none"> - Spincoat 907/17 resist - Acceleration: 5000 rpm/s - Speed: 4000 rpm - Time: 20 seconds - Hotplate 60°C => 2 minutes - Use the Karl Süss Mask aligner MA55 with an optical mask to define the electrode structure. The exposure time was 4 seconds - Develop in OPD4262 for 45 seconds - Hotplate 60°C => 3 minutes - Etching the gold in approximately 3 minutes in a mixture (at roomtemperature) of <ul style="list-style-type: none"> - 4.5 gram I₂ - 34 gram KI - 300 gram H₂O - 150 gram glycerine - Etching the 5 nm chromium by dipping in chromium etch. - Removing the resist by applying a flood exposure of 1 minute to the resist and develop the resist in OPD 4262 	
<p>Dice the device from the wafer on the “Loadpoint Micro Ace 3”</p> <ul style="list-style-type: none"> - Apply a layer of 907/17 resist to protect the device from the coolwater during dicing - Acceleration: 5000 rpm/s - Speed: 4000 rpm - Time: 20 seconds - Flood exposure of 1 minute on the Karl Süss Mask aligner MA55 - Using an F1230 diceblade on 32000 rpm with a translation speed of 2 mm/s for dicing. - Remove the resist by developing in OPD 4262 	

Table A2.1: Detailed process-steps MR device

A3 IEE ELECTRONIC LETTERS PAPER

Scattering loss reduction in polymer waveguides by reflowing

A. Leinse, M.B.J. Diemeer and A. Driessen

A polymer channel waveguide was fabricated by reactive ion etching. Loss measurements were performed on this waveguide before and after reflowing. The waveguide loss decreases from 3 to 1 dB=cm by heating the sample slightly above the glass transition temperature of the core material. This result in channel loss is very close to the measured film losses of 0.8 dB=cm.

Introduction: For most applications in integrated optics it is very important that the optical waveguides have a loss as low as possible. A very large source of loss in a waveguide is scattering caused by surface roughness. When creating a waveguide with a reactive ion etching (RIE) process, the sidewalls of this waveguide will be rough. This roughness occurs both in organic and inorganic materials. Reducing this roughness can be done in several ways, one being reflowing by heating the material to its glass transition temperature (T_g) (surface tension will smoothen the surface). For inorganic materials this is demonstrated in [1] and [2]. In this Letter we show that this procedure can also be carried out with organic materials such as polymers. These materials have the significant benefit that they have a relatively low T_g .

Fabrication and measurements: To see the effect of reflowing on a polymer waveguide a reactive ion etched spiral waveguide is fabricated (Fig. 1).



Fig. 1 Top view (left) and cross-section (right) of fabricated spiral waveguide

The core material of the waveguide is an EO polymer consisting of (Poly)Methyl MethAcrylate ((P)MMA) with disperse red-1 sidechains (PMMADR1), synthesised by Ecole

Nationale Supérieure de Chimie de Montpellier. The polymer was a mixture of MMA and PMADR1 in a ratio of 0.57:0.43 (refractive index is 1.61 at 1550 nm). The buffer polymer is a thermally curable methylsilicone resin (Glassclad PS233) fabricated by United Chemicals Technology (refractive index is 1.41 at 1550 nm). Fabrication of the waveguide is carried out by spincoating (on silicon wafers) of the Glassclad and PMADR1 layer. Both layers are thermally cured to remove the solvents. A positive resist is spincoated on top and the spiral waveguide is defined lithographically. The waveguide is etched with a reactive ion etching process. By etching a little deeper than the thickness of the waveguide-layer into the non-reflowable buffer polymer, the waveguide is placed on a ridge which will keep the waveguide's lateral dimensions intact during reflowing [1]. The radius of the spiral waveguide varies from 1000 to 50 mm and the total length of the waveguide is 3.5 cm. For the radii in this range the bend-loss of the fabricated waveguide is close to zero in comparison to the scattering and absorption losses. SEM pictures of the cross-section of the waveguide were taken from the fabricated sample before and after reflowing (Fig. 2).

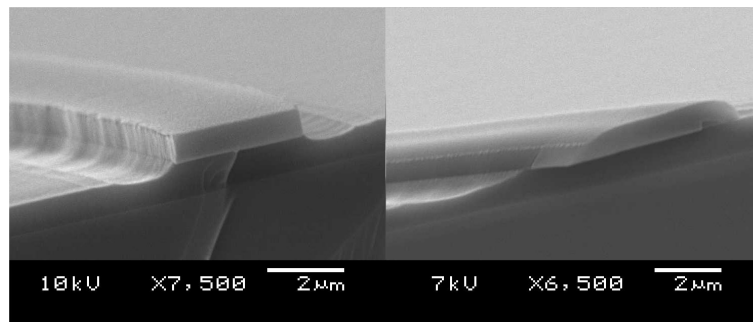


Fig. 2 Cross-section of reactive ion etched polymer waveguide before (left) and after (right) reflowing

The reflowing was carried out by heating the sample for 2 h at 135°C on a hotplate. The T_g of the PMADR1 is around 130°C. Light is coupled in the spiral waveguide with a polarisation-maintaining fibre and with a sensitive near-ir CCD camera photographs are taken from the spiral (Fig. 3). This is carried out before and after reflowing and from the pixel-intensities in these pictures the amount of scattering along the waveguide can be calculated. The photographs of a quarter of the spiral are shown in Fig. 4. By assuming that the amount of scattering is proportional to the amount of light in the waveguide, the waveguide loss can be calculated from the photographs. Fig. 5 shows the amount of scattering at different positions along the waveguide. From the slope of the lines in Fig. 5 it can be seen that the loss decreases from 3 to 1 dB=cm by reflowing of the sample. In the reflowed sample the amount

of scattering was so low that the points at the end of the waveguide (after 2 cm) could not be measured. A planar waveguide with the same thickness as the etched waveguide was fabricated and with a prism coupler setup the losses of the layer were measured. A loss of 0.8 dB=cm was obtained and therefore in the reflowed waveguide only 0.2 dB=cm can be attributed to scattering losses. This is also in agreement with the bulk losses of PMMA at 1550, which is in the order of magnitude of 0.5 dB=cm [3].

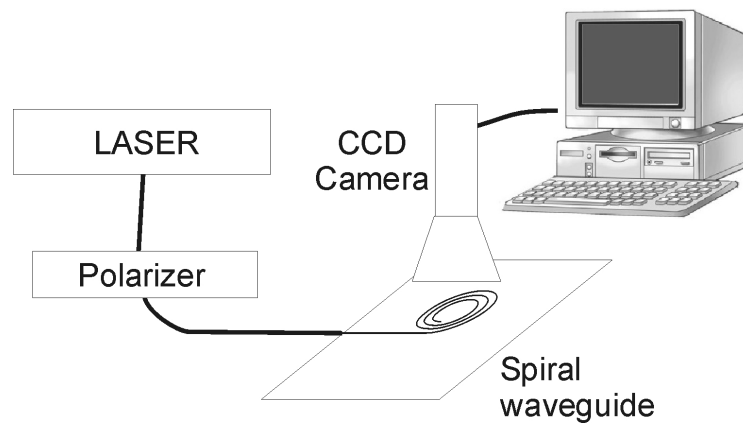


Fig. 3 Schematic view of measurement setup

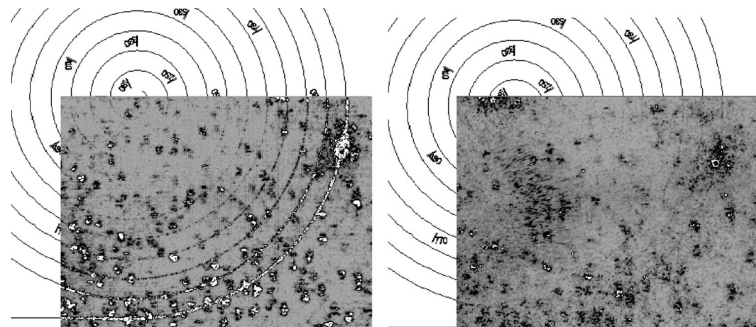


Fig. 4 Camera photographs before (left) and after (right) reflowing of spiral waveguide

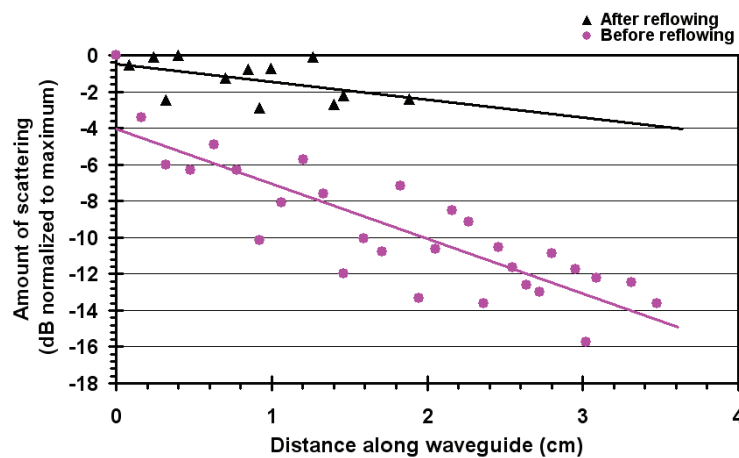


Fig. 5 Measured (and normalised to maximum) amount of scattering against distance along waveguide before and after reflowing

Conclusions: In reactive ion etched polymer waveguide channels a decrease in propagation loss was observed by simply heating the waveguide above the glass transition temperature of the core material. The waveguide definition was maintained because the waveguide was placed on a ridge of non-reflowable polymer. The decrease in loss was so great that the reflowed waveguide has losses close to the film losses.

Acknowledgments: The work was carried out in the framework of the Next Generation Active Integrated Optic Sub-systems Project IST 2000-28018 funded by the European Commission. We wish to thank R. Dekker from University Twente for the prism coupler measurements on fabricated planar waveguides, and E. Klein from University Twente for writing image processing software to calculate pixel intensities from the photographs taken.

References

- 1 Syms, R.R.A.: 'Advances in integrated optics' in Martelluci, S. (Ed.): (Plenum Press, New York, 1994), Chap. 7, p. 131
- 2 Polman, A., Min, B., Kalkman, J., Kippenberg, T.J., and Vahala, K.J.: 'Ultralow-threshold erbium-implanted toroidal microlaser on silicon', *Appl. Phys. Lett.*, 2004, 84, (7), pp. 1037–1039
- 3 Eldada, L., and Shacklette, L.W.: 'Advances in polymer integrated optics', *IEEE J. Sel. Top. Quantum Electron.*, 2000, 6, (1), pp. 54–68

© IEE 2004

2 June 2004

Electronics Letters online no: 20045654

doi: 10.1049/el:20045654

A. Leinse, M.B.J. Diemeer and A. Driessen (University of Twente, Integrated Optical MicroSystems Group, P.O. Box 217, 7500 AE,

E-mail: a.leinse@utwente.nl

A4 EQUIPMENT LIST

In the device-performance measurements discussed in this thesis the following equipment is used. The equipment is given for each different paragraph.

Paragraph	Apparatus	Type
5.1.1	Ellipsometer	Woollam M44 ellipsometer
5.1.3	CCD IR camera	Sensors unlimited inc. SU320M-1.7RT InGaAs NIR Mini Camera
	Tunable laser	Santec TSL-210
5.1.4	CCD IR camera	Sensors unlimited inc. SU320M-1.7RT InGaAs NIR Mini Camera
	Tunable laser	Hewlett Packard 8168C tunable laser source
5.2.1	Erbium Doped Fiber Amplifier (EDFA)	Nuphoton technologies NP2500 ASE EDFA
	Spectrum analyzer	ANDO 6310 AQ spectrum analyzer
5.2.2	EDFA	Nuphoton technologies NP2500 ASE EDFA
	Spectrum analyzer	ANDO 6310 AQ spectrum analyzer
	Heatable chuck	Marlow ind. Duratec high power heat pump type DT6-4-01LS
5.2.3	Tunable laser	Santec TSL-210
	High Speed InGaAs Photo-detector Module	Epitaxx ETX 100 RST
	Lock-in amplifier	Princeton applied research lock-in amplifier model 5209
	Function generator	Philips PM5193 programmable synthesizer/function generator
	Oscilloscope	Hewlett Packard 54845A Infinium Oscilloscope: 4 Channels, 1.5 GHz, up to 8 GSa/s
	Network component analyzer	HP 8702 Lightwave component analyzer
	Detector	Newport 2835C optical meter
	Heatable chuck	Marlow ind. Duratec high power heat pump type DT6-4-01LS

EQUIPMENT LIST

5.2.4	Tunable laser	Santec TSL-210
	High Speed InGaAs Photo-detector Module	Epitaxx ETX 100 RST
	Network component analyzer	HP 8702 Lightwave component analyzer
	Electrical amplifier	Minicircuit HELA-10B monolithic amplifier with a TB-17 evaluation board
5.3	Pump source	Santec TSL-210 + Firmstein technology Inc. PR25R EDFA
	Probe source	Nuphoton technologies NP2500 ASE EDFA
	Spectrum analyzer	ANDO 6310 AQ spectrum analyzer

Table A4.1: List of equipment used in characterization of materials and devices

A5 ECIO 2005 PAPER**High speed polymer e-o modulator consisting of A MZI with a micro ring resonator**

A. Leinse¹, M.B.J. Diemeer¹, A. Rousseau², A. Driessen¹

¹ Integrated Optical Micro Systems Group, MESA+ Research Institute,
University of Twente, P.O. Box 217, 7500 AE, Enschede, The Netherlands

² Ecole Nationale Supérieure de Chimie de Montpellier,
8, Rue de l'école normale F - 34296 Montpellier Cedex 5

A.Leinse@ewi.utwente.nl

SUMMARY

An integrated optical electro-optic modulator consisting of a Mach-Zehnder Interferometer with a micro ring resonator has been realized and characterized. The response measurements exhibit a 3dB roll-off at 0.5 GHz..

KEYWORDS

polymer, electro-optic, microring resonator, Mach-Zehnder Interferometer

ABSTRACT

A Mach-Zehnder interferometer with an polymer electro-optic micro-ring resonator on one of its branches is realized in a polymer layerstack and characterized. Electro-optic coefficients of 10 pm/V and modulation frequencies of 1GHz were measured.

INTRODUCTION

The role of integrated optics becomes more and more important in data communication. In order to let integrated optical components replace its electrical equivalents, active optical components are needed. A very important component is the electro-optic modulator, which is used to convert data-streams from the electrical to the optical domain. This paper deals with

the realization and characterization of such a modulator that is based on the resonance principle of a micro-ring resonator (MR) and the phase response of a Mach-Zehnder Interferometer (MZI).

DESIGN AND REALIZATION

A MR can be realized by fabricating a circular waveguide, which couples vertically to two straight port waveguides (figure 1), see, for example [1][2][3].

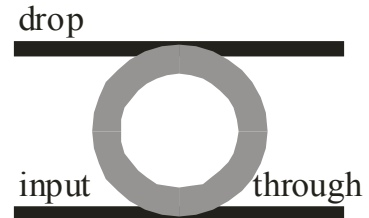


Figure 1: Schematic view of an MR with two port waveguides

By changing the optical path within the ring its resonance wavelengths can be shifted and both in the through and drop port an amplitude as well as phase modulation can be generated [1]. This change in the ring can be induced by temperature (placing a heater above the MR) or by an electric field (sandwiching the MR between two electrodes). Because of their high thermo- and electro-optic coefficients, polymers are very suitable for this type of devices. One of the problems in realizing such a device in a vertical coupling arrangement is the position of the MR relative to the two port waveguides. This position determines the amount of light that couples from the waveguides to the ring (and vice versa) at both the through and drop port side (the coupling constants). These coupling constants are critical parameters determining the spectral behaviour. Coupling the MR to a single waveguide simplifies the fabrication process because there is only one coupling constant involved. In addition, the spectral behaviour of the MR is less sensitive to changes in this single coupling constant.. In an ideal lossless ring the through port spectrum has no resonance dips because no light is coupled to the drop port waveguide. In order to use an MR coupled to a single waveguide, the phase change around a resonance wavelength can be used. Fig. 2 shows schematically the output spectrum and the phase response of a slightly lossy MR around a resonance wavelength (λ_r) [2].

This phase response can conveniently be converted to an intensity modulation by combination with an MZI. When switching between the on-resonance and off-resonance condition, the difference between the two branches of the MZI can switch from π to 0. This combination between an MR and MZI is

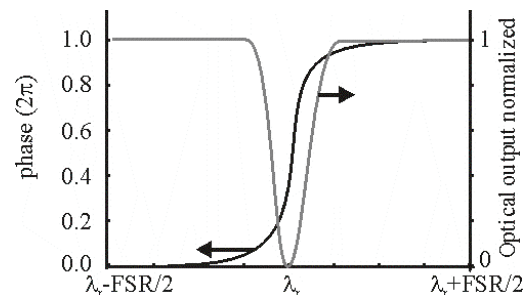


Figure 2: Output power and phase response of the through port waveguide around a resonance wavelength

shown (including a cross section through MR and waveguides) in figure 3. The passive behaviour of such is device is described by [4].

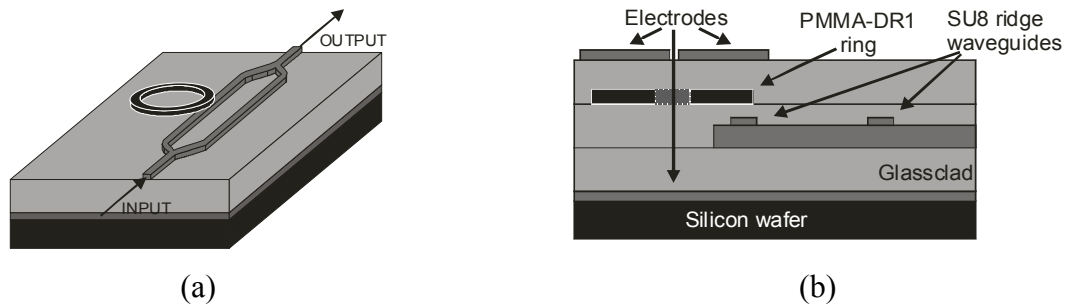


Figure 3: A MZI+ring device: (a) 3D image(b) cross section through MR and waveguides

The complete device is fabricated in a polymer layerstack, which can be deposited by spin-coating. The material used for the 2 μm wide ridge waveguides is the negative photoresist SU8. The ridges have a height of approximately 300 nm. The ridge waveguides can be defined in a two step lithographic process without any additional etching-step. The MR (with a radius of 150 μm) is fabricated in the nonlinear polymer PMMA-DR1 (synthesized by Ecole Nationale Supérieure de Chimie de Montpellier within the IST project NAIS). The MR is defined by lithography followed by reactive ion etching. Both, the MR and the ridge waveguides, are surrounded by a methyl-silicone resin (sold under the name PS233 Glassclad by United Chemical Technologies). The splitter and combiner in the MZI are fabricated by making two y-junctions in the single mode waveguide. The fabrication process is shown in figure 4 in some detail.

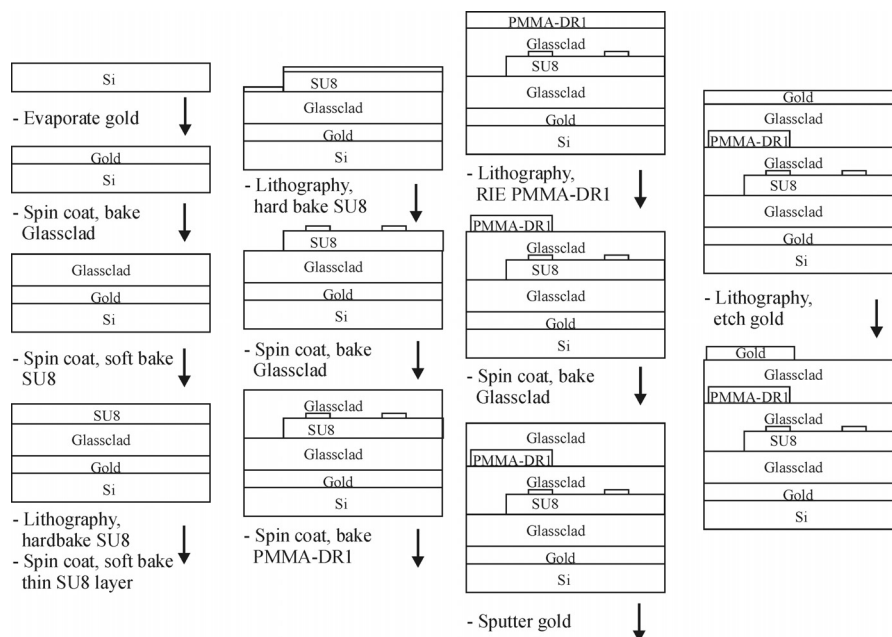


Figure 4: Fabrication process for vertical stacked MR and MZI

The part of the SU8 layer under the MR is removed lithographically in order to prevent coupling of light from the MR to this layer. Coupling to this layer would induce additional optical loss in the MR. Fabricating a balanced MZI is relatively easy when applying a heater over one of the branches. This branch can be tuned, such that both branches have the desired optical path length difference.

CHARACTERIZATION

While coupling in light at the input waveguide, the spectrum can be measured at the output waveguide. For the TE mode this spectrum shows two sets of resonance lines originating by two resonator modes, see figure 5. When using the MR as a modulator, this does not

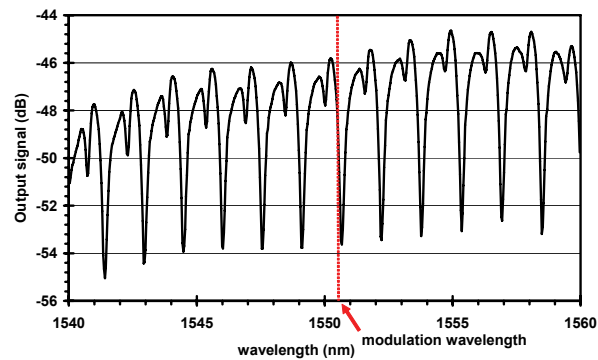


Figure 5: Measured Spectrum (TE) of the MR-MZI device. The vertical line is the wavelength of the CW tunable laser at which modulation was measured

matter because a single input wavelength (on a flank of one of the steep dips) is chosen as a modulation wavelength. With an electrode above and below the MR an electric field is applied over the MR changing its refractive index. Only the shift in the position of this single dip is of influence on the output.

While applying a modulating voltage between top and bottom electrode, the amount of optical modulation is measured. Because the slope of the spectrum around the modulation wavelength is known, the induced wavelength shift of the spectrum can be calculated for a certain modulation ripple. From this wavelength shift, the change in the refractive index of the MR-material can be calculated and with the electric field applied known, the electro-optic coefficient is determined. The r_{33} value found for this device is approximately 10 pm/V, which is in accordance to the values found in literature [5]. The electrode structure used is a lumped element structure because the length of the electrodes above such an MR can be small. A rule of thumb in RF design states that an electrode can be used as a lumped element as long as its length is smaller than 10% of the wavelength of the electrical driving field. Even for electrode structures of 1 cm in length this corresponds to an electrical frequency as high as

2 GHz. The electrode size can even be reduced to the size of the MR, making frequencies of 60 GHz possible without special RF electrode design.

The frequency of the applied modulation voltage is changed by a network component analyzer (NCA) and the modulation depth as a function of the electrical frequency is determined. These measurements were done with and without an electrical amplifier between the NCA and the electrode. This amplifier is used to increase the limited voltage applied by the NCA. The setup is schematically shown in figure 6.

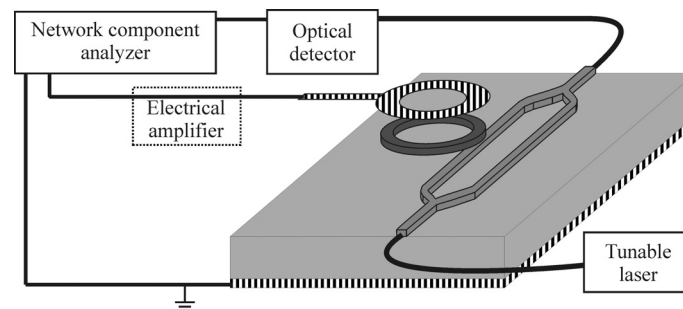


Figure 6: Schematic representation of the used measurement setup

The detector used had a spectral response which started to decay around 1 GHz. This spectral response was measured and the measured device response was corrected for this response. The different measurements done are shown in figure 7.

In figure 7 four lines are shown. These lines are:

1. Measured frequency response of the device without electrical amplification and detector correction
2. Measured frequency response of the device with electrical amplification and without detector correction
3. Measured frequency response of the device with electrical amplification and with detector correction
4. The noise signal of the detector (with the laser power off)

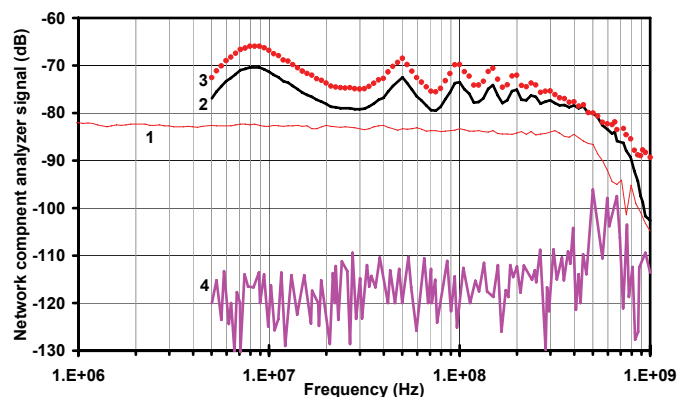


Figure 7: Measured frequency spectrum of the MR MZI device

In lines 2 and 3 a modulation can be seen with a periodicity of 50 MHz. This is probably caused by the amplifier which gets reflections from the electrodes back. This modulation is not caused by the device because in line 1 the frequency response is flat. It can be seen that modulation frequencies up to 1 GHz can be measured. With this performance, data-rates exceeding 1 Gbit/s can be transmitted. With some specific modulation techniques (like for instance quadrature amplitude modulation), data-rates of 2 to 3 Gbit/s will be possible. The roll-off above 500 MHz is caused by the layerstack. The effective current through this layerstack is dependent on $1/\omega C$ in which ω is the electrical frequency and C is the capacitance of the layerstack. Increasing the frequency results in an increase in the current through the layerstack. Because the NCA drives the electrodes with a constant modulation power, a higher current also means a lower voltage over the electrodes and therefore the electrical field decreases.

The roll off is certainly not caused by bandwidth limitations of the MR, because the characteristic time for an MR to build up the optical field is equal to:

$$\tau_{cav} = \frac{FRn_g}{c} \quad (1)$$

In which F is the finesse of the MR, R the radius, n_g the group index of the mode in the MR and c the speed of light in vacuum. With realistic values of R and n_g (150 μm and 1.5) it can be seen that for 1 GHz modulation ($\tau_{cav} < 1$ ns) the finesse can be as high as 1300 before this effect would be dominant. As can be seen from figure 5 the finesse in our ring is much lower (about 10).

CONCLUSION

A polymer electro-optic MR resonator has been fabricated and characterized. By coupling the MR with one of the branches of the MZI a modulator with larger fabrication tolerances than a standard MR is realized. With a NCA the frequency behaviour of the modulator was measured up to 1GHz with an electro-optic coefficient (r_{33}) of 10 pm/V.

REFERENCES

- 1) Rabiei P, Steier WH, Cheng Zhang, Dalton LR. 'Polymer Micro-Ring filters and modulators', Journal of lightwave technology, vol.20, n°11, p1968-1975, November 2002.
- 2) Blair S, Heebner JE, Boyd RW. 'Beyond the absorption limited nonlinear phase shift with microring resonators', Optics Letters, vol 27, n°5, p357-359, March 2002

- 3) A. Leinse, A. Driessen, M.B.J. Diemeer, 'Electro-optical modulation in a polymer ring resonator', 39th Course Microringresonators as building blocks for VLSI photonics, International School of Quantum Electronics , October 2003, Erice, Sicily
- 4) Absil PP; Hryniewicz JV; Little BE; Wilson RA; Joneckis LG; Ho PT, 'Compact microring notch filters', IEEE Photonics Technology Letters, vol 12, n° 4, p 398-400, April 2000
- 5) Nagtegaele P, Brasselet E, Zyss J., 'Anisotropy and dispersion of a Pockels tensor: a benchmark for electro-optic organic thin-film assessment', Journal of the Optical Society of America B , vol 20, n° 9, Sept. 2003, p 1932-6

AKNOWLEDGEMENT

The work presented was done within the frame work of the IST project NAIS and the MESA+ Strategic Research Orientation "TeraHertz Signal Processing"

References

- [Anderson.1964] J.C. Anderson, *Dielectrics*, Chapman and Hall, London, 1964, ASIN: B0006BXOZ6
- [Alkeskjold.2004] T.T. Alkeskjold, J. Lægsgaard, A. Bjarklev, *All-optical modulation in dye-doped nematic liquid crystal photonic bandgap fibers*, *Optics express*, vol 12. no 24, 2004, p. 5857-5871
- [Asperen.2003] S.A. van Asperen, *High speed and low power electro-optic polymer modulator based on a mode converter (grating)*, M.Sc. Thesis, Integrated Optical Micro Systems group, University of Twente, the Netherlands, 2003
- [ATR] ATRguide, mode solver software developed by the Integrated Optical Micro Systems group of the University of Twente
- [Azzam.1977] R.M.A. Azzam, N.M. Bashara, *Ellipsometry and polarized light*, North-Holland Publishing Co., Amsterdam 1977, p. 283, ISBN: 0720406943
- [Bauer.1996] S. Bauer, *Poled polymers for sensors and photonic applications*, *Journal of Applied Physics*, vol 80 (10), 15, 1996, p. 5531-5557
- [Blom.1998] F.C. Blom, *Linear and non-linear optical properties of cylindrical micro-resonators: from material to device realisation*, Phd Thesis, Integrated Optical Micro Systems group, University of Twente, the Netherlands, 1998

REFERENCES

- [Bradshaw.1997] R.D. Bradshaw, L.C. Brinson, *Physical aging in polymers and polymer composites: an analysis and method for time-aging time superposition*, Polymer Engineering and Science, vol. 37, no. 1, 1997, p. 31-44
- [Chen.2004] W.Y. Chen, R. Grover, T. A. Ibrahim, V. Van, W. N. Herman, P.T. Ho, *High-Finesse Laterally Coupled Single-Mode Benzocyclobutene Microring Resonators*, IEEE Photonics Technology Letters, vol. 16, no. 2, 2004, p. 470-472
- [C2V] TempSelene and Olympios, commercial products of C2V, Colosseum 20, 7521 PT Enschede, The Netherlands
- [Couch.1993] L.W. Couch, "Digital and analog communication systems", Prentice-Hall New Jersey, 1993, ISBN: 0135225833
- [Dalton.2001] L.R. Dalton, *Realization of sub 1V polymeric EO modulators through systematic definition of material structure/function relationships*, Synthetic Metals, vol. 124, 2001, p. 3-7
- [Diemeer.1990] M.B.J. Diemeer, F.M.M. Suyten, E.S. Trommel, A. McDonald, J.M. Copeland, L.W. Jenneskens, W.H.G. Horsthuis, *Photoinduced channel waveguide formation in nonlinear optical polymers*, Electronics Letters, vol. 26, no. 6, 1990, p. 379-80
- [Diemeer.1998] M.B.J. Diemeer, *Polymeric thermo-optic space switches for optical communications*, Optical Materials, vol. 9, 1998, p. 192-200.
- [Diemeer.2003] M.B.J. Diemeer, *Polymeric components for optical communications*, Phd Thesis, Integrated Optical Micro Systems group, University of Twente, the Netherlands, 2003
- [Diemeer.2004] M.B.J. Diemeer, *Organic and Inorganic glasses for microring resonators*, Microresonators as building blocks for VLSI photonics:

-
- International school of quantum electronics, 39th Course (18-25 October 2003), American Institute of physics, 2004, p. 252-267
- [Doi.1988] M .Doi, S.F. Edwards, *The theory of polymer dynamics*, International series of monographs on physics, Oxford: Clarendon Press, 1 ed., 1988, ISBN: 0198520336
- [Firestone.1995] M.A. Firestone, M.A. Ratner, T.J. Marks, *Electric field poling in polymeric nonlinear optical materials. Relaxation Dynamics, Model, and Experiment*, *Macromolecules*, vol. 28, 1995, p. 6296-6310
- [Geuzebroek.2005] D.H. Geuzebroek, A. Driessen, *Wavelength Filters for Fibre Optics*, chapter 9, editor H. Venghaus, Springer-Verlag, published medeo 2005
- [Gonzalez.2000] A.G. Gonzalez, M. Canva, G.I. Stegeman, *Systematic behaviour of electro-optic chromophore photostability*, *Optics Letters*, vol. 25, no. 5, p. 332-334
- [Gunter.2000] P. Günter, *Nonlinear optical effects and materials*, Springer Berlin, 2000, ISBN: 3540650296
- [Havinga.1979] E.E. Havinga, P. van Pelt, *Electrochromism of substituted polyalkenens in polymer matrices: Influence of chain length on charge transfer*, *Berichte der Bunsen-Gesellschaft : physical chemistry*. vol. 83, 1979, p. 816-821
- [Hornak.1992] L.A. Hornak, *Polymers for lightwave and integrated optics: technology and applications*, New York, Marcel Dekker inc., 1992, ISBN: 0824786971
- [Horowitz.2001] F. Horowitz, M.B. Pereira, P. Alcantara, H.P. Greineisen, V. Stefani, *Optical properties of organic-chromophore doped sol-gel coatings: poling-induces birefringence*, *Journal of Non-crystalline solids* vol. 284, 2001, p. 183-187

REFERENCES

- [Johnson. 1993] H.W. Johnson, M. Graham, "High speed digital design", Prentice Hall Inc., New Jersey 1993, ISBN: 0133957241
- [Klein.2002] E.J. Klein, *Wavelength selective switching using thermally tunable microring resonators*, M.Sc. Thesis, Integrated Optical Micro Systems group, University of Twente, the Netherlands, 2002
- [Klunder.2000] D.J.W. Klunder, F.S. Tan, T. van de Veen, H.F. Bulthuis, H.J.W.M. Hoekstra, A. Driessen, *Design and Characterization of waveguide coupled cylindrical microring resonators in Si₃N₄*, IEEE LEOS 2000 conference proceedings, Rio Grande Puerto Rico, 2000, p. 758-759
- [Klunder.2002] D.J.W. Klunder, *Photon physics in integrated optics microresonators*, Phd Thesis, Integrated Optical Micro Systems group, University of Twente, the Netherlands, 2002
- [Leinse.2003] A. Leinse, A. Driessen, M.B.J. Diemeer, *Fabrication of an Electro Optic Polymer Ringresonator*, 8th Annual Symposium IEEE/LEOS Benelux Chapter, November 20-21, 2003 University of Twente, Enschede, The Netherlands, p. 201-204, ISBN: 90-365-1990-X.
- [Leinse.2004] A.Leinse, M.B.J. Diemeer, A. Driessen, *Scattering loss reduction in polymer waveguides by reflowing*, IEE Electronics letters, vol. 40 no.16, 2004, p. 992-993
- [Leinse.2005] A. Leinse, M.B.J. Diemeer, A. Rousseau, A. Driessen, *High speed polymer e-o modulator consisting of a MZI with a micro ring resonator*, ECIO'05, 12th European conference on integrated optics, 6-8 April 2005, Grenoble, France.....(accepted)
- [Liang.1994] J. Liang, R. Levenson, C. Rossier, E. Toussaere, J. Zyss, A. Rousseau, B. Boutevin, F. Foll, D. Bosc, *Thermally stable cross-linked polymers*

-
- for electro-optic applications*, Journal de physique III, no. 12, 1994, p. 2441-2450
- [Little.1998] B.E. Little, S.T. Chu, H.A. Haus, *Track changing by use of the phase response of microspheres and resonators*, Optics Letters, vol. 23, no. 12, 1998, p. 894-896
- [Lorrain.1988] P.Lorrain, D.R. Corson, F. Lorrain, *Electromagnetic fields and waves*, W.H. Freeman and company New York, 1988, ISBN: 0716718235
- [LSPEC] LSPEC, Non-commercial image processing software by E.J. Klein, Integrated Optical Micro Systems group, University of Twente, the Netherlands
- [Madsen.1999] C.K. Madsen, J.H. Zhao, *Optical filter design and analysis*, John Wiley & sons inc., New York, 1999, ISBN: 0471183733
- [Michelotti.1999] F. Michelotti, G. Nicolao, F. Tesi, M. Bertolotti, *On the measurement of the electro-optic properties of poled side-chain copolymer films with a modified Teng-Man technique*, Chemical Physics, vol. 245, 1999, p. 311-326
- [Michelotti.2003] F. Michelotti, A. Belardini, M.C. Larciprete, M. Bertolotti, A. Rousseau, A. Ratsimihety, G. Schoer, J. Mueller, *Measurement of the electro-optic properties of poled polymers at $\lambda=1.55 \mu\text{m}$ by means of sandwich structures with zinc oxide transparent electrode*, Applied Physics Letters, vol. 83, no. 22, 2003, p. 4477-4479
- [Mittal.1996] K.L. Mittal, *Polymer surface modifications: relevance to adhesion*, VSP Utrecht the Netherlands, 1996, ISBN: 9067642010
- [MRT.SU8] Micro resist technology, *Product information negative tone photoresist mr-L 6000.5XP*, Köpinger Strasse 325, Haus 211, D-12555 Berlin, Germany

REFERENCES

- [Mulder.2004] M. Mulder, *Design and realization of a hybrid electro-optic microring resonator*, M.Sc. Thesis, Integrated Optical Micro Systems group, University of Twente, the Netherlands, 2004
- [Musa.2003] S. Musa, *Polymeric multimode optical planar waveguide devices for short-distance communication*, Phd Thesis, Integrated Optical Micro Systems group, University of Twente, the Netherlands, 2003
- [Okamoto.2000] K. Okamoto, *Fundamentals of optical waveguides*, Academic press, San Diego, 2000, ISBN: 0125250959
- [Peeling.1983] J. Peeling, D.T. Clark, *Surface ozonation and photooxidation of polyethylene film*, Journal of polymer science, vol. 21, 1983, p. 2047-2055
- [Rabiei.2002] P. Rabiei, W.H. Steier, Cheng Zhang; L.R. Dalton, *Polymer micro-ring filters and modulators*, Journal of Lightwave Technology, vol. 20, no. 11, 2002, p. 1968-75
- [Ren.2000] Y. Ren, M. Szablewski, G.H. Cross, *Waveguide photodegradation of nonlinear optical organic chromophores in polymeric films*, Applied optics, vol. 39, no. 15, 2000, p. 2499-2506
- [RFIT] RFIT, Non-commercial MicroRing fit software by E.J. Klein, Integrated Optical Micro Systems group, University of Twente, the Netherlands
- [Roeloffzen.2002] C.G.H. Roeloffzen, *Passband flattened binary-tree structured add-drop multiplexers using sion waveguide technology*, Phd Thesis, Integrated Optical Micro Systems group, University of Twente, the Netherlands, 2002

-
- [Sarat.1993] S.K. Mohapatra, C.V. Francis, "Microwave loss in nonlinear optical polymers", *Journal of applied physics*, vol. 73, no. 5, 1993, p. 2569-2571
- [Sauter.1996] E.G. Sauter, *Nonlinear optics*, John Wiley & Sons Inc., New York, 1996, ISBN: 0471148601
- [Schuurman.2001] G. Schuurman, *Design, realization, and operation of a pigtailed electro-optic polymer-based Mach-Zehnder interferometer at cryogenic temperatures*, M.Sc. Thesis, Integrated Optical Micro Systems group, University of Twente, the Netherlands, 2001
- [Sekkat.1994] Z. Sekkat, W. Knoll, *Stationary state and dynamics of birefringence and nonlinear optical properties induced by electric field poling in polymeric films*, *An international journal of physical chemistry: Berichte der Bunsen-Gesellschaft*, vol. 98, no. 10, 1994, p. 1231-1242
- [Serat.2001] S. Serat, A.Kovalev, A. Agashkov, H.F.Gleeson, S.J.Watson, V. Reshetnyak, O. Yaroshchuk, *Laser-induced surface and bulk reorientation of the director in azo-dye-doped liquid crystal cells*, *Optics communications*, vol. 187, 2001, p. 235-247
- [Singer.1987] K.D. Singer, M.G. Kuzyk, J.E. Sohn, *Second-order nonlinear-optical processes in orientationally ordered materials: Relationship between molecular and macroscopic properties*, *Journal of the Optical Society of America B (Optical Physics)*, vol. 4, no. 6, 1987, p. 968-76
- [Skumanich.1993] A. Skumanich, M. Jurich, J.D. Swalen, *Absorption and scattering in nonlinear optical polymeric systems*, *Applied Physics Letters*, vol. 62 (5), 1993, p. 446-448
- [Teng.1995] C.C. Teng, M.A. Mortazavi, G.K. Boudoughian, *Origin of the poling induced optical loss in a nonlinear polymeric waveguide*, *Applied Physics letters*, vol. 66 (6), 1995, p. 667-669

REFERENCES

- [Vegt.1994] A.K. van der Vegt, *Polymeren van keten tot kunststof*, Delft, Deftse uitgevers maatschappij, 1994, ISBN: 9040723885
- [Verdeyen.1981] J.T. Verdeyen, *Laser electronics*, third edition, Prentice Hall, New Jersey 1981, ISBN: 013706666X
- [Yariv.1975] A.Yariv, *Quantum electronics*, John Wiley and Sons, New York, 1989, ISBN: 0471609978
- [Waxler.1979] R.M. Waxler, D. Horowitz, A. Feldman, *Optical and physical parameters of plexiglass55 and lexan*, Applied Optics, vol. 18, no. 1, 1979, p. 101-104
- [Wicks.1998] Z.W. Wicks, *Organic coatings: science and technology*, 2nd. edition, Wiley interscience publication,1998, ISBN: 0471245070
- [Xie.2003] X. Xie, J. Khurgin, J. Kang, F.S. Chow, *Linearized Mach-Zehnder intensity modulator*, IEEE Photonics Technology Letters, vol. 15, no. 4, 2003, p. 531-533

Samenvatting (Dutch)

Deze samenvatting is een bewerking van hoofdstuk 7 (summary). In dit proefschrift wordt het ontwerp, de realisatie en de karakterisering van een polymeren Electro Optische (EO) Microring Resonator (MR) modulator behandeld. Deze modulator is gefabriceerd in het kader van het MESA⁺ speerpunt TeraHertz en het IST project NAIS. Het proefschrift is in de volgende hoofdstukken onderverdeeld.

Hoofdstuk 1 ‘**introduction**’:

In dit hoofdstuk wordt een korte introductie van de betrokken twee projecten gegeven. Ieder project stelt andere randvoorwaarden aan de te realiseren modulator en deze verschillende randvoorwaarden worden hier besproken, waarna een aantal keuzes wordt gemaakt met betrekking tot deze randvoorwaarden. Tevens worden er twee verschillende modulatoren behandeld, welke de MR als gemeenschappelijk element hebben.

Hoofdstuk 2 ‘**theory**’:

Om het gedrag van de EO MR te kunnen voorspellen en de modulator te kunnen ontwerpen is een stuk theorie nodig. Dit hoofdstuk beschrijft deze theorie en is grofweg opgedeeld in twee delen. Het eerste deel behandelt de verschillende eigenschappen van de gebruikte (niet-lineaire) polymeren. Het tweede deel van het hoofdstuk behandelt de theoretische beschrijving van zowel de MR als de MR-MZI.

Hoofdstuk 3 ‘**design**’:

Nadat de noodzakelijke theorie in het vorige hoofdstuk is besproken, wordt er in dit hoofdstuk een ontwerp van de modulator gemaakt. Het eerste deel van het hoofdstuk beschrijft de keuze van de verschillende materialen die gebruikt zijn. De brekingsindex en de spincurve van ieder materiaal worden bepaald in dit deel van het hoofdstuk. In het tweede deel van het hoofdstuk worden de verschillende afmetingen van de modulator ontworpen. Zowel 2D als 3D simulaties zijn uitgevoerd voor zowel de golfgeleider als de MR. De elektrodestructuur is ontworpen en de verschillende maskers, welke noodzakelijk zijn voor het lithografische proces, worden besproken.

Hoofdstuk 4 ‘**realization**’:

Nadat in het vorige hoofdstuk de EO modulator ontworpen is, moet deze natuurlijk ook nog gerealiseerd worden. Deze realisatie wordt in dit hoofdstuk beschreven. In het eerste deel worden de verschillende fabricagestappen opgesomd, waarna de verschillende problemen die in deze stappen aan het licht kwamen verder worden uitgediept (en opgelost) in de rest van het hoofdstuk. De verschillende problemen worden chronologisch in het fabricageproces behandeld.

Hoofdstuk 5 ‘**characterization**’:

Dit hoofdstuk is misschien wel het belangrijkste van het hele proefschrift. Nadat de modulatoren gerealiseerd zijn, moet worden geverifieerd of hun gedrag ook is zoals verwacht. Allereerst worden de verschillende technieken om de eigenschappen van zowel de materialen als de golfgeleiders te bepalen besproken. Het tweede deel van het hoofdstuk gaat over de metingen die zijn uitgevoerd aan compleet gerealiseerde MR modulatoren. De eerste metingen die besproken worden zijn passieve MR metingen. Aan de hand van deze metingen kunnen conclusies worden getrokken over de afmetingen en eigenschappen van de MR. Met behulp van software [RFIT] is een theoretisch model gefit aan de gemeten waarden, wat is gedaan om de verliezen in de MR en de afstand tussen de MR en de golfgeleider te kunnen bepalen. Vervolgens zijn er ook thermo-optische metingen gedaan, waarbij het spectrum van een MR is gemeten terwijl hij werd opgewarmd. Met sommige van deze MR modulatoren was het mogelijk om EO modulatie met een frequentie van 50 MHz te meten. Ook met een MR-MZI modulator zijn metingen uitgevoerd en EO modulatie van 1 GHz was meetbaar. De laatste paragraaf verklaart waarom er na de 50 MHz metingen aan de MR niet nog meer metingen te doen waren. Deze paragraaf behandelt de optische stabiliteit van de MR.

Hoofdstuk 6 ‘**conclusions**’:

In dit hoofdstuk worden aan het eind van het proefschrift een aantal conclusies getrokken en ook een aantal aanbevelingen voor eventueel toekomstig werk gedaan.

Dankwoord (Dutch)

De titel van dit hoofdstuk had wellicht beter introductie kunnen zijn, aangezien 9 van de 10 die dit proefschrift in de hand krijgen toch hier beginnen. Na 9 ½ jaar op de UT is het in dit hoofdstuk tijd geworden voor het bedanken van iedereen die hier (constructief) aan heeft bijgedragen (oftewel.....waarschijnlijk iedereen die dit leest).

Dames en heren..... Bedankt..... Het was mooi.....

Waarschijnlijk vinden nu een heleboel mensen dit toch iets te onpersoonlijk.

Voor al diegene volgt hieronder een uitgebreide uiteenzetting, waarvan de volgorde bijna geheel willekeurig is.

Natuurlijk wil ik beginnen met het bedanken van mijn promotor Alfred Driessen. Hij had meestal erg nuttige op-/aanmerkingen, welke door mij wel eens pas later erkend werden (dit heeft vast niet aan mijn eigenwijsheid gelegen....toch?). Ook mijn assistent-promotor Mart Diemeer wil ik natuurlijk hartelijk bedanken voor het mij voorzien van informatie en nieuwe polymeren (beter bekend als de bekende sapjes).

De rest van mijn promotiecommissie: dhr. van Bochove, dhr. Koonen, dhr. Popma, dhr. Subramaniam en dhr. Mouthaan wil ik natuurlijk ook hartelijk bedanken voor het zitting nemen in de commissie.

Natuurlijk mogen ook de collega's niet ontbreken in dit dankwoord. In het bijzonder Anton Hollink en Henk van Wolferen, bij wie ik regelmatig met allerlei soft-/hardware problemen terecht kon. Ook Edwin Klein en Ronald Dekker wil ik hartelijk bedanken voor het programmeren van menig handig tooltje om het werk een stuk eenvoudiger te maken. Verder wil ik mijn kamergenoten Douwe Geuzebroek, Henry Kelderman, Freddy Tan, Murali Balakrishnan, Henri Uranus en Marcel Hoekman natuurlijk even apart bedanken voor hun soms zinnige, maar meestal rake opmerkingen.

De rest van de (ex)IOMS-ers, bestaande uit Markus Pollnau, Paul Lambeck, Hugo Hoekstra, René de Ridder, Kerstin Wörhoff, Rita ter Weele, Cazimir Bostan, Geert (is je boekje al af?) Altena, Joris van Lith, Wico Hopman, Gamar Hussein, Didit Yudistira, Webin Hu, Remco Nieuwland, Wouter Engbers, Shankar Selvaraja, Lucie Hilderink, Meindert Dijkstra, Robert

DANKWOORD

Wijn, Gabriel Sengo, Chris Roeloffzen, Dion Klunder en Sami Musa wil ik natuurlijk ook bedanken. Verder wil ik Stef van Asperen en Maarten Mulder bedanken omdat zij het aandurfd en om onder mijn begeleiding hun afstudeeropdracht bij IOMS te doen.

Raymond en Rob wil ik natuurlijk ook even bedanken. Niet zo zeer voor iets vakinhoudelijks, maar eigenlijk meer voor.....ja, waar bedank je je vrienden eigenlijk allemaal voor? Voor veel, maar dat is lastig om hier allemaal op te noemen. Jongens bedankt.

Zo bijna aan het eind van mijn promotie wil ik ook mijn ouders nog even bedanken, dankzij wie ik mijn studie aan de UT kunnen volgen. Toen niet gedacht dat ik er 9 ½ jaar later nog zou zitten.

En het laatste (en inderdaad meest belangrijke) bedankje is natuurlijk voor Marjoke. Ik kan namelijk een heleboel mensen bedanken, maar er is er eigenlijk maar één echt belangrijk.

Arne

Bibliography

2001:

A. Leinse, C.G.H. Roeloffzen, K. Wörhoff, G. Sengo, R.M. de Ridder, A. Driessen, (2001, December 3), *Low loss fiber to chip connection system for telecommunication devices*, Poster/Proceedings of the 6th Annual Symposium IEEE/LEOS Benelux Chapter, Vrije Universiteit Brussel, Belgium, p. 185-188, ISBN: 90-5487247-0

2003:

Alfred Driessen, Arne Leinse, Sami Musa, Rene M. de Ridder, Sultur; *Polymer based integrated optics device in polymer optical fibers*, ed. By H.S. Nalwa, American Scientific Publishers, 2003, ISBN: 1-588883-012-8.

A. Leinse, A. Driessen, M.B.J. Diemeer, *Electro optical modulation in a polymer ring resonator*, (2003, October 18-25), 39th Course Microringresonators as building blocks for VLSI photonics, International School of Quantum Electronics, Erice, Sicily.

A. Leinse, A. Driessen, M.B.J. Diemeer, (2003, November 20-21), *Fabrication of an Electro Optic Polymer Ringresonator*, Poster/Proceedings of the 8th Annual Symposium IEEE/LEOS Benelux Chapter, University of Twente, Enschede, The Netherlands, p. 201-204, ISBN: 90-365-1990-X.

J. Flokstra, J. Sesé, A.A. Joseph, A. Leinse, I. Oomen, S. Radovanovic, K. Shunmugavel, E.H. Sujiono, G.F.M. Wiegerinck, *Terahertz Signal Processing*, (2003, October 2) MESA⁺ Annual meeting, University of Twente, The Netherlands.

2004:

A. Leinse, M.B.J. Diemeer, A. Driessen, *Scattering loss reduction in polymer waveguides by reflowing*, IEE Electronics letters, vol. 40 nr.16, August 2004, p.992-993

BIBLIOGRAPHY

A. Leinse, M.B.J. Diemeer and A. Driessen, *Scattering loss reduction in polymer waveguides by reflowing*, Annual workshop on Photonics Materials and Technology organized by the LEOS Benelux chapter, Eindhoven May 2004 (Oral presentation).

A. Leinse, M.B.J. Diemeer and A. Driessen, (2004, December 2-3), *High speed electro optic polymer micro-ring resonator*, Poster/Proceedings of the 9th Annual Symposium IEEE/LEOS Benelux Chapter, Ghent University, Ghent, Belgium, p. 111-114, ISBN: 9076546061.

P. Nagtegaele, H.Kelderman, A. Leinse, M.Diemeer, J. Zyss and A.Driessen, *Organic microresonators based devices and sub-systems for optical telecommunications*, SPIE conference Photonic West 2005 San Jose USA (Oral presentation in Conference 5728)

P. Nagtegaele, H.Kelderman, A. Leinse, M.Diemeer, J. Zyss and A.Driessen, *Vers une nouvelle filière de composants et sous-systèmes à base de matériaux hybrides et de polymères pour les télécommunications*, 2004, October 25-27, JNOG 2004 : 23rd National Conference on Guided Optics

P. Nagtegaele, H.Kelderman, A. Leinse, M.Diemeer, J. Zyss and A.Driessen, *Composants et sous-systèmes à base de organiques pour les télécommunications optiques microrésonateurs*, 2004, September 15-17, DIELOR 04 : Organic Electronic Devices, Limoges, France

2005:

A. Leinse, M.B.J. Diemeer, A. Rousseau, A. Driessen, *High speed polymer e-o modulator consisting of a MZI with a micro ring resonator*, Proceedings of ECIO'05: 12th European conference on integrated optics, 6-8 April 2005, Grenoble, France, oral presentation, p 184-187

A. Leinse, M.B.J. Diemeer, A. Rousseau and A. Driessen, *A novel high speed polymeric EO modulator based on a combination of a micro ring resonator and an MZI*, IEEE Photonics Technology Letters, submitted February 25th 2005 (accepted after little revisions)